

## Optically induced magnetization reversal in Co/Pt multilayers: Role of domain wall dynamics

Umut Parlak

Schlüsseltechnologien / Key Technologies

Band / Volume 232

ISBN 978-3-95806-536-9





Forschungszentrum Jülich GmbH  
Peter Grünberg Institut (PGI)  
Elektronische Eigenschaften (PGI-6)

**Optically induced magnetization  
reversal in Co/Pt multilayers:  
Role of domain wall dynamics**

Umut Parlak

Schriften des Forschungszentrums Jülich  
Reihe Schlüsseltechnologien / Key Technologies

Band / Volume 232

---

ISSN 1866-1807

ISBN 978-3-95806-536-9

Bibliografische Information der Deutschen Nationalbibliothek.  
Die Deutsche Nationalbibliothek verzeichnet diese Publikation in der  
Deutschen Nationalbibliografie; detaillierte Bibliografische Daten  
sind im Internet über <http://dnb.d-nb.de> abrufbar.

Herausgeber und Vertrieb: Forschungszentrum Jülich GmbH  
Zentralbibliothek, Verlag  
52425 Jülich  
Tel.: +49 2461 61-5368  
Fax: +49 2461 61-6103  
[zb-publikation@fz-juelich.de](mailto:zb-publikation@fz-juelich.de)  
[www.fz-juelich.de/zb](http://www.fz-juelich.de/zb)

Umschlaggestaltung: Grafische Medien, Forschungszentrum Jülich GmbH

Druck: Grafische Medien, Forschungszentrum Jülich GmbH

Copyright: Forschungszentrum Jülich 2021

Schriften des Forschungszentrums Jülich  
Reihe Schlüsseltechnologien / Key Technologies, Band / Volume 232

D 464 (Diss. Duisburg, Univ., 2021)

ISSN 1866-1807  
ISBN 978-3-95806-536-9

Vollständig frei verfügbar über das Publikationsportal des Forschungszentrums Jülich (JuSER)  
unter [www.fz-juelich.de/zb/openaccess](http://www.fz-juelich.de/zb/openaccess).



This is an Open Access publication distributed under the terms of the [Creative Commons Attribution License 4.0](https://creativecommons.org/licenses/by/4.0/), which permits unrestricted use, distribution, and reproduction in any medium, provided the original work is properly cited.

# Zusammenfassung

Das rein optische Schalten (*All-optical switching, AOS*) der Magnetisierung hat aufgrund der vielversprechenden Anwendungsaussichten in der magnetischen Speichertechnologie immer mehr an Interesse und Aufmerksamkeit gewonnen. Seit der ersten Demonstration im Jahr 2007, konnte AOS in verschiedenen Materialien beobachtet werden. Unter diesen befindet sich das ferromagnetische Co/Pt Mehrschichtsystem, welches aufgrund einzigartiger magnetischer und magneto-optischer Eigenschaften, als Vorreiter dient.

In dieser Arbeit, wurden optisch induzierte Magnetisierungsumkehrmechanismen in  $[\text{Co/Pt}]_N$  Mehrschichtsystemen, in Abhängigkeit der Anzahl der Doppelschichten  $N$  und der Strahleigenschaften des Lasers, untersucht. Die Mehrfachschichten wurden unter Verwendung der Magnetronsputtertechnik, bei genau kontrollierten Bedingungen gewachsen, sodass die Genauigkeit der Schichtdicke im Subnanometerbereich erhalten bleibt und die Rauheit der Grenzfläche reduziert wird. Bildgebung von optisch induzierten magnetischen Domänen wurde unter Verwendung eines optischen Mikroskops, basierend auf dem magneto-optischen Kerr Effekt (MOKE), durchgeführt. Wir verwendeten ebenfalls ein Photoelektronenmikroskop, durch welches eine Bildgebung mit verbesserter lateraler Auflösung und Elementselektivität gegeben ist.

Unsere detaillierte Untersuchung optisch induzierter Domänen zeigt, dass AOS in  $[\text{Co/Pt}]_N$  nur in einem genau definierten Laserfluenzintervall möglich ist, welches mit der Curie-Temperatur der Probe zusammenhängt. Darüber hinaus haben wir bestätigt, dass helizitätabhängiges AOS eine Mehrzahl an Laserpulsen, sowie eine Feinabstimmung der Laserstrahlparameter erfordert. Um den Effekt der laserinduzierten Erwärmung auf das Phänomen des AOSs weiter zu untersuchen, haben wir die Probenunterschiedlichen Laser-Wiederholungsraten bei unterschiedlichen Temperaturen ausgesetzt. Diese Experimente erlaubten uns die Entwicklung eines Modells für die Dynamik der Domänenwände basierend auf dem Wärmegradienten, welcher durch das Gaußschen Intensitätsprofil des Laserstrahls gegeben ist. Die Mechanismen für AOS sollen im Rahmen dieses Modells besprochen werden.

Um einen detaillierten Einblick in AOS zu erhalten, haben wir ultraschnelle Entmagnetisierungsdynamiken  $[\text{Co/Pt}]_3$  Mehrschichtsystemen mit einem zeitaufgelösten

MOKE-Aufbau untersucht. Wir haben charakteristische Entmagnetisierungs- und Relaxionszeiten in Abhängigkeit von der Laserfluenz gemessen. Die Experimente zeigten, dass sich die Magnetisierung innerhalb von 300 fs aufhebt und die Relaxation in zwei verschiedenen Zeitskalen auftritt. Dies weist darauf hin, dass mehrere Prozesse zur Relaxation beitragen.

Unsere detaillierte Untersuchung von ferromagnetischen  $[\text{Co}/\text{Pt}]_N$  Mehrschichtsystemen und deren magnetische Antwort auf Femtosekundenlaserpulse trägt zu einem besseren Verständnis des physikalischen Bilds von AOS bei.

# Abstract

All-optical switching (AOS) of magnetization has been attracting an increasing attention due to the promising application prospects in magnetic data recording technology. Since the first demonstration in 2007, AOS has been observed in a limited range of materials. Among them, the ferromagnetic Co/Pt multilayer system comes to the forefront owing to its unique magnetic and magneto-optical properties.

In the present project, we investigated optically induced magnetization reversal mechanisms in  $[\text{Co/Pt}]_N$  multilayers depending on the number of bilayers  $N$  and the laser beam properties. The multilayers were grown using magnetron sputtering technique at precisely controlled conditions to maintain sub-nanometer thickness precision and reduced interface roughness. Imaging of optically induced magnetic domains was performed, using optical microscopy based on magneto-optical Kerr effect (MOKE), during laser illumination. We also employed photoemission electron microscope for imaging with enhanced lateral resolution and element selectivity.

Our detailed investigation of optically induced domains revealed that AOS in  $[\text{Co/Pt}]_N$  is only possible in a well defined laser fluence interval associated with the Curie temperature of the sample. Moreover, we confirmed that helicity-dependent AOS requires multiple laser pulses as well as a fine tuning of the laser beam parameters. In order to further investigate the effect of laser-induced heating on AOS, we illuminated the samples using different laser repetition rates at different temperatures. These experiments allowed us to develop a model based on domain wall dynamics induced by thermal gradient due to the Gaussian intensity profile of the laser beam. We discuss the AOS mechanisms within the framework of this model.

In order to gain a detailed insight in AOS, we studied ultrafast demagnetization dynamics of  $[\text{Co/Pt}]_3$  multilayers using a time-resolved MOKE system. We measured characteristic demagnetization and recovery times as a function of the laser fluence. Experiments showed that the magnetization quenches within  $\sim 300$  fs and relaxation occurs in two different timescales pointing towards multiple processes governing the relaxation.

Our extensive study of ferromagnetic  $[\text{Co/Pt}]_N$  multilayers and their magnetic response to the femtosecond laser pulses contribute to a clearer physical picture of laser-induced AOS in ferromagnetic multilayers.



*Our true mentor in life is science.*

- Kemal Atatürk

# Contents

<b>Zusammenfassung</b>	<b>iii</b>
<b>Abstract</b>	<b>v</b>
<b>1 Introduction</b>	<b>1</b>
1.1 Magnetic recording . . . . .	1
1.2 Scope of this thesis . . . . .	4
<b>2 Fundamental aspects</b>	<b>7</b>
2.1 Ferromagnetism of 3d transition metals . . . . .	7
2.1.1 Spin-orbit interaction . . . . .	11
2.2 Magnetic metallic multilayers . . . . .	12
2.2.1 Interface-induced magnetic phenomena . . . . .	14
2.3 Magnetic anisotropy in thin films . . . . .	15
2.3.1 Shape anisotropy . . . . .	16
2.3.2 Magnetocrystalline anisotropy . . . . .	17
2.3.3 Surface and interface induced anisotropy . . . . .	17
2.4 Coupling mechanisms in magnetic multilayers . . . . .	19
2.5 Magnetic domains . . . . .	20
2.5.1 Domain formation . . . . .	20
2.5.2 Domain walls . . . . .	21
2.5.2.1 Domain wall width . . . . .	22
2.5.2.2 Coercivity of domain walls . . . . .	23
2.5.3 Magnetic hysteresis . . . . .	23
2.6 Precessional magnetization dynamics . . . . .	24
2.6.1 Landau-Lifschitz-Gilbert equation . . . . .	25
2.7 Magneto-optical effects . . . . .	26
2.7.1 Polarized light . . . . .	27
2.7.1.1 Jones formalism . . . . .	27
2.7.2 Magneto-optical Kerr effect . . . . .	28
2.7.2.1 Microscopic description of MOKE . . . . .	31
2.7.2.2 Inverse Faraday effect . . . . .	31
2.7.3 Magneto-optical effects in the x-ray region . . . . .	33
2.7.3.1 X-ray absorption and XMCD . . . . .	33
<b>3 Review of ultrafast magnetism phenomena and all-optical switching</b>	<b>35</b>
3.1 Optical excitation of magnetic metals . . . . .	35
3.2 Laser-induced ultrafast magnetization dynamics . . . . .	36
3.2.1 Phenomenological descriptions . . . . .	37
3.2.2 Microscopical descriptions . . . . .	39
3.2.3 Summary . . . . .	40
3.3 All-optical switching . . . . .	41
3.3.1 Early predictions of AOS . . . . .	41

3.3.2	All-optical switching in ferrimagnetic thin films . . . . .	41
3.3.3	All-optical switching in ferromagnetic multilayers . . . . .	45
3.3.4	Proposed mechanisms . . . . .	48
3.3.4.1	Summary . . . . .	52
<b>4</b>	<b>[Co/Pt]<sub>N</sub> multilayers: Sample fabrication and characterization</b>	<b>53</b>
4.1	Magnetic properties of [Co/Pt] <sub>N</sub> multilayers . . . . .	53
4.1.1	Magneto-optical properties . . . . .	53
4.1.2	Perpendicular magnetic anisotropy (PMA) . . . . .	54
4.1.3	Domains . . . . .	55
4.1.4	Magnetic properties depending on repetition . . . . .	56
4.2	Thin film fabrication and characterization instruments . . . . .	57
4.2.1	Magnetron sputtering . . . . .	57
4.2.2	Atomic/Magnetic force microscopy . . . . .	59
4.2.3	X-ray reflectivity . . . . .	60
4.2.4	Magneto-optical Kerr effect magnetometry . . . . .	61
4.3	Taguchi's method for roughness minimization . . . . .	63
4.3.1	Roughness minimization . . . . .	64
4.4	[Co/Pt] <sub>N</sub> multilayer fabrication . . . . .	67
4.5	Analysis and results . . . . .	68
4.5.1	Structural analysis . . . . .	68
4.5.2	Static magnetic characterization . . . . .	69
<b>5</b>	<b>Experimental techniques</b>	<b>75</b>
5.1	Description of the femtosecond laser system . . . . .	75
5.1.1	Laser amplifier . . . . .	76
5.2	Time-resolved MOKE setup . . . . .	79
5.2.1	Determination of pulse duration . . . . .	79
5.3	Magneto-optical Kerr microscopy . . . . .	82
5.4	X-ray photoemission electron microscopy . . . . .	87
5.4.1	FE-LEEM P90 at UE56/1-SGM beamline . . . . .	87
<b>6</b>	<b>Optical control of magnetization in Co/Pt multilayers</b>	<b>89</b>
6.1	Quasi-static all-optical switching of magnetization . . . . .	89
6.1.1	Methodology of all-optical switching experiments . . . . .	89
6.1.2	AOS dependence on laser fluence . . . . .	91
6.1.3	AOS dependence on number of pulses . . . . .	92
6.1.3.1	Sweeping beam . . . . .	93
6.1.3.2	Static beam . . . . .	97
6.1.4	AOS dependence on bilayer repetition . . . . .	99
6.2	Domain formation and relaxation mechanism . . . . .	102
6.2.1	Heat assisted magnetic recording . . . . .	103
6.3	Discussion . . . . .	104
6.3.1	Laser intensity threshold for AOS . . . . .	104
6.3.2	Domain wall dynamics model . . . . .	106
6.3.3	Role of laser pulse accumulation . . . . .	108
6.3.4	General overview of AOS by domain wall motion . . . . .	110
6.4	Conclusions . . . . .	111

---

<b>7</b>	<b>Domain wall drift driven by laser pulses</b>	<b>113</b>
7.1	Introduction . . . . .	113
7.2	Results and analysis . . . . .	113
7.3	Discussion and conclusion . . . . .	116
<b>8</b>	<b>Ultrafast demagnetization dynamics of [Co/Pt]<sub>3</sub> multilayer - An outlook</b>	<b>119</b>
8.1	Introduction . . . . .	119
8.2	Results . . . . .	120
8.2.1	Laser fluence dependence . . . . .	120
8.2.2	Magnetic field dependence . . . . .	122
8.3	Discussion . . . . .	123
8.4	Conclusions . . . . .	124
<b>9</b>	<b>Conclusion and outlook</b>	<b>125</b>
	<b>Appendix A Gaussian beams</b>	<b>129</b>
	<b>Appendix B Cryostat</b>	<b>131</b>
	<b>Appendix C Curie temperature of [Co/Pt]<sub>3</sub> multilayer</b>	<b>133</b>
	<b>Appendix D Determination of the <math>p</math>-values</b>	<b>135</b>
	<b>Bibliography</b>	<b>137</b>
	<b>Abbreviations</b>	<b>I</b>
	<b>Symbols</b>	<b>III</b>
	<b>Publications and conference contributions</b>	<b>V</b>
	<b>Curriculum vitae</b>	<b>IX</b>
	<b>Acknowledgments</b>	<b>XI</b>



# Chapter 1

## Introduction

### 1.1 Magnetic recording

The late 19th century has witnessed the invention and development of early magnetic storage devices in a form of magnetic tapes which were mainly used for audio recording [1, 2]. Introduced in 1956, hard disk drives (HDD), with a capacity of 3.75 MB [3], had been on the other hand employed in computers for data storage purposes. High demand in worldwide data storage for personal computers, smart phones and cloud computing encouraged scientists and engineers to find new approaches to increase the capacity and processing speed. Today, it is forecasted that the data storage capacity on the market will achieve 40 TB or higher by 2023 [4].

A modern hard disk drive utilizes the magnetization direction of a ferromagnetic domain to store the logical information. Each magnetic domain represents a ‘bit’ stored as *zero* or *one* depending on its magnetic orientation. The magnetization direction is conventionally manipulated by an external magnetic field generated by an inductive write head sliding over the recording medium [5]. In order to read-out a recorded magnetic bit, modern magneto-resistive read heads are used instead of an inductive measurement of the stray field. Magneto-resistive spin-valve heads have revolutionized the recording market after the invention of giant magneto-resistance (GMR) effect by Albert Fert and Peter Grünberg [6, 7].

Ever since the earlier devices, magnetization of a recording media had been aligning parallel to the surface for sake of write- and read-ability of the head. After the down-sizing of the read-heads and development of out-of-plane magnetized media, based on CoCrPt, FePt:C [8, 9], the outdated in-plane longitudinal magnetic recording (LMR) technology was substituted by perpendicular magnetic recording (PMR) [10]. With the advances in PMR technology, data storage density has tremendously increased due to the fact that out-of-plane media has a lower demagnetizing fields and allows much denser packing of magnetic bits [8, 11].

Today, the highest areal data density is reached by the shingled magnetic recording (SMR) technology introduced in 2013. SMR allows writing of the data in overlapping magnetic tracks and increases the track density per hard drive [12,13]. Reduced writing performance as well as data management are the main challenges of the SMR technology. Other emerging recording technologies are based on heat-assisted magnetic recording (HAMR) [4,14,15], microwave-assisted magnetic recording (MAMR) [16,17], two-dimensional magnetic recording (TDMR) [18,19] and bit-patterned magnetic recording (BPMP) [20–22]. On the other hand, non-magnetic flash memories, i.e. solid-state drives (SSD), are also expected to establish a larger presence in the market very soon because of their faster access time [23]. However, HDDs have still higher capacity, longer life-time and lower cost per MB.

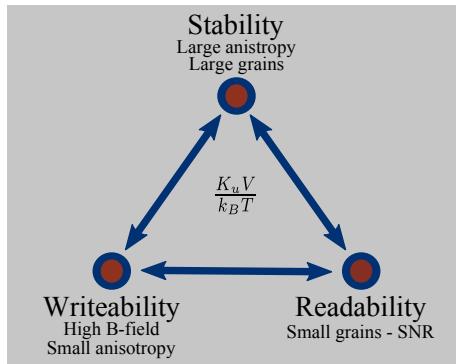


Figure 1.1: Schematics of the magnetic recording trilemma. Writeability, readability and stability compete in terms of anisotropy, grain volume and external magnetic field.

The limitation of today’s HDD technology is the competition between writeability, readability and stability. This problem is known as Magnetic Recording Trilemma [24,25], illustrated in Figure 1.1. A bit is assigned to a magnetic domain, which is formed by a number of grains of the polycrystalline or granular medium. The smallest magnetic unit, therefore, can be of the size of one single grain. The magnetic energy stored in a single grain is  $K_u V$ , where  $K_u$  is the magnetic anisotropy constant and  $V$  is the volume of the grain. In order to maintain a stable magnetic bit, this energy has to overcome the thermal energy  $k_B T$ . From the Arrhenius-Néel theory, one can estimate that the  $K_u V / k_B T$  ratio has to be larger than 40 in order to keep the magnetization stable for  $\sim 10$  years at room temperature [25]. On one hand, increasing the volume  $V$  of grains will reduce the readability by decreasing the signal-to-noise ratio [26]. On the other hand, an increased anisotropy energy  $K_u$  will require higher magnetic fields for reversal. On the contrary, shrinking the grain size will eventually reach the

superparamagnetic limit [27].

Heat-assisted magnetic recording has been proposed as a possible solution to overcome the limitations arising from the Magnetic Recording Trilemma. This recording technology enables the use of granular thin film materials with very high magnetocrystalline anisotropy. The grains with high-anisotropy are thermally stable, but cannot be written by the conventional write-heads. By locally heating the recording medium during the writing process, the coercive field ( $H_C$ ) can be temporarily lowered below the available applied magnetic field. In order to apply a local heating, high local temperatures are generated by an optical system. Generally, a laser source is employed combined with a near field transducer (NFT) [28, 29]. The heated area then rapidly cools under applied field and thus stores the magnetic bit for a longer period [14, 29, 30]. The writing and storing process is schematically shown in Figure 1.2. Despite the lack of HDDs utilizing HAMR technology on the market at present, first demonstrations have already been done and the high-capacity devices are expected to be shipped in the very near future [31].

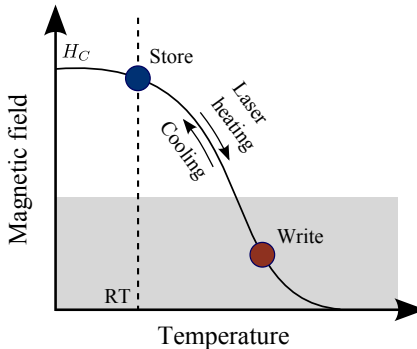


Figure 1.2: Schematic diagram of the HAMR writing and storage process. Figure adapted from [14].

A further progress in magnetic data storage requires not only a larger capacity, but also a faster data processing speed. The speed of writing a magnetic bit is governed by the time required to reverse its magnetization. In a typical ferromagnet, the magnetization can be reversed by  $180^\circ$  by applying magnetic fields opposite to the initial magnetization orientation in the presence of thermal excitations. Under an external field  $H_{ext}$ , the torque exerted on magnetization induces a damped precessional motion. The precession period and strength of the damping determine the reversal time, which is usually in the nanosecond timescale.

Ultrashort laser pulses provide a new approach to excite magnetic materials on the timescale of fundamental magnetic interactions. In 1996, Beaurepaire *et al.* showed that the illumination of Ni thin layers with 60 fs laser pulses leads to an ultrafast



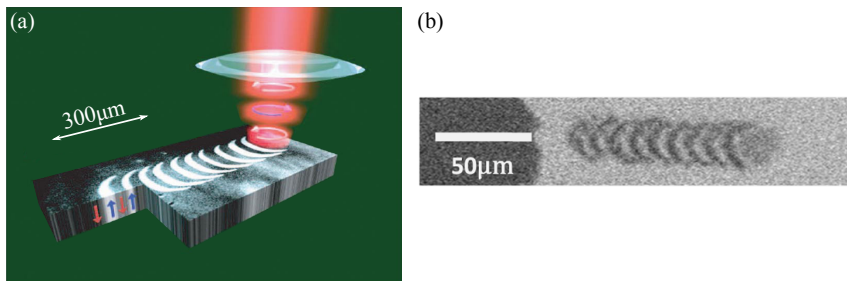


Figure 1.3: Demonstration of all-optical recording of magnetic bits using alternating circularly polarized laser pulses. (a) GdFeCo ferrimagnetic alloy. Image taken from Ref. [33]. (b) Co/Pt multilayer. The pattern was written by moving the beam for  $5 \mu\text{m}$  with a dwell time of 5 seconds. (Performed in the framework of this thesis.)

demagnetization [32]. Stanciu *et al.* demonstrated that the fs laser pulses can also be applied to deterministically switch the magnetization state of ferrimagnetic GdFeCo films depending on the laser helicity [33]. This all-optical helicity-dependent switching was later observed also in ferromagnetic Co/Pt multilayers [34].

The all-optical magnetization switching method promises a contribution to the high-density storage and faster data writing technology. On the other hand, the physical mechanism of the process still lacks a detailed theoretical understanding and many questions still remain unanswered.

## 1.2 Scope of this thesis

The motivation of this study is first to demonstrate all-optical magnetization switching in  $[\text{Co/Pt}]_N$  multilayers. When this study started, the publication of Lambert *et al.* [34] was the only report on all-optical switching of ferromagnetic multilayers. The second task is then to determine the laser beam parameters, i.e., fluence, polarization, pulse repetition rate, number of pulses required for magnetization switching. Overall, we investigated the physical principles involved the interaction of laser pulses with  $[\text{Co/Pt}]_N$  multilayers, as well as processes governing optically controlled magnetization switching.

It was earlier shown that the sample thickness plays a decisive role. In this work, the sample thickness was tuned by varying the multilayer repetition rate. Additionally, the effect of the sample temperature was investigated.

In this work, we show, in agreement with the literature, that the single-pulse helicity-dependent all-optical switching in these ferromagnetic multilayers is not possible for

the standard set of laser parameters. Single pulses only give rise to ultrafast demagnetization and consequently break the magnetization into domains. We investigate the magnetization dynamics on sub-picosecond timescales.

This thesis is organized in the following way:

**Chapter 2** gives a general overview of magnetism in 3d metallic materials in thin film and multilayer form. Anisotropy, coupling and domain concepts are discussed, in particular, for perpendicularly magnetized layers. A brief description of magneto-optical effects in both the visible and x-ray region is also given at the end of the chapter.

**Chapter 3** provides an overview of the ultrafast magnetism concepts with a particular focus on the current knowledge about all-optical magnetization switching in ferri- and ferromagnetic materials.

**Chapter 4** introduces the  $[\text{Co/Pt}]_N$  sample system and its unique magnetic properties. The processes and instruments employed for fabrication and characterization steps of  $[\text{Co/Pt}]_N$  multilayers are discussed in detail.

**Chapter 5** covers the principal instruments and setups employed in this work for imaging the optically induced magnetic domains and measuring the ultrafast demagnetization dynamics.

**Chapter 6** is dedicated to the quasi-static all-optical magnetization switching experiments. The chapter involves the procedure of switching experiments, image analysis, simulations and a detailed discussion based on our findings.

**Chapter 7** presents an experimental study and analysis of domain wall drift driven by laser pulses.

**Chapter 8** is focused on the ultrafast demagnetization dynamics of  $[\text{Co/Pt}]_3$  multilayer system. Characteristic timescales of demagnetization and relaxation processes were measured using a time-resolved MOKE setup.

**Chapter 9** summarizes the conclusions of the presented work and finally provides the outlook for the future studies.



# Chapter 2

## Fundamental aspects

This chapter covers the fundamental descriptions of physical mechanisms governing magnetism in 3d metallic layers and forms the basis for understanding magnetic anisotropies, magnetic domains as well as magnetization dynamics. These concepts are discussed from the aspect of perpendicularly magnetized magnetic films due to their importance as being the main sample system in this work. In addition, a brief overview of the magnetic phenomena emerging from the atomic configurations at the surfaces and interfaces of the multilayer systems are given.

Magneto-optical effects are important not only for their ability to probe magnetic properties of solid thin films. They can be also employed to control the magnetic state of the material. In that sense, phenomenological and microscopic mechanisms are discussed in [Section 2.7](#).

### 2.1 Ferromagnetism of 3d transition metals

Ferromagnetism refers to a magnetic state where all magnetic moments in the solids are aligned parallel in a long-range. That yields a spontaneous magnetization below a certain temperature called Curie temperature  $T_C$ , even in the absence of an external magnetic field. Fe, Co and Ni are the only elements showing ferromagnetism at room temperature. Some rare-earth elements like Gd, Tb and Ho are other ferromagnetic elements with much lower Curie temperatures. Elemental ferromagnets are fundamentally divided into two classes depending on the electronic configuration contributing to magnetism. In the rare-earths, magnetic moments are carried by the localized f-electrons. On the other hand, magnetism in 3d transition metals has its origin in magnetic moments of the delocalized electrons in partially filled d-states.

Collective behavior of parallel aligned magnetic moments ( $\mathbf{m}_i$ ) in a volume  $V$  is rep-

resented by the magnetization vector,  $\mathbf{M}$ .

$$\mathbf{M} = \frac{\sum \mathbf{m}_i}{V} \quad (2.1)$$

The total magnetic moment of an atom is composed of orbital (l) and spin (s) angular momenta, and expressed in terms of Bohr magneton  $\mu_B$  [35]:

$$\mathbf{m} = (2s + l)\mu_B/\hbar \quad (2.2)$$

The direct exchange mechanism plays a decisive role in the alignment of the magnetic moments. The exchange interaction reflects the Coulomb interactions of two nearby electrons obeying the Pauli exclusion principle. This interaction arises from the quantum nature of the indistinguishable electrons and has no classical analogue. Detailed descriptions and derivation of the direct exchange mechanism can be found in various textbooks [35, 36]. Here, we take the Heisenberg formalism into consideration with the Hamiltonian:

$$H = - \sum_{i,j}^N J_{ij} \mathbf{S}_i \cdot \mathbf{S}_j = -2 \sum_{i<j}^N J_{ij} \mathbf{S}_i \cdot \mathbf{S}_j \quad (2.3)$$

where the sign of the exchange integral  $J$ , being the exchange coupling constant between spin  $S_i$  and spin  $S_j$ , stands for either parallel (ferromagnetic,  $J > 0$ ) or antiparallel (antiferromagnetic,  $J < 0$ ) spin alignment. In the above discussion we did not include electron-electron interactions in the crystal environment where an electric field is created due to the neighboring atoms. Breaking the spherical symmetry by this *crystal field* may cause a quenching of the orbital momentum, so that total angular momentum  $\mathbf{J}$  equals to spin momentum  $\mathbf{S}$ , instead of  $\mathbf{L} + \mathbf{S}$  [37, 38].

On the continuum level, the exchange integral is replaced by the exchange stiffness parameter  $A$ , and single spins are replaced by a continuous magnetization  $\mathbf{M}$ . The Bethe-Slater curve (in Figure 2.1) represents the variation of the exchange integral as

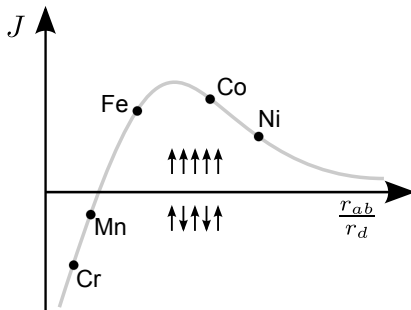


Figure 2.1: Sign variation of the exchange integral  $J$  of the 3d metals is described by Bethe-Slater curve as a function of interatomic distance  $r_{ab}$  and radius of incompletely filled shells  $r_d$ .

a function of interatomic spacing and the radius of empty d-shells.

The Heisenberg model suits well for the materials with strongly localized electrons, such as 3d metal oxides, 4f metals and their compounds, but it is not suitable for itinerant magnets such as elemental 3d transition metals [39]. The magnetic moment per atom of Fe, Co and Ni is mostly carried by spin angular momentum of the electrons and amounts to  $2.2 \mu_B$ ,  $1.7 \mu_B$  and  $0.6 \mu_B$ , respectively [35]. The experimental data on the magnetic moment per atom deviate from the predictions for the 3d metals, because of the strongly delocalized 3d-electrons. Therefore, magnetic contribution of the itinerant electrons must be described using the band model of magnetism. The simplest band-like model of the ferromagnetic metals is known as Stoner-model [40]. According to the Stoner model, the interaction between the itinerant electrons are mediated by a molecular field, arising from exchange interactions [41]. A quantitative condition for the occurrence of spontaneous ferromagnetic ordering is the *Stoner criterion* that will be derived using the arguments of Mohn [41], Jiles [42] and Getzloff [43] using following arguments.

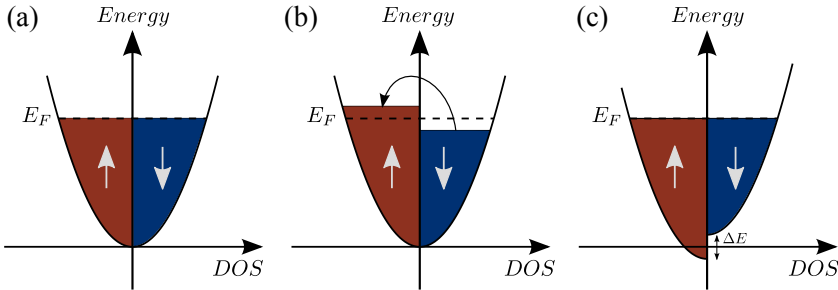


Figure 2.2: Stoner model of ferromagnetic transition metals used for the band description of magnetism. (a) Non-magnetic density of states split into the two sub-bands for the two spin directions. (b) Redistribution of spin-down electrons into unoccupied spin-up states. (c) Mutual shift of two sub-bands in order to equalize the Fermi energy level.

To derive the Stoner criterion, let us do a *Gedankenexperiment* on the band structure. In the non-magnetic case (Figure 2.2(a)), a number of spin-down and spin-up electrons occupy all possible states inside the Fermi sphere up to the Fermi level,  $E_F$ . In ferromagnetic materials 3d bands are partially filled. Between these partially filled sub-bands, the degeneracy can be removed by the exchange coupling which results in a redistribution of electrons at the Fermi surface, from spin-down sub-band to the empty states of the spin-up sub-band (Figure 2.2(b)). Finally, these two sub-bands mutually shift in energy-domain in order to equalize the Fermi levels (Figure 2.2(c)). A large exchange splitting may lead to a complete energy separation between the sub-

bands. In this case, one sub-band can shift completely below Fermi level and remain completely filled. Co and Ni are the best examples of this state. Therefore, they are called strong-ferromagnets, whereas Fe is a weak-ferromagnet.

The shift of the sub-bands indicates that spin-down electrons with energies between  $E_F - \delta E$  and  $E_F$  perform a spin-flip and are redistributed into unoccupied spin-up states with energies between  $E_F + \delta E$  and  $E_F$ . Therefore, the energy gain per electron amounts to  $\delta E$  and the number of redistributed electrons equals to  $1/2D(E_F)\delta E$ . Total increase in kinetic energy is given by:

$$\Delta E_{kin} = \frac{1}{2}D(E_F)(\delta E)^2 \quad (2.4)$$

Increase in the kinetic energy contradicts the energy minimization principle, however, it can be compensated by the exchange interactions. After the spin-flip, number of spin-up and spin-down electrons are calculated as follows.

$$n_{\uparrow} = \frac{1}{2}n + \frac{1}{2}D(E_F)(\delta E) \quad (2.5)$$

$$n_{\downarrow} = \frac{1}{2}n - \frac{1}{2}D(E_F)(\delta E) \quad (2.6)$$

with  $n$  being the number of electrons at the Fermi energy in the non-magnetic case. Magnetization can be expressed in terms of Bohr magneton and electron populations considering that each electron carries a magnetic moment of  $1 \mu_B$ .

$$M = \mu_B(n_{\uparrow} - n_{\downarrow}) \quad (2.7)$$

The molecular field is proportional to magnetization, and can be represented by  $\mathbf{B}_m = \lambda \mathbf{M}$ , where  $\lambda$  is the molecular field constant. Then the molecular field energy or potential energy,  $\Delta E_{pot}$  can be calculated as;

$$\Delta E_{pot} = \Delta E_m = - \int_0^M \mu_0 \lambda M' dM' = -\frac{1}{2}\mu_0 \lambda M^2 = -\frac{1}{2}\mu_0 \mu_B^2 \lambda (n_{\uparrow} - n_{\downarrow})^2 \quad (2.8)$$

Introducing Stoner parameter  $I = \mu_0 \mu_B^2 \lambda$ , the total energy change is written as following.

$$\Delta E = \Delta E_{kin} + \Delta E_{pot} \quad (2.9)$$

$$= \frac{1}{2}D(E_F)(\delta E)^2 - \frac{1}{2}I(D(E_F)\delta E)^2 \quad (2.10)$$

$$= \frac{1}{2}D(E_F)(\delta E)^2(1 - I \cdot D(E_F)) \quad (2.11)$$

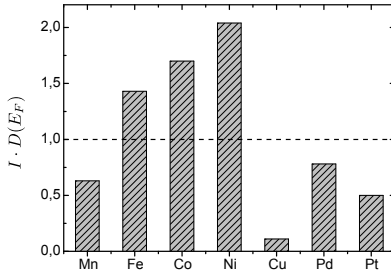


Figure 2.3:  $I \cdot D(E_F)$  product for selected materials. Fe, Co and Ni fulfill Stoner criterion. Data taken from [44].

Ferromagnetic ordering due to spontaneous spin splitting was assumed to be favored by energy minimization principle, i.e.  $\Delta E < 0$ . In the other words, transition metals can exhibit spontaneous magnetization only if they fulfill the *Stoner criterion*:

$$I \cdot D(E_F) \geq 1 \quad (2.12)$$

The model is very successful in predicting the onset of ferromagnetism for Fe, Co and Ni, but it overestimates Curie temperature ( $T_C$ ) and predicts that saturation magnetization ( $M_S$ ) vanishes gradually, by means of spin-flip excitations across the Stoner gap [38, 45]. In itinerant ferromagnets,  $M_S$  is strongly reduced close to  $T_C$  by randomization of magnetic moments, while their magnitude is preserved.

The value of Stoner parameter  $I$  is usually fixed for a given material, whereas density of states typically increases for ultrathin films owing to the reduced coordination number [46, 47]. This is a factor enhancing the magnetization in thin films of 3d metals [48]. In addition, it means that Stoner criterion can be met in thin films of 4d and 5d elements which are normally nonmagnetic.

### 2.1.1 Spin-orbit interaction

The previous discussion focused on spin-spin interactions and neglected spin-orbit interactions (SOI). As its name suggests, SOI describes the coupling of the spin and orbital angular momenta to form a new total angular momentum,  $J$ . SOI is a relativistic effect that occurs due to large electron orbital velocities. In the rest system of the electron, the electric field of the positive atomic nucleus is transformed into a magnetic field that couples to the spin of electron [49]. It is about 10-100 times smaller than the strength of exchange interaction ( $\sim 1$  eV), however, it can not be neglected in magnetism, since its importance for understanding the basic mechanisms [35].

The spin-orbit Hamiltonian can be written in terms of the electron spin and the



angular momentum of the perceived magnetic field of the lattice [35].

$$H_{SO} \approx \frac{g_e e}{2m^2 c^2 r} \frac{\partial V(r)}{\partial r} \mathbf{S} \cdot \mathbf{L} = \lambda(r) \mathbf{S} \cdot \mathbf{L} \quad (2.13)$$

where  $m$  and  $e$  are the mass and charge of an electron, respectively,  $c$  is the speed of the light,  $V(r)$  is the Coulomb potential of the atomic nucleus, and  $g_e$  is the electron g-factor  $\approx 2.002$ . SOI scales with the nuclear charge,  $\lambda(r) \propto (1/r)dV/dr \propto -Z|e|/r^3 \propto -Z^4$ , considering the expectation value  $\langle 1/r^3 \propto Z^3 \rangle$ , where  $Z$  is the nuclear charge. The assumption that the nuclear charge scaling is the same for all elements can be misleading when comparing SOI for e.g. 3d and 4d elements. Although, due to the nodes in the radial wave functions, the spin orbit coupling strength among the same group elements is far smaller than  $Z^4$ , as shown in Figure 2.4.

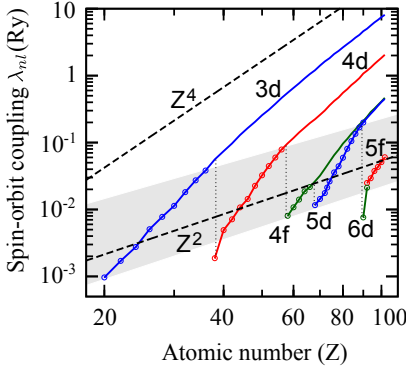


Figure 2.4: Spin-orbit coupling strength  $\lambda_{nl}$  of various series as a function of atomic number  $Z$  [50].  $Z^4$  dependency (upper dashed line) is calculated for the 3d series. The same scaling applies within each series, but SOI increases much slower ( $Z^2$ , lower dashed line) between different series.

Spin-orbit interaction determines the magnitude and direction of the magnetocrystalline anisotropy field. An important consequence of SOI is that it links the magnetization direction to the crystal lattice. Moreover, SOI is at the root of magneto-optical effects, magnetoresistance or anomalous and spin Hall effects.

As discussed later in the thesis, all-optical switching is observed only in a limited range of thin film systems including alloys and heterostructures. This fact points to the critical role of interfacial spin-orbit interactions in all-optical switching process [49].

## 2.2 Magnetic metallic multilayers

A multilayer consists of at least two materials stacked on top of each other in the form of thin films. These layers forming a multilayer can be in an amorphous, polycrystalline or single crystalline form. The term superlattice was coined to describe the alternating multilayers with a long range structural coherence, namely epitaxially grown structures.

Progresses in ultra-high vacuum (UHV) and thin-film fabrication technologies, such as molecular beam epitaxy (MBE), atomic layer deposition (ALD) and magnetron sputtering, allowed one to grow high-purity ultra-thin metallic multilayers with high uniformity and a well-defined thickness down to the level of atomic monolayers. These thicknesses correspond to the fundamental length-scales of magnetism, such as, the range of exchange interaction, domain wall thickness and mean free path (MFP) of electrons. The fact that these artificial thin multilayers do not exist in nature, opened the way to discover novel physical phenomena emerging from these unique properties of these multilayer systems.

The intrinsic magnetic properties of the materials, such as, Curie temperature, coercive field and anisotropy, can appreciably differ in thin films and bulk material. Generally, these properties are modified as long as the thin film thickness becomes comparable to the magnetic correlation length. For instance, a variation of Curie temperature  $T_C$  is empirically described by the following formula.

$$[T_C - T_C(N)]/T_C \sim N^{1/\nu} \quad (2.14)$$

where  $N$  is the thickness in monolayers and  $\nu$  is the critical exponent for the correlation length [48, 51].

A number of magnetic phenomena emerging from the finite size, broken symmetry and interface-induced effects of the multilayers have been known for a few decades. The discovery of fundamental magnetic effects, e.g., exchange bias [52, 53] and oscillatory interlayer coupling [7, 54], has led to the design of complex magnetic structures. Some of them, such as magneto-resistive multilayers [55], have been already employed in technological applications. Further research of the latter phenomena is promising even faster, smaller and more energy-efficient spintronic devices. General fundamental problems in spintronics, regarding the spin polarized currents and spin dependent scattering, have been resolved by making use of multilayers. For instance, the giant magnetoresistance (GMR) effect results from a combination of three interactions between layers [56]: (i) as the thickness of magnetic layers comparable with the electronic mean free path, electrons can transport to the adjacent magnetic layer crossing the non-magnetic spacer layer, (ii) the scattering cross-section of electrons at the interface depends on the orientation of the spin state and magnetization of the layer, (iii) the magnetization orientation of the layers can be modified by AFM coupling or magnetic pinning. Overall, the GMR effect arises from the relative resistivity of minority and majority spin states of electrons. A graphical description of the effect is shown in Figure 2.5.

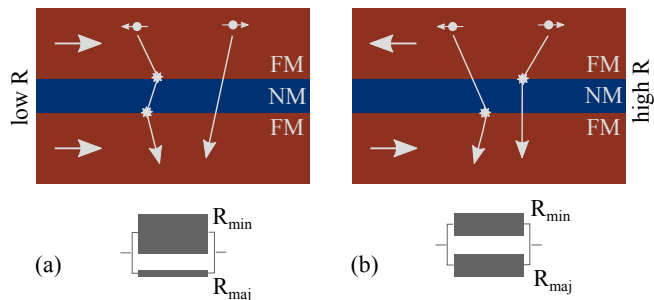


Figure 2.5: Simplified representation of giant magnetoresistance (GMR) effect in spin valve system. Electron transport takes place between two ferromagnetic (FM) layers with a nonmagnetic (NM) spacer in between. The electrons are strongly scattered when their spins are antiparallel to the local magnetization orientation. Spin-dependent scattering gives rise to a difference in equivalent resistances for (a) parallel and (b) antiparallel configuration.

### 2.2.1 Interface-induced magnetic phenomena

The discontinuity of the atomic structure and the broken translational and inversion symmetry at the interfaces constitute a fruitful playground for novel magnetic phenomena. The modified electronic band structure of the interfaces can create new magnetic states even in non-magnetic materials. A particular example of this phenomenon is the proximity-induced magnetic moments in Pt and Pd atoms which are already close to fulfill Stoner criterion [57, 58]. The breaking of inversion symmetry also creates a difference between ‘up’ and ‘down’ layers for the interface which may in turn induce the perpendicular anisotropy as described in the next section [59]. In the lack of inversion symmetry, strong spin-orbit coupling and exchange interaction may induce chiral arrangement of the magnetization at the interface [60, 61]. This interaction has the form of Dzyaloshinskii-Moria interaction (DMI), which has already led to a tremendous number of new phenomena in magnetism including skyrmions. Recently, magnetic skyrmions are even generated using single ultrafast laser pulses [62].

To conclude, many important effects in magnetism, such as Hall effects (spin-, quantum spin-, anomalous-), Rashba effect, spin transfer torque, spin-orbit torque are either intrinsically interfacial phenomena or enhanced at the interfaces. For a general overview, the reader is referred to Ref. [49].

### 2.3 Magnetic anisotropy in thin films

Ferromagnetic single crystals exhibit magnetic anisotropies that manifest themselves as easy and hard axes regarding the energy required to magnetize the material along a certain crystal direction. Magnetic anisotropy energy, by definition, is the amount of energy required to rotate the magnetization from one easy axis into one hard axis. Therefore, hard axes require more applied field to reach saturation state. A comparison between easy and hard axes of cobalt is shown in Figure 2.6.

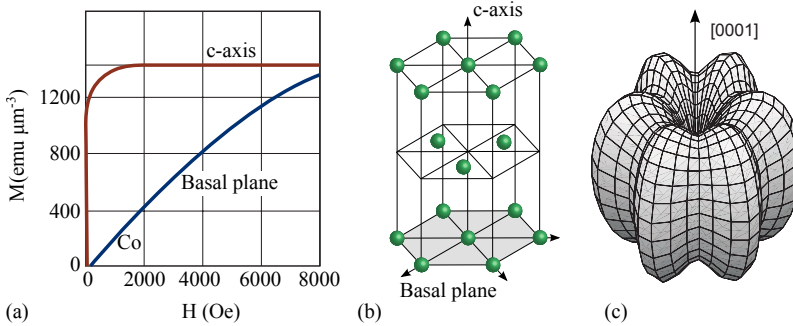


Figure 2.6: Magnetic anisotropy of crystalline cobalt. (a) The easy axis overlaps with hexagonal c-axis, whereas all basal planes are the hard axes. The data are reproduced from [63]. (b) Schematics of crystallographic orientations of hexagonal cobalt. (c) Polar plot of energy surface for a hexagonal crystal for easy axis along [0001] axis (c-axis) [64].

In the absence of magnetic anisotropy, thin film samples could not exhibit a long range ferromagnetic ordering, since the exchange interaction is short ranged [35]. Magnetic anisotropy in layered thin film structures can be engineered by alloying, varying thicknesses of the layers, and inducing magnetic anisotropies at the interfaces. It is even possible to change the magnetization from in-plane orientation to the out-of-plane orientation. The latter is termed as perpendicular magnetic anisotropy (PMA) and is particularly of interest for the magnetic data recording technologies.

There are two main interactions, which compete and eventually determine the magnetic anisotropy; namely magnetic dipolar interaction and spin-orbit interaction (SOI) [65]. Dipolar interaction has a long range character and mainly depends on the shape of the material. Basically, it favors in-plane magnetization due to the 2D geometry of the thin films (see Subsection 2.3.1). On the other hand, SOI has to do with crystal lattice, because the total magnetic moment is coupled to the lattice via SOI. Therefore, the magnetization direction reflects the symmetry of the crystal, which is the essence of magnetocrystalline anisotropy. In addition, the broken symmetry at the

surface or interface of a ferromagnetic layer leads to surface or interface anisotropies.

In a hexagonal crystal, such as cobalt, magnetocrystalline anisotropy has only one easy axis, which coincides with the hexagonal c-axis [66] (see Figure 2.6(b)). The associated magnetic anisotropy energy,  $E_{ani}$ , must be constant when the magnetization is inverted.  $E_{ani}$  is thus expressed as a series of even functions as

$$E_{ani} = K_1 \sin^2 \theta + K_2 \sin^4 \theta + \dots = \sum K_n \sin^{2n} \theta \quad (2.15)$$

where  $\theta$  denotes the angle between the surface normal and magnetization, and  $K_i$  are the anisotropy constants, which depend on the material and vary with the temperature. In thin films,  $K_1$  and  $K_2$  are usually much larger than the other terms and the anisotropy constant can be simplified in a  $K_{eff}$  term, which includes volume and surface contributions. The volume term  $K_V$  is independent of magnetic layer thickness  $t$ , whereas the surface/interface term  $K_S$  is proportional to  $1/t$ . The volume term is composed of magnetocrystalline  $K_{MCA}$  and shape  $K_{Sh}$  anisotropies.

### 2.3.1 Shape anisotropy

The origin of the shape anisotropy is the demagnetizing magnetic field,  $H_{demag}$ , generated by the magnetization of the magnetic material itself. In a homogeneously magnetized material, all magnetic moments experience the dipolar field from the neighboring moments. These dipole fields cancel each other, except the ones placed at the boundaries of the sample [67]. Due to the finite size of the samples, these dipoles create a stray field outside of the sample which results in a demagnetizing field acting against the magnetization vector. Hence, the origin of shape anisotropy is basically a dipole-dipole interaction. The strength of this demagnetizing field can be written as:

$$\mathbf{H}_{demag} = -\mathcal{N} \cdot \mathbf{M} \quad (2.16)$$

where  $\mathcal{N}$  is the demagnetizing tensor. The calculation of  $\mathcal{N}$  is strongly shape-dependent. Generally it is given as

$$\mathcal{N} = \begin{pmatrix} N_1 & 0 & 0 \\ 0 & N_2 & 0 \\ 0 & 0 & N_3 \end{pmatrix} \quad (2.17)$$

with  $N_1 + N_2 + N_3 = 1$ , in MKS units. For an infinitely large and very thin layer,  $N_1 = N_2 = 0$  and  $N_3 = 1$ . Therefore, the demagnetizing energy is:

$$E_{demag}/V = \frac{1}{2} \mu_0 M^2 \cos^2 \theta \quad (2.18)$$

with the shape anisotropy constant  $K_{Sh} = \mu_0 M^2 / 2$  [68].

### 2.3.2 Magnetocrystalline anisotropy

As stated above, magnetocrystalline anisotropy (MCA) has its microscopic origin in spin-orbit interaction. In crystalline metals, the wavefunctions of strongly localized d-electrons overlap in an anisotropic manner in accordance with the crystallographic orientation. This means that spin-orbit interaction depends on the crystallographic orientation and plays a decisive role in the anisotropy. The exchange interaction itself, on the other hand, does not contribute to the anisotropy, because the scalar product of the spin vectors is independent of the angle between spins and the crystal axes.

Polycrystalline ferromagnets exhibit no -or only small- net magnetocrystalline anisotropy as the contributions of randomly oriented grains cancel out [43].

### 2.3.3 Surface and interface induced anisotropy

Néel first predicted that the broken translational symmetry at the interfaces (FM-FM, FM-NM or FM-Air) may give rise to a new uniaxial anisotropy owing to the missing bonds and incompletely quenched orbital moments. The energy associated with an interfacial anisotropy is expressed as:

$$E_{int} = \frac{K_i}{t} \sin^2 \theta \quad (2.19)$$

where  $t$  is layer thickness and  $\theta$  is the angle between the surface normal and the magnetization. Thus, the contribution of interface anisotropy depends on the thickness of the film. When the interface anisotropy energy dominates in a thin layer, this energy favors a magnetic anisotropy perpendicular to the surface plane which is counteracting the dipolar induced shape anisotropy. Perpendicular magnetic anisotropy is particularly observed in multilayers and alloyed films. Multilayers are mostly in the form of FM/X, where FM:Fe, Co, Ni and X is typically a metal with strong spin-orbit coupling. Notable examples of Co/X multilayers are; Co/Pt [69], Co/Pd [59], Co/Au [70], Co/Ir [71] and Co/Ni [72, 73]. The latter interestingly consists of two ferromagnetic components. Ni/Pt [74], Fe/MgO [75] are the examples of other ferromagnetic bilayers with PMA. In addition, many of RE-TM multilayers [76, 77] and alloys [78–82] exhibit perpendicular anisotropy. The degree of interface anisotropy can be tailored by tuning the composition of alloys or the contribution of interfaces in multilayer thin films.

In order to analyze experimental data on magnetic anisotropy constants, it is useful

to distinguish volume and surface/interface contributions. This yields  $K = K_{eff} = K_V + 2K_i/t$  (2.20), for the average magnetic anisotropy  $K$  and a magnetic layer thickness  $t$  [68]. The prefactor 2 is taken into account assuming a magnetic layer is surrounded by nonmagnetic layers from two sides. Rewriting the Equation 2.20 yields

$$t \cdot K_{eff} = t \cdot K_V + 2K_i \quad (2.21)$$

Plotting the  $t \cdot K_{eff}$  product versus Co thickness in the Co/Pd multilayers allows to determine the volume and surface/interface contributions as shown in Figure 2.7. It turns out that below a critical thickness  $t_C$ , Cobalt layer reorients its magnetization to the perpendicular direction.

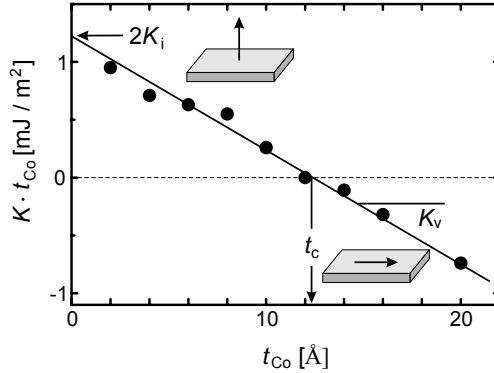


Figure 2.7: Magnetic anisotropy study of a Co thin film layer in a Co/Pd multilayer as a function of Co thickness. The slope of the fit line gives the volume contribution  $K_V$  and the zero crossing amounts to  $K_i$  [43]. (Data taken from [71].)

Experimental studies on Co/Pd multilayers grown in different crystallographic orientations as well as in polycrystalline form show that perpendicular magnetic anisotropy is an intrinsic property of the interface of ultrathin Cobalt layers [83]. However, the interface quality can strongly influence PMA from the translation symmetry point of view. In case of sharp interfaces, a difference arises in the chemical bonding of ferromagnetic atoms which results in uncompensated orbital moments. These orbitals can generate an orbital momentum aligned in a direction that depends on the bonding strength between the ferromagnetic (FM) and paramagnetic (PM) atoms. For the onset of PMA in heterostructures or multilayers, one can expect a stronger bonding between FM-PM than FM-FM [84].

## 2.4 Coupling mechanisms in magnetic multilayers

When a magnetic layer is brought into direct contact with another, the two layers will magnetically align parallel due to direct exchange coupling of the moments. For most applications, however, adjacent magnetic layers are separated using thin barrier or spacer films. In such a case, the relative alignment of the layers is determined by various mechanisms (see Figure 2.8), which are discussed below.

### Pinhole coupling

Pinhole coupling is a direct exchange coupling mechanism which takes place in case of a discontinuous growth of the spacer layer in between two ferromagnetic layers (Figure 2.8(a)). This discontinuity leads to the direct contact and coupling between the layers [85]. This coupling is often encountered in sputtered multilayers where the spacer layer thicknesses are less than 2 nm.

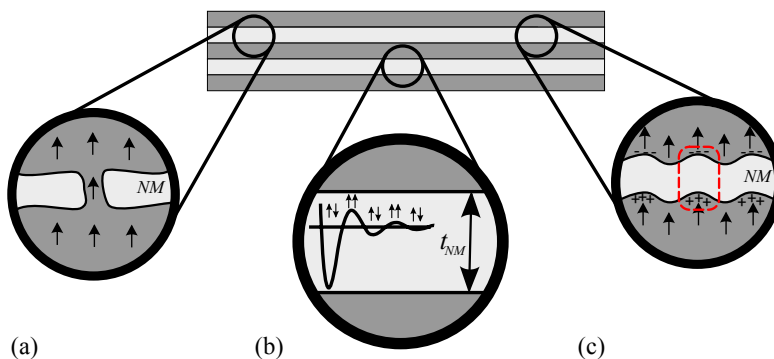


Figure 2.8: Schematics of coupling mechanisms in between perpendicular magnetic thin layers. (a) Parallel coupling through a pinhole due to discontinuous growth. (b) Oscillatory exchange coupling. Sign of the coupling determined by the thickness of spacer layer. (c) Neel's orange peel coupling. In-phase waviness of the rough interface creates magnetic "charges" that results in dipolar coupling. Sign of the coupling depends on the strength of interface anisotropy [86].

### Oscillatory exchange coupling

RKKY interaction (named after Ruderman, Kittel, Kasuga and Yosida) is an example of indirect exchange mechanism which is mediated by the conduction electrons. RKKY is the origin of the oscillatory exchange coupling observed in magnetic multilayers with a non-magnetic conducting spacer [87]. The thickness of the spacer layer plays a key role in determining the strength and the sign of interaction (see Figure 2.8(b)), which



leads to either parallel or anti parallel coupling [88]. According to equation:

$$J_{RKKY}(R) \propto \frac{x \cos x - \sin x}{x^4} \xrightarrow{x \rightarrow \infty} \frac{1}{x^3} \quad (2.22)$$

the strength of the RKKY interaction vanishes quickly by the spacer layer thickness  $x$ , and it is usually dominant in the range of a few nanometers.

### Néel coupling

Néel coupling, commonly known as *orange-peel* coupling, is another type of indirect coupling which emerges as a result of interface roughness of neighboring ferromagnetic layers. In-phase waviness in the structural geometry results in creation of magnetic poles along the film surface favoring the parallel alignment of magnetization. Due to the misalignment of interfacial anisotropy axes, the magnetization spatially oscillates over the wavy interface. It was reported that orange-peel coupling favors parallel or antiparallel coupling in perpendicular magnetic layers depending on the strength of anisotropy, see Figure 2.8(c). A comprehensive model can be found in the study of Moritz et al. on Co/Pt multilayers [86].

## 2.5 Magnetic domains

Magnetic domains are regions in a ferromagnetic materials where a number of magnetic moments align parallel. Each magnetic domain locally exhibits saturation magnetization ( $M_S$ ) of the material. Magnetic orientations of the surrounding domains do not necessarily align parallel, and therefore, the overall magnetization can cancel out in the absence of the applied field. Between two adjacent domains, magnetic moments gradually rotate from one direction to another. These boundaries are called domain walls. In this thesis, explanation of these concepts will be restricted to perpendicularly magnetized thin films.

### 2.5.1 Domain formation

The division of a magnetic material into the magnetic domains arises from the balance of the contributions of energetic terms. Homogeneously magnetized sample generates a magnetic stray field that yields a higher magnetostatic energy over the volume (Figure 2.9(a)). Therefore, magnetization breaks into domains in order to minimize this magnetostatic energy (Figure 2.9(b)). On the other hand, formation of domain walls costs energy in terms of exchange and anisotropy energies.

The balance between the magnetostatic energy and domain wall energy determines

the domain state. Forming domain walls is energetically unfavorable, below a *critical single-domain radius*, defined as  $R_{sd} \approx 36\sqrt{AK}/\mu_0 M_s^2$  for spherical magnetic materials [38]. In case of Co/Pt multilayer nanopillars, the single-domain condition is met when the radius is  $\sim 50$  nm.

In perpendicularly magnetized thin films, band (stripe) domains are the most notable domain structures observed. Band domains, as proposed by Kooy and Enz [89], are in the form of parallel bands with alternating magnetization, where the width of the bands follows the minimization of wall energy and stray field energy. Yet another type of domain structure is the magnetic bubble, which is observed when the anisotropy energy dominates the demagnetization energy. In this case, band domains transform into cylindrical domains under an applied field. The isolated bubbles require this applied field to be stable.

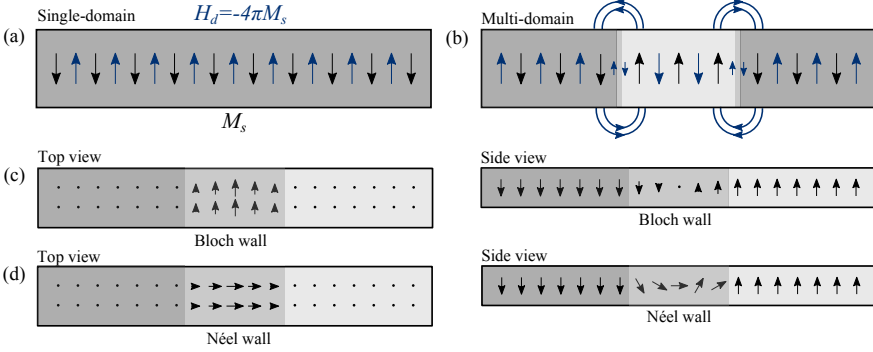


Figure 2.9: Illustration of minimization of stray field of perpendicularly magnetic thin films and types of domain walls (not to scale). (a) Stray field gives rise to a higher demagnetizing field ( $H_d = -4\pi M_s$ ) in homogeneously magnetized layers, as depicted by blue arrows. (b) Stray field mostly reduces after the magnetization breaks into domains. Domain wall types in thin magnetic films with perpendicular anisotropy are shown in the right part. In-plane component of magnetization is parallel to the domain wall in (c) Bloch-type walls and is perpendicular to the wall in (d) Néel-type walls [90].

### 2.5.2 Domain walls

In perpendicularly magnetized samples, there can be only up- and down-domains which are magnetized homogeneously and pointing in opposite directions due to the uniaxial anisotropy. These domains are separated by 180 degree domain walls. There are basically two types of domain walls; Bloch and Néel walls. In the case of a Bloch wall, the magnetization remains parallel to the wall and rotates  $180^\circ$  in the transition region as shown in Figure 2.9(c). On the other hand, the in-plane component of mag-

netization is perpendicular to the domain wall in the Néel-type walls (Figure 2.9(d)). It should be noted that Néel type domain walls give rise to magnetic “charges” which scale proportional to the film thickness. Thus, the Néel walls form in relatively thin layers. In Figure 2.10 (a), the domain wall energy ( $\gamma$ ) of a nanocomposite alloy film is plotted as a function of film thickness. Néel-type wall is energetically favorable below 50 nm film thickness.

### 2.5.2.1 Domain wall width

Domain wall width is determined by two competing energies, namely; exchange energy and anisotropy energy. For a non-parallel spin alignment, as it appears in the domain wall, the exchange energy amounts to  $E = -2JS^2 \cos \theta$  (2.23), where  $\theta$  is the angle between adjacent spins. This energy can be minimized when the angle  $\theta$  is kept small which yields thicker domain walls. On the other hand, the effective anisotropy energy will not favor thicker walls, since the amount of spins which are misaligned from the anisotropy axis is higher. Considering these two contributions, the width of a Bloch wall is given as:

$$\delta_B = Na = \pi\sqrt{A/K} \quad (2.24)$$

where  $a$  and  $N$  are lattice constant and number of spins involved in the domain wall.  $A$  and  $K$  are the exchange stiffness and the effective anisotropy constant, respectively [43]. In thin films, the effect of magnetostatics becomes more dominant, which also influences the Néel wall width as follows.

$$\delta_N = \pi\sqrt{A/K_{Sh}} = \pi\sqrt{A/2\pi M_s^2} \quad (2.25)$$

The film thickness dependences of Bloch and Néel walls are plotted in Figure 2.10 (b).

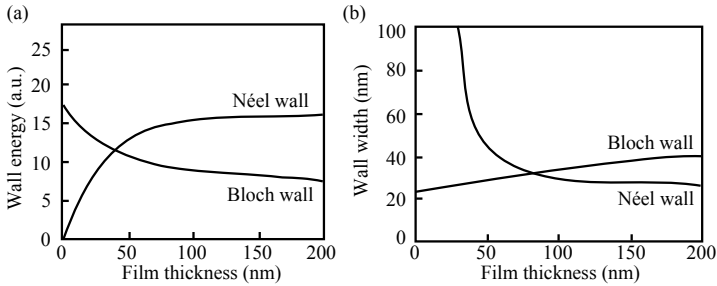


Figure 2.10: Calculated domain wall parameters for  $\text{Fe}_{40}\text{Co}_{40}\text{Nb}_4\text{B}_{13}\text{Cu}$  nanocomposite alloy. (a) Wall energy, (b) wall width as a function of film thickness. Figure taken from [91].

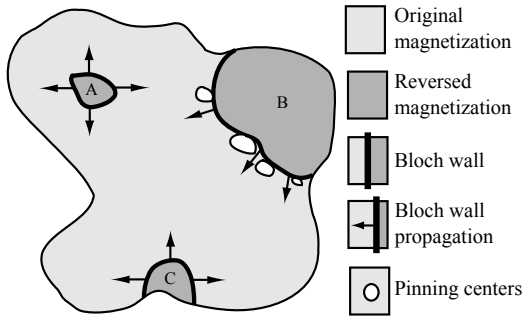


Figure 2.11: Domain wall motion during magnetization reversal. ‘A’ is a domain nucleated at a defect or due to a spontaneous thermal fluctuation. ‘B’ is a reverse domain which is trapped by pinning centers. ‘C’ is a domain nucleated at a surface distortion. Figure taken from [36].

### 2.5.2.2 Coercivity of domain walls

In an ideal magnetic material, domain walls can move freely in an external field. Walls with high surface energies tend to remain planar and the wall motion is reversible. In real materials, however, domain walls interact with the imperfections of the crystal structure, i.e., inclusions, dislocations and grain boundaries. As a result of this, the domain wall motion is inhibited by pinning centers unless the pinning energy is overcome. Then, wall motion is no longer reversible [92, 93].

Inclusions are normally formed by foreign atoms trapped inside the structure. In high-purity sputtered multilayers fabricated for this study, such inclusions are not expected. Nevertheless, due to the sputtering processes small-sized gaps on the order of a few Å can be present between the grains at the surface. Zeper *et al.* confirmed that the grain boundaries in Co/Pt multilayers can act as pinning centers [94]. Suzuki *et al.* showed that the coercivity of Co/Pt multilayers strongly depends on fabrication conditions [95].

Inclusions may have magnetic poles at the interfaces which repel an approaching domain wall and decelerate the domain wall motion [93]. If a sufficiently strong magnetic field is provided, the domain wall will leap forward to another inclusion, in other words to another pinning center. In heterogeneous systems, pinning centers are associated with irregularities in domain wall energy profile,  $d\gamma/dx$ .

### 2.5.3 Magnetic hysteresis

When a magnetic field is applied upon a magnetic material in a multi-domain state, the magnetic domains start to align in the direction of the applied field. Eventually, the domains completely disappear, the material reaches the saturation magnetization ( $M_S$ ) and transforms to a single-domain state. The field-induced magnetization reversal in thin films, however, does not proceed by coherent spin rotation, because the

defects in real films affect the coercivity by generating energy barriers for both domain nucleation and domain wall propagation [96].

In the absence of an applied field, the magnetic sample is in the remanence state. The remanent magnetization ( $M_R$ ) can be equal to the saturation magnetization (100% remanence). In such case, in order to break the sample into domains again field has to be applied in the opposite direction. The field required to flip the magnetization direction is termed as coercive field ( $H_C$ ). On the other hand, the remanence could be smaller than the saturation and the sample gradually turns into a multi-domains state. The response of the magnetization to the applied field is shown by the  $M - H$  curve or so-called hysteresis curve (see Figure 2.12). A hysteresis curve gives information about basic magnetic properties of the material, e.g., the easy axis, magnetic hardness, magnetization reversal and etc.

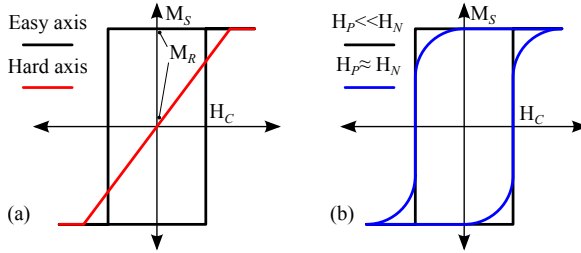


Figure 2.12: Typical hysteresis curve for thin films with uniaxial anisotropy.  $M_S$  and  $M_R$  stand for saturation and remanence magnetization values, respectively.  $H_C$  denotes coercive field. (a) Comparison of easy and hard axes. A square hysteresis loop is observed when the field is applied along easy axis ( $M_R/M_S = 1$ ). (b) Conditions between pinning field  $H_P$  and nucleation field  $H_N$  which determine the squareness of the loop.

The magnetization reversal in thin films is basically initiated by domain nucleation events followed by wall motion, which is controlled by presence of defects [97]. Domains can nucleate, when the magnetic field is applied up to a critical nucleation field,  $H_N$ . If there is a large amount of pinning centers, a larger field –defined by the pinning field  $H_P$ – has to be applied in order to proceed domain wall motion and reach saturation magnetization.

## 2.6 Precessional magnetization dynamics

Equilibrium and metastable states of a magnetic system are described with respect to the energy minima of the system. It can transform from one state to the other by means of external factors such as magnetic field [98], temperature, spin polarized

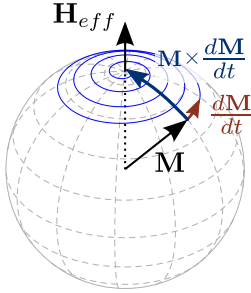


Figure 2.13: Precessional motion of magnetization vector around the effective magnetic field. A damping torque ( $\mathbf{M} \times \frac{d\mathbf{M}}{dt}$ ) acting on the precessing  $\mathbf{M}$  aligns the moments in the direction of external field.

currents [99, 100], electric field [101] as well as electromagnetic waves [32]. Conventionally, magnetization reversal is driven by a static magnetic field applied antiparallel to the initial direction of the magnetization under thermal excitation. The torque on the magnetization together with the damping term induce a damped precessional motion, which results in the reversal. The reversal time is mainly governed by the damping strength and precession period, and typically happens on a nanosecond timescale [35]. There is a second and a faster way for magnetization reversal, where a pulsed magnetic field is applied perpendicular ( $\mathbf{M} \perp \mathbf{H}$ ) to the magnetization during half of the precessional period [102, 103]. In practice, shorter and powerful magnetic field pulses are limited by the instrumentation. According to the experiments in SLAC, deterministic magnetization reversal is not possible for magnetic field pulses shorter than 2.3 ps [104].

The precessional motion of the magnetization vector is defined by a non-linear differential equation derived by Landau and Lifschitz. It has been later extended by Gilbert, and took the well-known form of Landau-Lifschitz-Gilbert (LLG) equation [105]. Modifications of the LLG equation are still being made upon the requirements of novel magnetic systems [106].

### 2.6.1 Landau-Lifschitz-Gilbert equation

The Landau-Lifschitz-Gilbert equation describes the temporal evolution of the magnetization vector with a constant magnitude and its field-induced precessional motion. The motion of a single magnetic moment can be expressed by using the semi-classical approach, which connects the time derivative of the angular momentum to the magnetic torque exerted on the magnetic moments considering  $\boldsymbol{\mu} = \gamma \mathbf{L}$ . It follows:

$$\frac{d\boldsymbol{\mu}}{dt} = -|\gamma| \boldsymbol{\mu} \times \mathbf{H} \quad (2.26)$$

where  $\gamma$  represents the gyromagnetic ratio for free electrons. The frequency of this

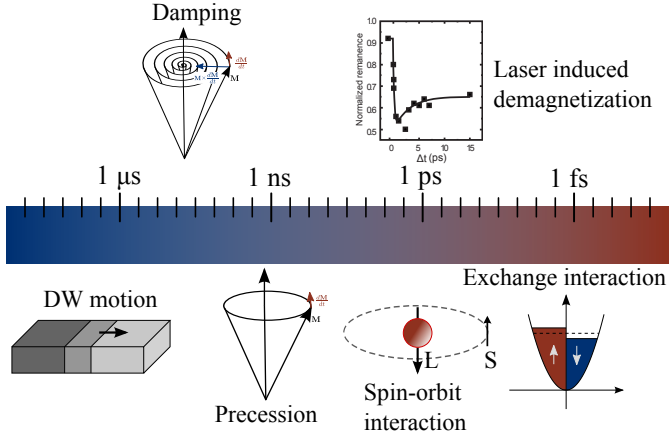


Figure 2.14: Fast and ultrafast timescales in magnetism.

precession is a function of the external magnetic field and is given as  $\omega_L = -|\gamma|H$ . For an external field of 1 Tesla, a full precession of a spin takes 36 ps [35]. Observations show that when magnetic moments form a continuum, the magnetization does not precess infinitely as denoted in Equation 2.26. Instead, the precessional motion is damped. Therefore, a damping term must be added in the form of an additional torque perpendicular to the precessional torque and perpendicular to  $\mathbf{M}$ . The more realistic form of the equation describing the magnetization motion is the LLG equation and is given as follows [35]:

$$\frac{d\mathbf{M}}{dt} = \underbrace{\gamma(1 + \alpha^2)(\mathbf{M} \times \mathbf{H}_{eff})}_{\text{precessional term}} + \underbrace{\frac{\alpha}{|\mathbf{M}|} \left( \mathbf{M} \times \frac{d\mathbf{M}}{dt} \right)}_{\text{damping term}} \quad (2.27)$$

where  $\alpha$  is the phenomenological Gilbert damping parameter and  $\mathbf{H}_{eff}$  is the effective magnetic field, which is composed of a number of energetic terms such as exchange energy, anisotropy energy, dipolar energy and Zeeman energy.

## 2.7 Magneto-optical effects

Magneto-optics deals with the phenomena which occur as a consequence of interaction between light and matter under applied magnetic field. In the case of spontaneous magnetization these effects may also appear in the absence of magnetic fields. Michael Faraday first discovered the magneto-optical effect when observing the polarization rotation changes of the light transmitted through a transparent medium under magnetic field [107]. This phenomenon, known as Faraday effect, did not even lose any

importance over the years. Inverse Faraday effect (IFE), opposite to Faraday effect, induces a magnetic field on the metallic surface when a circularly polarized light beam is transmitted through the material [108, 109].

Magneto-optical Kerr effect (MOKE) is yet another significant magneto-optical phenomenon discovered about 30 years later than the Faraday effect [110]. It describes the polarization rotation of the light reflected from the magnetic surfaces. Since then, a number of magneto-optical phenomena, for example, Zeeman [111], Voigt [112] and Cotton-Mouton [113] effects, has been discovered. For a general overview, a reader is referred to Oppeneer's book chapter [114].

MOKE is particularly important for this thesis, since our perpendicularly magnetized Co/Pt multilayers were grown on non-transparent and reflecting silicon substrates. Therefore, we employed MOKE in polar geometry in order to probe the magnetic properties of these multilayers. In this section, we describe the polar MOKE (p-MOKE).

### 2.7.1 Polarized light

The planar wave solution of the electromagnetic radiation is expressed in terms of the  $\mathbf{E}$  and  $\mathbf{H}$  fields which are perpendicular with respect to each other.

$$\mathbf{E} = \mathbf{E}_0 \exp i(\mathbf{k} \cdot \mathbf{r} - \omega t) \quad (2.28)$$

$$\mathbf{H} = \mathbf{H}_0 \exp i(\mathbf{k} \cdot \mathbf{r} - \omega t) \quad (2.29)$$

When  $\mathbf{E}_0$  and  $\mathbf{H}_0$  are constant vectors, the wave or light is said to be linearly polarized (LP). If the electric field vector rotates around the propagation axis with an angular velocity  $\omega$  of the light, then the light is circularly polarized. The direction of the rotation determines the helicity of the light polarization, i.e., right circularly polarization (RCP) and left circularly polarization (LCP). Linearly polarized light can be thought of as composed by the superposition of RCP and LCP lights with equal amplitudes.

#### 2.7.1.1 Jones formalism

The Jones formalism is a powerful tool to describe the polarization state of the light, as well as a tool for solving polarization problems in optical systems. In this notation, the polarization state of light is described by a two-dimensional vector ( $\mathbf{J}$ ) and any optical element is represented by a  $2 \times 2$  matrix ( $\mathbf{T}$ ). In order to model the effect of any optical element on the light polarization state, standard matrix operations will



apply.

$$\mathbf{J}^{out} = \mathbf{T} \cdot \mathbf{J}^{out} \quad (2.30)$$

The electric field component of a light wave is simply shown by the following Jones vector:

$$\mathbf{J} = \begin{pmatrix} E_x \\ E_y \end{pmatrix} = \begin{pmatrix} E_{x0}e^{i\phi_x} \\ E_{y0}e^{i\phi_y} \end{pmatrix} \quad (2.31)$$

Here, spatial and temporal phases are neglected for the polarization description. Therefore, Jones vectors for a linearly polarized light are simply represented by the following matrices.

$$\mathbf{J}_x = \begin{pmatrix} 1 \\ 0 \end{pmatrix}, \mathbf{J}_y = \begin{pmatrix} 0 \\ 1 \end{pmatrix}, \mathbf{J}_{45^\circ} = \frac{1}{\sqrt{2}} \begin{pmatrix} 1 \\ 1 \end{pmatrix} \quad (2.32)$$

Similarly, the vector notation for right and left circularly polarized light are:

$$\mathbf{J}_{RCP} = \frac{1}{\sqrt{2}} \begin{pmatrix} 1 \\ i \end{pmatrix}, \mathbf{J}_{LCP} = \frac{1}{\sqrt{2}} \begin{pmatrix} 1 \\ -i \end{pmatrix} \quad (2.33)$$

### 2.7.2 Magneto-optical Kerr effect

In order to study magnetic thin films in reflection geometry, magneto-optical Kerr effect (MOKE) is one of the most effective methods. There are three basic geometries in MOKE measurements regarding the orientation of the magnetization vector. On one hand, the magnetization can be perpendicular or parallel to the film surface. These two geometries are called as polar and longitudinal, respectively. On the other hand, magnetization can be parallel to the surface, but perpendicular to the reflection plane. This geometry is the transverse MOKE, where the polarization rotation is not observed, but only the intensity changes are measured.

The Co/Pt multilayers fabricated during this work show out-of-plane magnetization. Therefore, the polar MOKE geometry will be discussed in more detail. Polar MOKE is manifested in two ways when the light is reflected from a magnetic surface, as shown in [Figure 2.15](#). First, the polarization of linearly polarized light is rotated by a small angle  $\theta_K$ , and second, it becomes elliptical. The Kerr rotation,  $\theta_K$  is described as a complex quantity. The imaginary part of  $\theta_K$  is called the Kerr ellipticity. The rotation and ellipticity both originate from the fact that linearly polarized light is composed of two circular modes with refractive indices of  $n_+$  and  $n_-$ . These two modes undergo different magneto-optic response resulting in different propagation and absorption. It is important to note that this reduced symmetry is due to spin-orbit coupling [115].

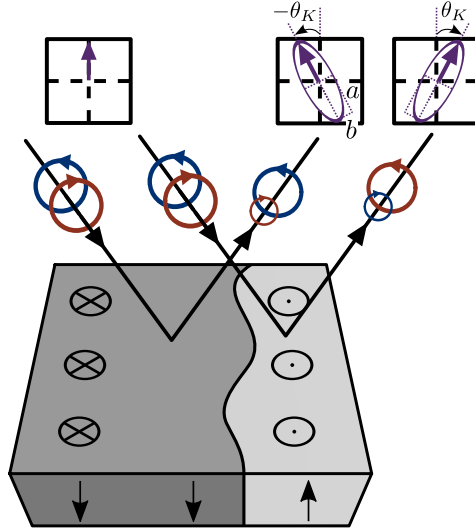


Figure 2.15: Schematics of Kerr rotation and Kerr ellipticity in polar geometry. Circular birefringence of opposite helicities gives rise to an asymmetry in polarization and hence results in elliptical polarization. For two domains with opposite orientation, the Kerr rotations differ only in sign. The Kerr ellipticity is quantified by  $\eta_K = \arctan(b/a)$ .

The magneto-optical response, like the other material-dependent optical properties, is incorporated into the dielectric tensor  $\epsilon(\omega)$  that describes the propagation of electric field in the material by:

$$\nabla \times (\nabla \times \mathbf{E}) = -\mu_0 \epsilon_0 \epsilon(\omega) \frac{\partial^2 \mathbf{E}}{\partial t^2} \quad (2.34)$$

with the plane-wave solution:

$$\mathbf{E} = \mathbf{E}_0 \exp[-i(\omega t - \mathbf{k} \cdot \mathbf{r})] \quad (2.35)$$

Generally, the magnetic permeability tensor  $\mu(\omega)$  has a very small effect on the optical phenomena, thus, the macroscopic properties of a material are described with the help of the dielectric permittivity tensor  $\epsilon(\omega)$ , which defines the proportionality between displacement vector  $\mathbf{D}$  and electric field  $\mathbf{E}$ .

$$\mathbf{D} = \epsilon_0 \epsilon(\omega) \mathbf{E} \quad (2.36)$$

In the simplest case the dielectric tensor can be written as follows.

$$\epsilon(\omega) = \epsilon_{xx} \begin{pmatrix} 1 & -iQm_z & iQm_y \\ iQm_z & 1 & -iQm_x \\ -iQm_y & iQm_x & 1 \end{pmatrix} \quad (2.37)$$

where  $Q$  is the magneto-optical constant given by  $Q = i\epsilon_{xy}/\epsilon_{xx}$  and  $m_i$  is the magnetization unit vector [116, 117]. It should be noted that the symmetry holds for  $\epsilon_{yx} = -\epsilon_{xy}$ . If the direction of magnetization  $\mathbf{M}$  points along one of the coordinate axes, rotation around this axis has no effect on the tensor. The dielectric tensor simplifies to the following form for the polar geometry ( $\mathbf{M} \parallel \hat{z}$ ):

$$\epsilon = \begin{pmatrix} \epsilon_{xx} & \epsilon_{xy} & 0 \\ -\epsilon_{xy} & \epsilon_{xx} & 0 \\ 0 & 0 & \epsilon_{xx} \end{pmatrix} \quad (2.38)$$

where diagonal elements are independent of  $\mathbf{M}$  and off-diagonal terms are functions of  $\mathbf{M}$  in first order [118]. All elements  $\epsilon_{ij}$  are complex and composed of real and imaginary parts. Solving the Maxwell's equation 2.34 for the plane waves assuming  $E_z = 0$  gives the matrix form which is diagonalized as below.

$$\begin{pmatrix} \epsilon_{xx} + i\epsilon_{xy} & 0 \\ 0 & \epsilon_{xx} - i\epsilon_{xy} \end{pmatrix} \begin{pmatrix} E_x + iE_y \\ E_x - iE_y \end{pmatrix} = 0 \quad (2.39)$$

Two eigenvectors correspond to right and left circularly polarized light with complex refractive indices,

$$N_{\pm}^2 = \epsilon_{xx} \pm i\epsilon_{xy} \quad \text{and} \quad \pm iE_x = E_y \quad (2.40)$$

with  $N = k/k_0$  describing the complex refractive indices of the circularly polarized light. The difference between both indices,  $\Delta N$  is extracted from Equation 2.40:

$$\Delta N = \frac{i\epsilon_{xy}}{\sqrt{\epsilon_{xx}}} \quad (2.41)$$

The refractive indices can be used to calculate the complex reflectivity (Fresnel coefficients) of right and left circularly polarized light separately.

$$r_{\pm} = \frac{N_{\pm} - 1}{N_{\pm} + 1} \quad (2.42)$$

Following Yokoyama *et al.* [119], the complex Kerr rotation can be expressed using

the Fresnel coefficients.

$$\Phi_K = \theta_K + i\eta_K \cong \frac{i}{2} \ln \frac{r_-}{r_+} \quad (2.43)$$

For a linearly polarized incident light, the reflection will be elliptically polarized as depicted in Figure 2.15. The Kerr rotation  $\theta_K$  defines the rotation of the major axis and the Kerr ellipticity  $\epsilon_K$  is the ratio of minor and major axes of ellipsoid [118]. The change in polarization is due to unequal phases, whereas the ellipticity is due to unequal amplitudes of the reflected right and left circularly polarized waves [114].

### 2.7.2.1 Microscopic description of MOKE

Macroscopically, the origin of MOKE is attributed to circular birefringence. The absorption spectra of left and right circularly polarized light are closely related to the electronic energy levels in the simultaneous presence of **exchange splitting** and **spin-orbit splitting**. For 3d transition metals, optical transitions from the 3d states to the 4p states are determined by the selection rules.

$$\Delta l = \pm 1, \Delta m_l = \pm 1, \Delta s = 0 \quad (2.44)$$

The transitions from occupied d states to unoccupied p states are displayed in Figure 2.16. The arrows show allowed d→p transitions upon excitation by left and right circularly polarized light, where the sign of  $m_l$  selection rule (magnetic quantum number) is determined by the photon helicity [120, 121]. The asymmetry between left and right helicities for the same allowed transitions arises from the different photon energies required for the excitations. In reality, the asymmetry in the absorption is of the order of a few percent [120].

### 2.7.2.2 Inverse Faraday effect

The effect of circularly polarized light on the angular momentum of magnetic systems has been predicted many decades ago [123]. This effect is just the opposite of the Faraday effect, where linearly polarized light undergoes a polarization rotation and ellipticity upon interaction with magnetic systems. Inverse Faraday effect (IFE) is, nowadays, at the core of discussions about the origin of the optically induced magnetization reversal phenomenon.

Here, only the results are given from Hertel's paper where a simplified derivation of IFE is provided [124]. In this work, the interaction between the magnetic system and a high-frequency (HF) electromagnetic wave is treated by a microscopical approach based on Drude's free electron gas approximation. The HF electromagnetic wave

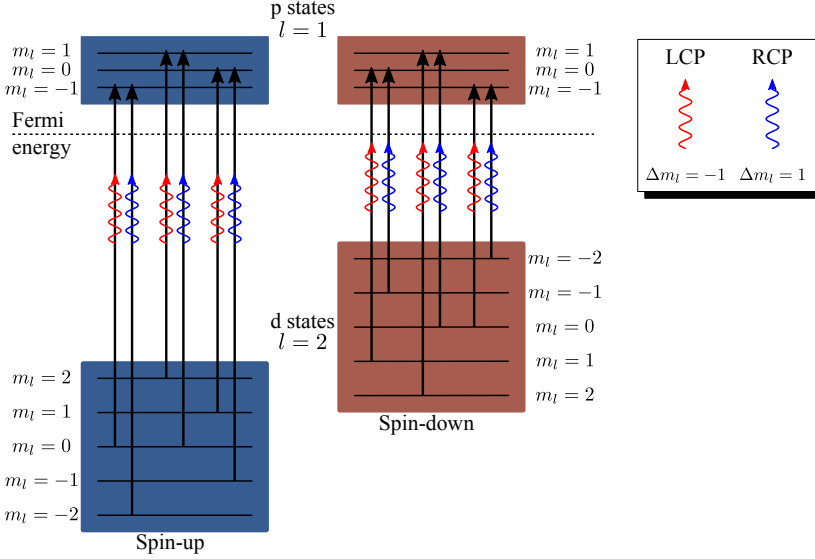


Figure 2.16: Transition from d-states to p-states obeying to dipole selection rules. The exchange splitting for d-states are shown, while for p-states are neglected. Reproduced from [120, 122].

generates microscopical solenoidal currents  $\mathbf{j}_m$ , where  $\mathbf{j}_m = \nabla \times \mathbf{M}$ . Hence, the resulting magnetization  $\mathbf{M}$  is expressed as

$$\mathbf{M} = -\frac{i\epsilon_0 e \omega_p^2}{4m\omega^3} [\hat{\mathbf{E}} \times \hat{\mathbf{E}}^*] \quad (2.45)$$

where  $\omega_p$  is the plasma frequency. It is noted that the last term in Equation 2.45 is zero in case of linear polarization, but is written as

$$\hat{\mathbf{E}} \times \hat{\mathbf{E}}^* = \pm i |\mathbf{E}|^2 \cdot \hat{\mathbf{z}} \quad (2.46)$$

in case of circular polarization propagating in the direction of  $\hat{\mathbf{z}}$ . The magnetization is expected to be parallel to the propagation and the sign is determined by the light helicity. It is reported that circularly polarized laser pulses can generate IFE-fields that last about 100 femtoseconds [124]. The estimated IFE-field strength varies from 0.1 to 30 T in the literature [108]. The models suggest that the IFE-field lifetime is proportional to the light pulse duration [108].

### 2.7.3 Magneto-optical effects in the x-ray region

Magneto-optical effects in the x-ray region are analogous to the conventional (visible range) effects with an additional capability of reaching characteristic absorption edges of electronic core levels owing to the shorter wavelengths. Close to the absorption edges, magneto-optical effects are appreciably enhanced by transitions from atomic core levels to conduction states [115]. However, in order to employ x-rays in the experiments, generation of circularly polarized x-rays and appropriate optics are needed. Synchrotron radiation [125] as well as table-top higher-harmonic-generation (HHG) [126, 127] sources are widely used for generation of x-rays for magnetic measurements.

#### 2.7.3.1 X-ray absorption and XMCD

In the x-ray absorption process, a photon impinging on a material transfers its energy and angular momentum to an electron in the core level, which is excited to the empty states above the Fermi level. The transition probability of an electron between the initial and final states is calculated by Fermi's Golden Rule.

$$P_{f,i} = \frac{2\pi}{\hbar} |\langle \psi_f | H | \psi_i \rangle|^2 \delta(E_f - E_i - \hbar\omega) \quad (2.47)$$

Energy conservation in the process is expressed by the  $\delta$ -function. The transition probability is determined by the transition matrix element  $|\langle \psi_f | H | \psi_i \rangle|$ . The above-mentioned (Eqn. 2.44) dipole selection rules are also obtained according to the Golden Rule.

For a typical ferromagnet, transitions take place between spin-orbit split 2p states and exchange split 3d states. The microscopic origin of dichroic effect, therefore, involves the interplay of spin-orbit coupling and exchange interaction. The angular momentum associated with circularly polarized light interacts with the spin of excited electron at the core level through the spin-orbit interaction. In Figure 2.17, x-ray absorption process is shown for a *strong* ferromagnet with one filled spin channel. Thus, 2p→3d transitions are only possible for the partially-filled (spin-up) band. Right and left circularly polarized light excite different proportions of electrons at the two edges [128]. Specifically, left circularly polarized (LCP) light excites 75% of spin-down and 37.5% of spin-up electrons at the 2p<sub>1/2</sub> level, and 25% of spin-down and 62.5% spin-up electrons at the 2p<sub>3/2</sub> level. It means that absorption spectra differ for opposite helicities which gives rise to magnetic circular dichroism. The dichroism in the initial absorption stage is transferred to the emitted electrons. The photoexcited

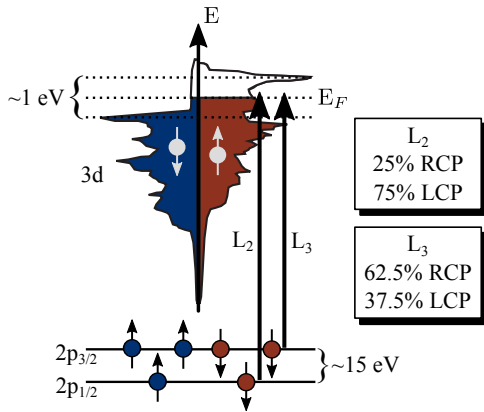


Figure 2.17: Schematics of L-edge x-ray absorption upon circularly polarized light absorption for a *strong* ferromagnet with one filled spin channel. The fraction of excited electrons for opposite helicities are given for  $L_2$  and  $L_3$  transitions [35].

2p electron leaves a core hole in the 2p shell which relaxes within a certain lifetime either by fluorescence or Auger emission.

X-ray magnetic circular dichroism (XMCD) contrast is obtained either using opposite light polarizations with a fixed magnetization or vice versa. XMCD spectra of Co/Pt multilayer, shown in Figure 4.18, were obtained using fixed helicity and opposite magnetic fields. XMCD presents element selectivity as well as direct and independent measurement of spin and angular magnetic moments in ferromagnetic materials [129]. Therefore, it is necessary to tune the x-ray energy to the absorption edge of the studied element.

# Chapter 3

## Review of ultrafast magnetism phenomena and all-optical switching

This chapter consists of two sections which are related to ultrafast demagnetization and magnetization switching processes. It has been known for two decades that femtosecond laser pulses can completely quench the magnetization within sub-picosecond timescales. Since 2007, magnetization reversal have been demonstrated in a limited number of materials in thin film form. The first part is devoted to the mechanisms of the ultrafast demagnetization process. The second part covers the literature overview on all-optical magnetization switching in a broad aspect.

### 3.1 Optical excitation of magnetic metals

When a laser pulse impinge on the metallic surface, the energy of the photons is transferred to the electrons by absorption and highly energetic ( $\geq 1$  eV) electrons are created. Neglecting interfacial reflections and scattering events, the transmitted light intensity profile in a metal throughout a thickness  $d$  is given by Beer-Lambert law:

$$I(d) = I_0 \exp(-\mu d) \quad (3.1)$$

where  $\mu$  is the optical absorption coefficient proportional to the imaginary part of the refractive index. Upon absorption, photon energy instantly raises the temperature of the illuminated area depending on to the laser intensity profile. The temperature profile introduced by the impinging laser pulses will spread by the heat diffusion and smooths within time. In case of a uniform thin film, the heat diffusion equation may



be expressed in spherical coordinates by

$$\frac{\partial}{\partial t} T(\mathbf{r}, t) = \frac{D}{r} \frac{\partial}{\partial r} \left[ r \frac{\partial}{\partial r} T(\mathbf{r}, t) \right] \quad (3.2)$$

where  $D$  is the thermal diffusivity [90]. The analytical solution to this equation indicates that the temperature profile remains Gaussian, but its size increases with time governed by diffusivity [90].

$$r_0(t) = \sqrt{r_0^2 + 4Dt} \quad (3.3)$$

### 3.2 Laser-induced ultrafast magnetization dynamics

The development of femtosecond lasers and precise instruments allowed the investigation of the sub-picosecond magnetization dynamics. Laser pulses can be used as either pump or probe as well as both together in so-called pump-probe techniques, described in Section 5.2. The earliest considerable achievement has been made by Beaurepaire *et al.* on the ultrafast dynamics of nickel using 60 femtosecond linearly polarized pulses [32]. The observation was interpreted as ultrafast demagnetization of ferromagnetic nickel within a few picosecond (see Figure 3.1), which is much faster than the precession period of the magnetic moments. The demagnetization is followed by relatively slow recovery to the remanence. This result has been confirmed by several other groups by means of magneto-optical responses as well as time-resolved photoemission studies [130, 131]. The discussions finally reached an agreement that the demagnetization time  $\tau_M$  is around 100 fs for elementary transition metals [132].

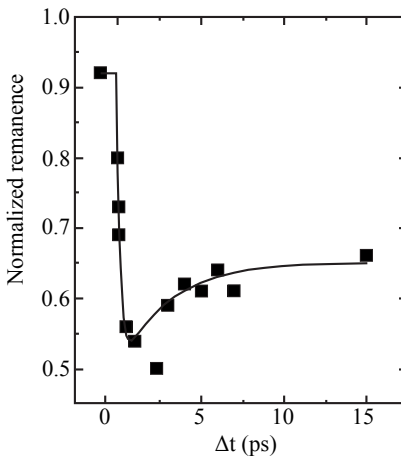


Figure 3.1: Ultrafast demagnetization of polycrystalline nickel thin films probed using time resolved MOKE [32]. The magnetization drops within 2 ps and recovers on a relatively large time-scale.

### 3.2.1 Phenomenological descriptions

Ultrafast demagnetization dynamics of a magnetic system can be explained by separating into the subsystems of electrons, spins and lattice. These three subsystems (see Figure 3.2) show dynamic responses upon femtosecond laser excitation within different, but partially overlapping timescales.

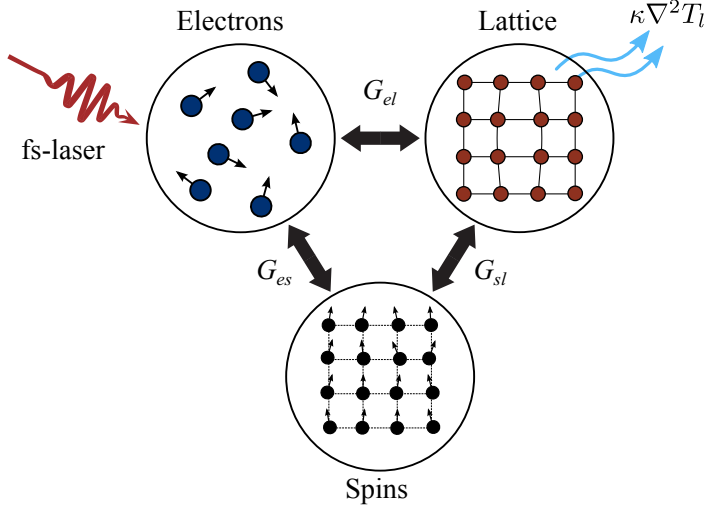


Figure 3.2: Mutually interacting heat reservoirs in a ferromagnetic system. The double-sided arrows denote the coupling, which allows angular momentum and energy exchange between subsystems.

In the framework of the three-temperature model (3TM), electrons, spins and lattice are treated as heat reservoirs, which are coupled to each other and can exchange thermal energy [32]. The coupling between the reservoirs is formulated by the following differential equations,

$$\begin{aligned}
 C_e(T_e) \frac{\partial T_e}{\partial t} &= G_{el}(T_l - T_e) + G_{es}(T_s - T_e) + P(\mathbf{r}, t), \\
 C_l(T_l) \frac{\partial T_l}{\partial t} &= G_{el}(T_e - T_l) + G_{sl}(T_s - T_l) - \kappa \nabla^2 T_l(\mathbf{r}, t), \\
 C_s(T_s) \frac{\partial T_s}{\partial t} &= G_{es}(T_e - T_s) + G_{sl}(T_l - T_s)
 \end{aligned} \tag{3.4}$$

where  $P(\mathbf{r}, t)$  describes the initial excitation from the laser pulse,  $\kappa \nabla^2 T_l(\mathbf{r}, t)$  is the term for heat diffusion within the lattice and  $G_{el}, G_{es}, G_{sl}$  are coupling constants between reservoirs at temperatures  $T_l, T_s$  and  $T_e$ .

The demagnetization process described by 3TM assumes that electrons constitute

the only system, which is able to respond to electromagnetic excitation at optical frequencies. Therefore, an impinging fs-laser pulse initially excites the electron subsystem [133]. This gives rise to a rapid ( $< 500$  fs) increase of the temperature, the so-called electron thermalization, due to the electron-electron scattering. Owing to the small heat capacity, the electronic temperature  $T_e$  may reach several hundreds of Kelvin [35]. In the transition metals, energy relaxation from electrons to the lattice takes a few ps [32]. Next, the heat is distributed (10-1000 ps) to spin and lattice subsystems such that  $T_e$ ,  $T_s$  and  $T_l$  are in thermal equilibrium at elevated temperatures. On the longer timescale, the illuminated area cools down by the diffusion of heat energy. 3TM does not answer the question what happens with the spins, although, a number of models provide a microscopic description of the spin subsystem, as listed in the following subsection.

The analytical solution of the rate equations in Equation 3.4 gives an insight to the time scales of dynamical processes. In a typical demagnetization curve, the most important parameters are demagnetization time ( $\tau_M$ ) and relaxation time ( $\tau_E$ ). The relaxation time can be governed by multiple mechanisms within electrons-electrons and electrons-phonons simultaneously. In order to fit a demagnetization curve, various functions are used in the literature. For a detailed review of these functions, we refer the PhD thesis of Giovannella to the readers [134].

The temperature evolution of the spin subsystem can be used to follow the demagnetization curve. Using the assumptions of Koopmans [135], the fitting function can be given as:

$$\frac{\Delta M(t)}{M_0} = G(t) \otimes H(t) \left[ A_2 - \frac{(\tau_E A_1 - \tau_M A_2) e^{-\frac{(t-t_0)}{\tau_M}} + \tau_E (A_2 - A_1) e^{-\frac{(t-t_0)}{\tau_E}}}{\tau_E - \tau_M} \right] \quad (3.5)$$

where  $G(t)$  is a Gaussian function, which represents the temporal resolution of the laser pulses,  $H(t)$  is the Heaviside step function.  $A_1$ ,  $A_2$  are fitting coefficients associated with the magnetization change and the initial electron temperature rise, respectively [136]. On a long range, cooling by heat diffusion is described by the  $(\sqrt{t/\tau_0} + 1)^{-1}$  term. The fitting function takes the following form where  $\tau_0 \gg \tau_M, \tau_E$ .

$$\frac{\Delta M(t)}{M_0} = G(t) \otimes H(t) \left[ \frac{A_2}{\sqrt{1 + \frac{t}{\tau_0}}} - \frac{(\tau_E A_1 - \tau_M A_2) e^{-\frac{(t-t_0)}{\tau_M}} + \tau_E (A_2 - A_1) e^{-\frac{(t-t_0)}{\tau_E}}}{\tau_E - \tau_M} \right] \quad (3.6)$$

Another widely used fitting function represents the early stage recovery of the mag-

netization with electron-phonon scattering [137]:

$$\frac{\Delta M(t)}{M_0} = G(t) \otimes H(t) \left[ A_1 \left( 1 - e^{-\frac{-(t-t_0)}{\tau_M}} \right) e^{-\frac{-(t-t_0)}{\tau_E}} + A_2 \left( 1 - e^{-\frac{-(t-t_0)}{\tau_E}} \right) \right] \quad (3.7)$$

In many cases, the electron-phonon interaction timescale,  $\tau_E$ , is not sufficient to simulate the long-term magnetization recovery. Therefore, an additional  $\tau_R$  term is added in order to model the phonon-phonon interaction. The quadruple exponential function is written as:

$$\frac{\Delta M(t)}{M_0} = G(t) \otimes H(t) \left[ A_1 \left( 1 - e^{-\frac{-(t-t_0)}{\tau_M}} \right) e^{-\frac{-(t-t_0)}{\tau_E}} + A_2 \left( 1 - e^{-\frac{-(t-t_0)}{\tau_E}} \right) e^{-\frac{-(t-t_0)}{\tau_R}} \right] \quad (3.8)$$

### 3.2.2 Microscopical descriptions

The mechanism of ultrafast demagnetization is explained above, although a full description of physical mechanisms has not been proposed yet. It is generally accepted that the overall process depends on the exchange of energy and angular momentum between electron, spin and lattice systems. Further information can be found in Ref. [49], and the other references therein.

#### Direct photon-spin interaction

Zhang and Hübner predicted that in the presence of spin-orbit coupling, the direct interaction between pump laser photons and spins could lead to light angular momentum transfer to the magnetic moments [138]. However, there is a strong controversy against this theory considering the number of absorbed photons, which are insufficient to quantitatively explain the magnitude of magnetization quenching [139]. In addition, experiments reported by Rhie *et al.* [140] showed that the exchange splitting in nickel quenches after the pump pulse has ceased.

#### Electron-electron interaction

The Coulomb interaction among electrons is interpreted as another mechanism of ultrafast demagnetization. Here, electron-electron interaction within the Elliot-Yafet (EY) scattering scheme is proposed for spin-lattice relaxation by Krauß *et al.* [141].

#### Electron-phonon spin-flip scattering

In 2005, Koopmans *et al.* introduced a Hamiltonian inspired by spin-flip scattering of electrons interacting with impurities or phonons [142]. Spin-flip scattering is responsible for the spin angular momentum transfer to the lattice. The spin-flip scattering is of the EY type, namely, each electron-phonon scattering event may lead to a

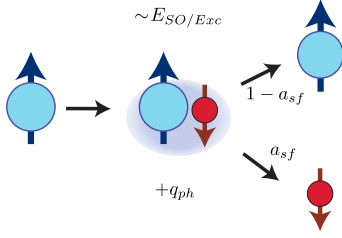


Figure 3.3: Schematic representation of Elliott-Yafet type electron-phonon spin-flip [144].

spin flip. This mechanism states that the electron spin is no longer a good quantum number because of SOC, and it is found in a mixed state of spin-up and spin-down ( $|\Psi\rangle = a|\Psi_{\uparrow}\rangle + b|\Psi_{\downarrow}\rangle$ ) during scattering process. For a given spin state,  $a$  and  $b$  are determined by a spin-flip scattering probability  $\alpha_{sf}$  term determined by spin-orbit coupling.

Koopmans *et al.* merged the EY type spin-flip channel with the three-temperature model (3TM), which led to the microscopic three-temperature model (M3TM) [143].

### Superdiffusive spin transport

Superdiffusive spin transport was proposed by Battiato *et al.* as a novel approach for the origin of ultrafast demagnetization [145, 146]. This model assumes magnetization quenching by spin-dependent transport of charge carriers out of the excited area as follows: After the laser illumination, electrons in quasi-localized d-bands are excited to sp-bands to gain mobility, while conserving their spin states [145]. Excited spin majority and minority electrons have different lifetimes [147]. Subsequently, electrons are drained out of the excited volume. The transport of the electrons is neither ballistic nor diffusive, but it lies in between the two models and is therefore called as superdiffusive. The difference in the lifetimes results in a larger mean free path for majority electrons and gives rise to the ultrafast demagnetization of the excited volume.

### 3.2.3 Summary

The above-mentioned models are based on different microscopical processes, and they all prove that it is possible to numerically obtain demagnetization times of the same order of magnitude. Although, a complete description of ultrafast demagnetization dynamics remains absent. In this work, estimation of characteristic time-scales is the solely important aspect independent of an explanation of the microscopical perspective.

### 3.3 All-optical switching

All-optical switching (AOS) denotes magnetization reversal by means of ultrashort optical pulses in the absence of external magnetic fields. All-optical switching appears in the literature also as *all-optical magnetization reversal* or *optically-induced magnetization reversal*. In this thesis the *AOS* abbreviation will be used due to the convention in the ultrafast magnetism community. All-optical helicity *dependent* switching (AO-HDS) represents the case where the magnetization reversal depends on the helicity of the incoming light pulses. On the contrary, switching can occur *independent* of helicity (AO-HIS) or even by means of linearly polarized pulses. The latter is termed as *toggle* switching, because the magnetization direction is flipped by each successive pulse.

#### 3.3.1 Early predictions of AOS

AOS was theoretically predicted by Hübner *et al.* who developed a model based on electronic transitions induced by coherent laser pulses [138, 148]. The excitation by the coherent laser pulses would give rise to transitions between two states without change of the spin state. The main idea was manipulating the spins at the excited state with a sufficiently magnetic field acting perpendicular to the magnetization. Hübner suggested this field to be supplied by spin-orbit interaction. However, there were shortcomings of the model with respect to exchange field and transition lifetime. In fact, the model assumes the transition lifetime to be infinitely long and neglects the exchange field in the transiently excited state [35].

An experimental confirmation of AOS was demonstrated by Kimel *et al.* on ferrimagnetic DyFeO<sub>3</sub> [149], which exhibits large magneto-optic coupling owing to the presence of Dy [35]. The experimental results presented in Figure 3.4 show two distinct processes: first, a helicity-dependent response of Faraday rotation following the femtosecond laser illumination, and second, oscillations of the Fe moments around the equilibrium position.

#### 3.3.2 All-optical switching in ferrimagnetic thin films

**Multi-pulse switching** The first deterministic all-optical switching (AOS) was demonstrated in 2007 by Stanciu *et al.* on 20 nm-thick GdFeCo ferrimagnetic alloy films using circularly polarized femtosecond laser pulses in the absence of external magnetic fields [33]. The experiment was performed using a laser beam with 800 nm wavelength, 40 fs pulse duration and 1 kHz repetition rate and by sweeping the laser

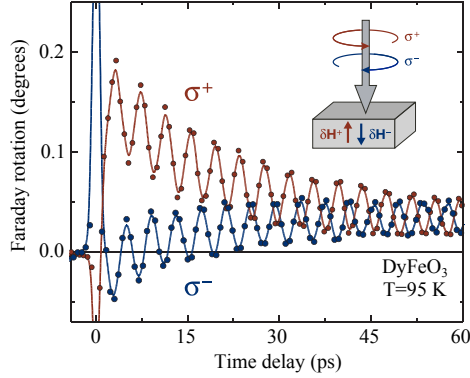


Figure 3.4: Magneto-optical response of DyFeO<sub>3</sub> after optical excitation with circularly polarized laser pulses [149].

beam at  $\sim 30 \mu\text{m/s}$  across the ground-state magnetic domains with different light polarizations. The magnetization direction of the illuminated area was determined by the helicity of the laser beam (see Figure 3.5). On the other hand, exposure of linearly polarized light yields a random distribution of dark and bright domains. The end spots of the lines remain demagnetized due to overheating by longer exposure times before the laser beam is turned off. Stanciu *et al.* further reported that multi-pulse AOS strongly depends on the laser fluence, such that central part of the Gaussian intensity profile yields thermal demagnetization by overheating whereas a ring-like switching pattern is observed at the outer perimeter as shown in Figure 3.6(a). In this experiment, linearly and circularly polarized laser beams are focused on a domain wall for a given time period. The experimental findings suggest that by reducing the laser fluence a spot can be switched without a thermally demagnetized core. Indeed,

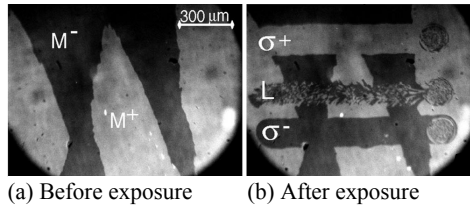


Figure 3.5: Magneto-optical microscopy image of GdFeCo before and after laser beam exposure. (a) Up and down magnetic domains (ground state) are depicted by  $M^+$  and  $M^-$ , respectively. (b) Domain pattern after exposure of right ( $\sigma^+$ ), left circularly ( $\sigma^-$ ) and linearly ( $L$ ) polarized laser beam ( $11.4 \text{ mJ/cm}^2$ ) from left to right at a speed of  $30 \mu\text{m/s}$ . The central part of the end-spots remains demagnetized, namely a combination of small up- and down-domains. Figure is adapted from [33].

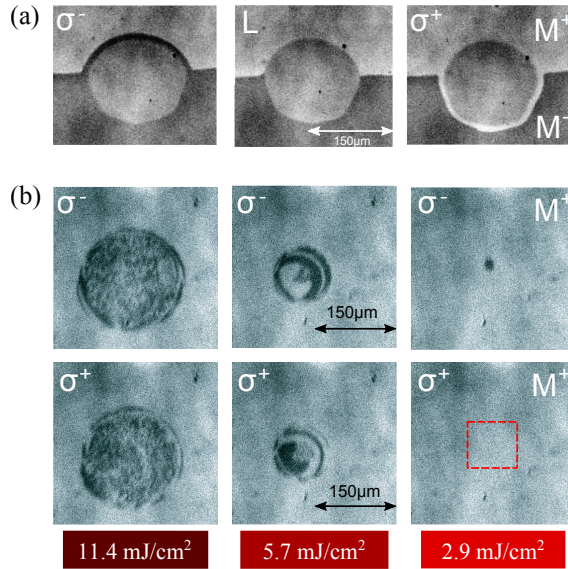


Figure 3.6: Magneto-optical microscopy images of AO-HDS in GdFeCo. (a) Ring-like switching is observed when the laser beam with a fluence of 11.4 mJ/cm<sup>2</sup> was focused on the domain wall. In all three cases, central parts are demagnetized. (b) Laser fluence dependence of AO-HDS after exposure to  $\sim 20$  pulses. Sample was initially saturated in the  $M^+$  state. At 2.9 mJ/cm<sup>2</sup> left circularly polarized light results in a complete switched spot, whereas right circularly polarized light has no difference (field depicted with dashed red box) since the background is already bright. Image adapted from [33].

when the laser fluence was gradually reduced down to 2.9 mJ/cm<sup>2</sup>, the laser exposure switched a homogeneously magnetized spot, as shown in Figure 3.6(b).

**Single-pulse switching** Yet another intriguing outcome from the publication of Stanciu *et al.* is helicity-dependent single-pulse all-optical switching [33]. In the experimental results shown in Figure 3.7, a laser beam of 2.9 mJ/cm<sup>2</sup> fluence was swept at higher speeds such that each pulse landed at distinct positions. Single laser pulses at this fluence level gave rise to *helicity-dependent* magnetization reversal.

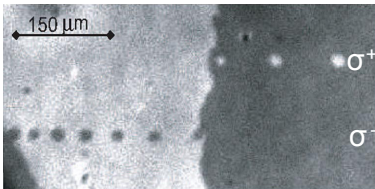


Figure 3.7: Magneto-optical microscopy images of AO-HDS using single pulses with 40 fs pulse duration. The laser fluence was about 2.9 mJ/cm<sup>2</sup>, which was also shown to be the minimum fluence required for switching in the previous study [33].



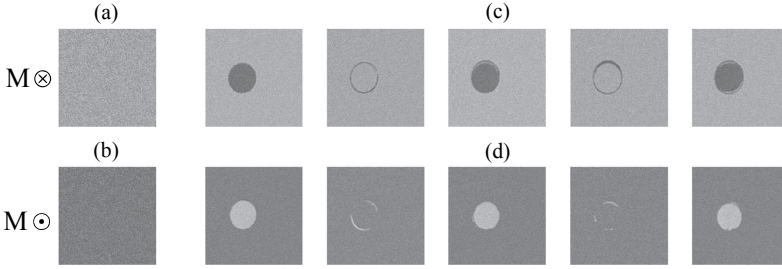


Figure 3.8: Demonstration of toggle switching in GdFeCo thin films using linearly polarized laser pulses (100 fs). (a) and (b) represent homogeneously magnetized up- and down-domain states. (c) and (d) show the magnetic response against a sequence of laser pulses impinging on the same position. Adopted from [150].

**Toggle switching** All-optical helicity-*independent* switching in GdFeCo ferrimagnetic thin films using single pulses, shortly ‘toggle switching’, was observed by Ostler *et al.* using magneto-optical imaging [150]. Here, circularly polarized single laser pulses with a fluence of  $2.25 \text{ mJ/cm}^2$  result in helicity-dependent switching. On the other hand, when the fluence is increased only by a small amount up to  $2.30 \text{ mJ/cm}^2$ , the effect of helicity is canceled out and each single pulse deterministically toggles the magnetization. Interestingly, the magnetization reversal can also be triggered with *linearly* polarized fs pulses (see Figure 3.8). This finding pointed to a thermally induced origin to the reversal mechanism instead of inverse Faraday effect. Very soon after, Radu *et al.* explained the mechanism of reversal of Gd and Fe sublattices using

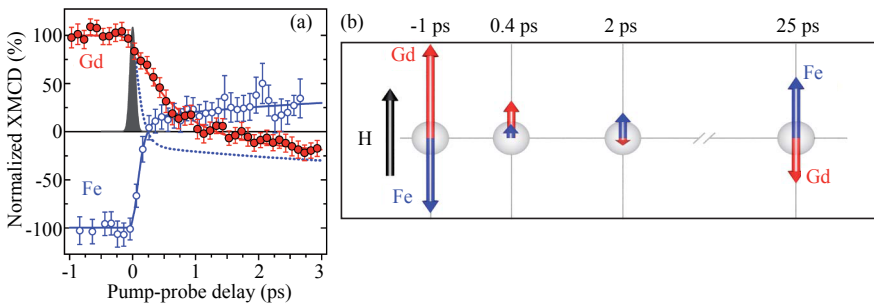


Figure 3.9: Transient ferromagnetic state in ferrimagnetic GdFeCo thin film. (a) Time-resolved XMCD signals at Gd and Fe edges show that Fe demagnetizes within the first 0.3 ps whereas Gd demagnetizes around 1.5 ps. (b) Illustration of time evolution of magnetization vectors based on atomistic spin model based calculations. Transient ferromagnetic-like state is observed in the first picoseconds. Later, Gd sublattice switches the magnetization according to the antiferromagnetic exchange between Fe sublattice.

laser pump - XMCD probe technique [151]. Figure 3.9 (a) shows the time-resolved XMCD signal at Fe ( $L_3$ ) and Gd ( $M_5$ ) absorption edges upon linearly-polarized laser pulses. The Fe sublattice demagnetizes and reverses rapidly within 300 fs, which is much faster than the response of the Gd sublattice (1.5 ps). Distinct demagnetization and reversal times of exchange-coupled Gd and Fe(Co) sublattices suggested a *transient ferromagnetic-like state* in GdFeCo. Calculations based on the atomistic spin model also confirmed the timescales for the demagnetization of each sublattice. The time evolution of magnetization vector is illustrated in Figure 3.9 (b).

### Dependence on sample system

All-optical switching was extensively studied on ferrimagnetic amorphous alloys such as GdFeCo, TbFe and TbCo, with a variety of atomic compositions. In the RE-TM alloys, the magnetization is the sum of two sublattices ( $M_{RE}+M_{TM}$ ). Thus, the net magnetization vanishes at a certain temperature called compensation temperature,  $T_M$ . Tuning the atomic composition, the compensation temperature, strength of the exchange coupling and magnetization can differ for ferrimagnetic alloys. We note that most of the samples given in Figure 3.10(a) exhibit  $T_M$  above room temperature, but it is not a general rule for switching.

Besides the RE-TM alloy systems [152–154], RE/TM multilayers [153] and RE-free synthetic ferrimagnets [153] were used in AOS experiments. It is mostly accepted for ferrimagnetic layers that the all-optical switching ability strongly depends on the material system. In Figure 3.10(b), various ferrimagnetic systems are shown depending on their magnetic responses, i.e., remanence magnetization  $M_R$ , against the laser illumination. The data presented in this view-graph indicates that a low-remanence criterion applies to ferrimagnetic layers. Furthermore, the occurrence of AOS can be controlled by tuning the  $M_R$  value by laser-induced heating or by substrate heating.

### 3.3.3 All-optical switching in ferromagnetic multilayers

The research of all-optical switching in ferromagnetic materials was driven by scientific curiosity as well as industrial considerations. Ferromagnetic materials consist of a single magnetic sublattice unlike the ferrimagnets. This fundamental fact leads to a difference in the mechanisms of the magnetization reversal which are discussed in the following subsection. At the same time, ferromagnetic materials are structurally stable compared to ferrimagnetic alloys. Due to the complexity of RE-TM ferrimagnetic alloy fabrication, FM thin films present a more applicable option for the magnetic recording industry.

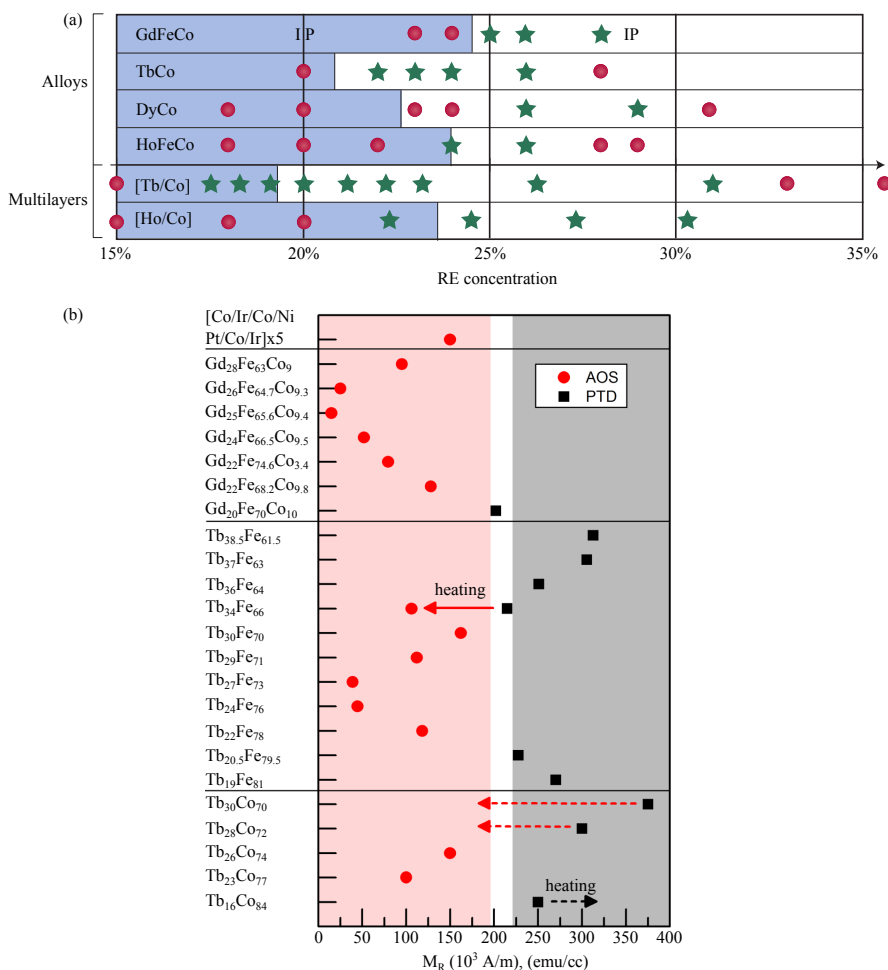


Figure 3.10: An overview of all-optical switching ability of various ferrimagnetic thin films. (a) RE-TM alloys and multilayers as a function of RE concentration. All samples show PMA except two alloys marked IP (for in-plane). Circles denote thermal demagnetization and stars denote HD-AOS. The blue area corresponds to the materials which have compensation temperatures below room temperature [153]. (b) Red dots and light-red area denote AOS whereas black squares and light-grey area denote pure thermal demagnetization (PTD). The abscissa shows remanence magnetization. The arrows depict the thermal treatment in order to make AOS happen [155].

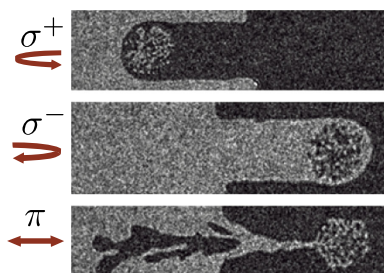


Figure 3.11: Magneto-optical microscopy image of ferromagnetic  $[\text{Co/Pt}]_3$  multilayer after fs laser illumination with circular and linear polarization. AO-HDS is observed for  $\sigma^+$  and  $\sigma^-$  pulses, while  $\pi$  pulses result in randomly formed domains. Figure taken from [49], original image from [34].

All-optical switching in ferromagnetic materials was first demonstrated in 2014 by Lambert *et al.* on  $[\text{Co/Pt}]_N$  multilayers, see Figure 3.11 [34]. Co/Pt multilayers are distinguished materials with superior magneto-optical properties and a strong perpendicular magnetic anisotropy. Besides the  $[\text{Co/Pt}]_N$  multilayers, Lambert *et al.* investigated the AOS ability of CoNi/Pt multilayers and FePtAgC granular media [34]. El Hadri *et al.* demonstrated AOS in Co/Ni [156], while John *et al.* showed FePt granular media are switchable with multiple laser pulses [157].

**Multi-pulse helicity-dependent switching** All-optical switching in any type of pure ferromagnetic layers is mostly demonstrated using a series of circularly polarized pulses [34, 157–161]. Unlike in ferrimagnets, helicity-dependent single-pulse switching in ferromagnets has not been observed, so far. Few publications reported single-pulse-triggered AOS in ferromagnetic films under certain circumstances, up to now [162–164].

**Single pulse switching in FM thin films** In order to deterministically switch the magnetization of ferromagnetic layers using single fs pulses, Gorchon *et al.* used Co/Pt multilayers coupled to GdFeCo ferrimagnetic alloys [162]. According to time-resolved experiments, the reversal of the Co/Pt magnetization takes place within  $\sim 7$  ps, which is slightly longer than in the GdFeCo layer ( $\sim 3$  ps). Later, Laliu *et al.* demonstrated single-pulse switching of Pt/Co/Gd stacks with linearly polarized pulses [163]. These two studies indicate the necessity of ferrimagnetic coupling for the single-pulse switching. In 2017, Vomir *et al.* tuned the laser beam spot to the intrinsic size of magnetic domains, and consequently observed helicity-independent toggle-switching in Pt/Co/Pt stacks [164]. It is also reported that the toggle-switching is completely independent of the light polarization such that circularly polarized pulses contribute toggle-switching as well.

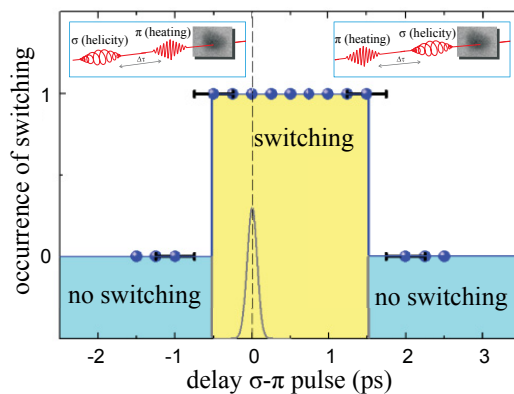


Figure 3.12: All-optical switching ability versus time delay between circularly and linearly polarized pulses. Laser fluences were kept lower than the single pulse switching threshold. Negative delays indicate that the  $\pi$  pulse arrives before the  $\sigma$  pulse, and positive delays vice versa [166].

### 3.3.4 Proposed mechanisms

The studies suggest that the mechanism of AOS in ferrimagnets and ferromagnets is different. In addition, experimental findings point to the different origin for all-optical magnetization reversal for both type of materials. Some of the experimental results support the pure thermal origin of the effect, whereas the others suggest inverse Faraday effect owing to the role of light helicity. As proposed by Vomir *et al.* [164], both explanations may fail under certain circumstances. Therefore, unification of these models is still far from a consensus.

**The inverse Faraday effect** was the earliest model proposed after AOS in ferromagnetic alloys was discovered [133, 165]. The necessity of circularly polarized pulses suggested a symmetry breaking factor which is, in this case, the field generated by IFE. In 2012, Ostler *et al.* [150]<sup>1</sup> reported helicity-independent switching above the laser power threshold at which Vahaplar *et al.* observed helicity-dependency [165]. This ground-breaking observation was explained by the **transient ferromagnetic-like state** approach by Radu *et al.* [151], as discussed above. On the contrary, Alebrand *et al.* showed that neither heating nor helicity alone is sufficient to obtain switching, see Figure 3.12 [166]. It is concluded that all-optical switching is a result of an interplay between helicity and heating for a given laser fluence.

In case of ferromagnetic materials, open questions arise with respect to the strength of the magnetic field. The induced magnetic field strength due to a typical  $\text{mJ}/\text{cm}^2$

<sup>1</sup>Related figures can be found in Supplementary Information (online) of the cited publication

laser fluences is estimated to range from 0.1 - 20 T [149, 167]. One might expect that a magnetic field in this range would be able to switch any magnetic material. On the other hand, studies based on *ab initio* calculations show a good agreement with experimental results. For instance, Cornelissen *et al.* calculated a phase diagram (Figure 3.13) as a function of laser beam fluence and IFE-induced magnetic field lifetime  $\tau$ , which depends on the pulse duration [108]. The simulation suggest a critical lifetime of at least 0.15 ps in order to achieve AOS. As the lifetime increases, AOS is observed at lower laser fluences.

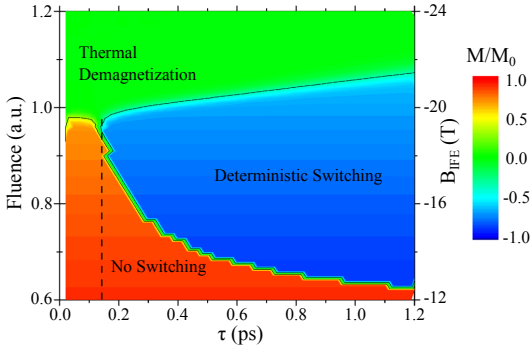


Figure 3.13: Calculated phase diagram of the magnetization state of Co/Pt multilayer as a function of laser fluence and IFE-induced field lifetime  $\tau$  [108].

In 2016, Berritta *et al.* employed *ab initio* theory to predict the effect of IFE on the magnetization switching [168]. The calculations show that there are both spin and orbital contributions to the IFE, and their coefficients are material-specific. Pd and Pt exhibit larger  $K^{IFE}$  (L+S) particularly for photon energies below 1 eV.

**Magnetic circular dichroism (MCD)** is an alternative approach that brings a new understanding to the underlying mechanism of helicity-dependent AOS. Khorsand *et al.* experimentally showed that, in RE-TM ferrimagnetic alloys, HD-AOS occurs in a narrow range of laser fluences,  $F_{LCP} < F < F_{RCP}$ , where  $F_{LCP}$  and  $F_{RCP}$  are threshold values for left and right circularly polarized pulses [169]. Above the  $F_{RCP}$  threshold AOS occurs in helicity-independent manner. Using the experimental data plotted in Figure 3.14, the fluence window ( $\Delta$ ) where AO-HDS occurs can be calculated with the formula below.

$$\Delta = \frac{F_{RCP} - F_{LCP}}{\frac{1}{2}(F_{RCP} + F_{LCP})} \quad (3.9)$$

These findings point to the possible role of MCD in both helicity dependent and independent switching. Recently, Gorchon *et al.* developed a model based on MCD in order to explain multi-pulse switching of ferromagnets, taking FePt-C granular media as an example [159]. In this model, it is assumed that the laser pulse heats the magnetic layer close to the Curie temperature  $T_C$ , where the stability of the magnetic

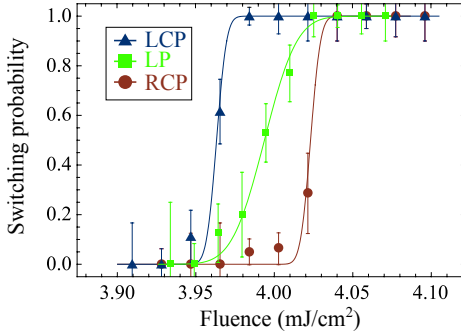


Figure 3.14: Switching probability of GdFeCo alloy film as a function of laser fluence and polarization. Figure taken from [169].

state drops. In case of circularly polarized pulses, the heat absorption for magnetic domains with opposite magnetization directions is different due to MCD. Therefore, the magnetic stability and characteristic hopping time for ‘hot’ and ‘cold’ domains are expected to be asymmetric. The change of the energy barrier is schematically shown in Figure 3.15.

The hopping time  $\tau_{ab}$  between magnetic states is defined with the Arrhenius-Néel law:

$$\tau_{ab}(T) = \tau_0 \exp\left(\frac{E_{ab}(T)}{k_B T}\right) \quad (3.10)$$

where  $\tau_0$  is the characteristic hopping time and  $E_{ab}$  is the energy barrier between states.

Gorchon *et al.* further developed the model by deriving a cumulative probability that agrees with the multi-pulse nature of switching in ferromagnets [159]. The calculations were conducted for 7-nm-thick FePtC granular film with 5.8% MCD asymmetry. As presented in Figure 3.16 (a),  $N=1$  pulse results in random domain formation (AOS probability 0.50) while  $N=10$  pulses are sufficient for a complete AOS (AOS probability 1.00).

The authors also investigated the MCD asymmetry range where AOS can happen as a function of temperature provided by laser pulses ( $N=10$ ). Figure 3.16 (b) shows that as the MCD asymmetry increases, AOS can happen in a broader range of temperatures. The simulations based on these calculations are in good agreement with the experimental study of Lambert *et al.* [34] (see Figure 3.16 (c)).

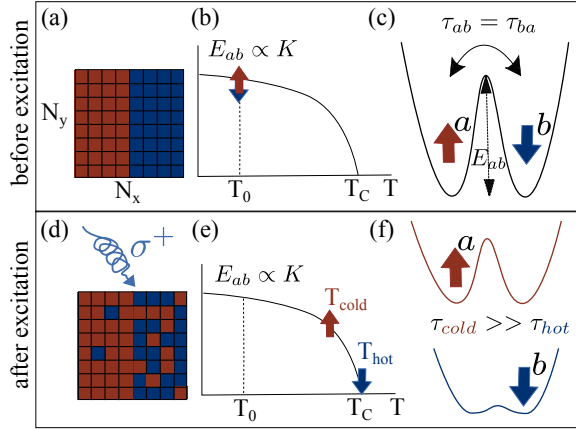


Figure 3.15: The model derived by Gorchon *et al.* based on magnetic circular dichroism effect. (a) Two states of magnetization direction are represented in different colors in a  $N_x \times N_y$  grid. Initially, both magnetic states are at the same temperature  $T_0$  (b) and the energy barrier  $E_{ab}$  between two states makes the hopping rates the same. (d) After circularly polarized pulse excites the system, (e)  $a$  and  $b$  states absorbs different amount of heat and asymmetry arises between the temperatures. (f) The energy barrier at the colder cells is larger than that of hotter cells. Hotter cells are more prone to stochastic switching. Figure adopted from [159].

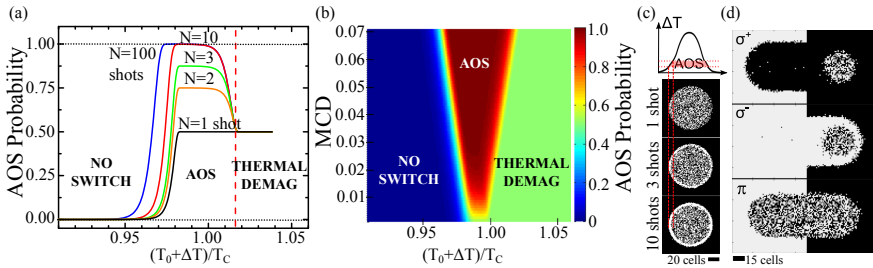


Figure 3.16: Calculations based on the model of Gorchon *et al.* shows the multi-pulse nature of switching and the range of MCD where AOS happens. (a) AOS probability as a function of total temperature rise by different number of laser pulses. For the temperatures close to  $T_C$  AOS probability increases with number of pulses. At higher temperatures, laser illumination ends up with thermal demagnetization independent from pulse number. (b) Calculated MCD effect as a function of temperature provided by  $N=10$  pulses. (c) Simulation of magnetic domain formation after illumination with 1, 3 and 10 pulses of Gaussian intensity profile. (d) Simulation of magnetic domain formation by sweeping the laser beams. All figures taken from [159].



#### **3.3.4.1 Summary**

The mechanism of AOS in ferromagnetic materials has been investigated theoretically [108, 159] and experimentally [160, 170] by a number of groups. The ongoing discussion suggests that, similar to the case of ferrimagnets, AOS is based on a combination of laser-induced heating, magnetic circular dichroism (MCD) [159, 169, 171], and inverse Faraday effects (IFE) [108, 133, 165, 172]. Nevertheless, the questions about the strength of the optically induced IFE magnetic field as well as material and wavelength dependencies are still under debate.

The above-discussed mechanisms lead to a classification of AOS as single-pulse and multi-pulse switching. Ferrimagnetic layers exhibit both types of switching, while ferromagnetic layers require multi-pulses except for special cases. Multi-pulse switching in ferromagnets occurs only in helicity-dependent manner. Single-pulse switching, however, is observed both to occur helicity-dependent and independent.

# Chapter 4

## [Co/Pt]<sub>N</sub> multilayers: Sample fabrication and characterization

This chapter is dedicated to the magnetic properties of [Co/Pt]<sub>N</sub> multilayers as well as their fabrication and characterization processes. The first section explains the unique magnetic and magneto-optical properties of the sample system used in this thesis. The following sections describe the essential instruments employed in fabrication and characterization of the multilayer sample system. A special focus will be put on Taguchi's method that is used to optimize the surface roughness of thin films in a statistical approach. In the last part of the chapter, structural and magnetic characterization results will be discussed.

### 4.1 Magnetic properties of [Co/Pt]<sub>N</sub> multilayers

This section is particularly devoted to the magnetic properties of [Co/Pt]<sub>N</sub> multilayers due to their unique characteristics exploited in this work. Within the three decades after the discovery of perpendicular magnetic anisotropy (PMA) in [Co/Pt]<sub>N</sub> multilayers [69], it has attracted a growing interest due to its potential in applications: exchange bias [173, 174], magneto-optical recording [175, 176], spin valves [177, 178], magnetic tunnel junctions (MTJ) [179, 180], MRAMs [181], generation of magnetic Skyrmions [182], THz emission [183], ultrafast control of magnetism [34, 184] etc. [Co/Pt]<sub>N</sub> multilayers have been used as magneto-optical recording materials due to their adequate perpendicular anisotropy, coercivity and squareness, environmental stability, low deposition temperature and high deposition rate properties [185].

#### 4.1.1 Magneto-optical properties

Magneto-optical properties of [Co/Pt]<sub>N</sub> multilayers are particularly interesting owing to the demand for higher density recording using shorter wavelengths in MO recording technology. Because, reducing the wavelength by a factor of 2 can increase the

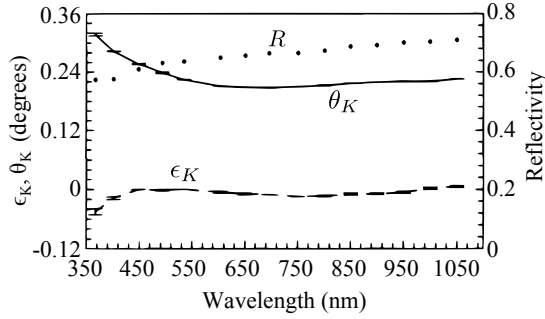


Figure 4.1: Magneto-optical spectra of [Co(0.4 nm)/Pt(1.0 nm)]<sub>21</sub> multilayers between 350-1050 nm wavelengths.  $\theta_K$ ,  $\epsilon_K$  and R stands for Kerr rotation, Kerr ellipticity and reflection, respectively. Data taken from [90].

recording density by a factor of 4 [186]. In [Co/Pt]<sub>N</sub> multilayers, the Kerr rotation is enhanced, and even larger than that of a single thick Co layer [186]. Figure 4.1 shows the experimental data of [Co/Pt]<sub>N</sub> multilayers with individual bilayer thicknesses similar to the ones used in this work. The value of Kerr rotation ( $\theta_K$ ) increases with decreasing wavelengths at the visible range [90, 175, 187]. The enhancement in Kerr rotation has been attributed to exchange polarized Pt [188].

#### 4.1.2 Perpendicular magnetic anisotropy (PMA)

PMA in [Co/Pt]<sub>N</sub> multilayers is formulated by the surface/interface term in the Equation 2.20, as predicted by L. Néel. In order to find the origin of PMA, the effect of spin-orbit interaction, particularly the contribution of orbital magnetic momentum has to be understood. To achieve this goal, the XMCD technique has been widely used due to the ability to distinguish spin and orbital moments. In 1994, Weller *et al.* showed that 3d orbital moments of Co atoms are largely enhanced in Co/Pt and Co/Pd multilayers compared to the metallic Co and other Co based multilayers [189]. It is also shown by Nakajima *et al.* that the 3d-5d hybridization between Co and Pt atoms at the Co/Pt interface gives rise to strong PMA especially in thinner Co layers [190], see Figure 4.2. In addition, the Pt orbital moment induced by the spin polarization also favors PMA. Since the interface plays a crucial role in determining the easy axis, the magnetic properties of [Co/Pt]<sub>N</sub> multilayers are very sensitive to intermixing, alloy formation as well as interfacial roughness [191, 192]. The formation of CoPt alloy phases at the interface was also attributed to the observed anisotropy in Co/Pt multilayers by Garcia *et al.* [69].

In order to have a strong PMA, in general, sharper interfaces are more favorable.

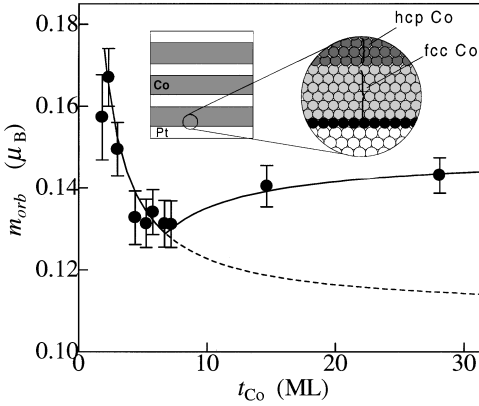


Figure 4.2: Orbital magnetic moment of Co layer determined from XMCD measurements on epitaxial Co/Pt multilayers [190]. The dashed curve denotes an extrapolation for pure Co layer. The gradual increase of orbital moment at thicker Co layers is related to the phase change.

Therefore, the interfacial roughness has to be reduced by engineering the multilayer stack, for instance, by using buffer layers. The buffer layer can also be used for growing a particular crystal orientation to provide a magnetocrystalline anisotropy (MCA) in the perpendicular direction. Tantalum [193, 194] is the mostly used buffer layer to maintain sharp interfaces. Studies on [Co/Pt]<sub>N</sub> multilayers showed an enhancement in PMA when grown on Ta(5 nm)/Cu(10 nm) instead of directly on Cu(10 nm) [194].

Besides the interfacially induced anisotropy, also the crystalline structure of Co and Pt lattice plays a role in PMA. The effect of crystallographic orientation on the anisotropy was studied by Lin *et al.* [195]. In epitaxially grown [Co/Pt]<sub>N</sub> multilayers, a (111) textured Pt seed layer provides the ideal conditions for strong PMA. We note that Co layers in this study are 0.4 nm thin, which is equal to  $\sim 2$  ML, and [Co/Pt]<sub>N</sub> multilayers were not epitaxial, but grown in polycrystalline form.

### 4.1.3 Domains

Magnetic domains of [Co/Pt]<sub>N</sub> multilayers form usually as isolated bubbles or more or less regular stripes depending on the range of Co and Pt thicknesses, and the repetition of bilayers in the stack [196]. The model of periodic stripe domains was proposed by Kittel [197] and developed by Kooz and Enz [89].

The mean domain size decreases as the number of bilayer repetitions increases. The magneto-static energy increase by forming a domain wall is compensated by the gain in demagnetizing energy as the film gets thicker [198]. The predicted domain width  $d$  in the thin film limit ( $t < D_0$ ) is given by the Kaplan model as [199]:

$$d = t \cdot \exp(\pi D_0 / 2t) \quad (4.1)$$

where  $t$  is the thickness of thin film and  $D_0$  is a characteristic domain size. This range is depicted with a dashed red rectangle in Figure 4.3.

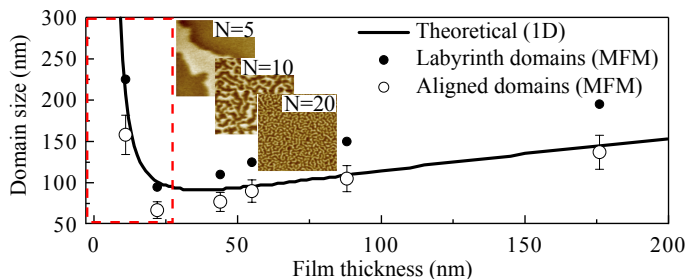


Figure 4.3: Comparison of theoretical and experimental data for domain sizes in [Co(0.4 nm)/Pt(0.7 nm)]<sub>N</sub> multilayers. Dashed red rectangle depicts the thickness range for the samples used in this work. Inset:  $5 \times 5 \mu\text{m}^2$  MFM images of N=5, 10, 20 multilayers after AC demagnetization [200].

#### 4.1.4 Magnetic properties depending on repetition

As mentioned before, relatively thin Co layers ( $< 1.4$  nm [69]) will induce PMA in [Co/Pt]<sub>N</sub> multilayers. Each Co layer is coupled via the non-magnetic Pt layers and all layers form a ferromagnetic block all together [200]. The magnetic anisotropy tends to increase as a function of multilayer repetition [195]. However, after reaching a maximum, the anisotropy energy and orbital magnetic moment contribution decrease for the higher repetitions of the multilayer, allegedly due to the loss of conformal roughness [201]. On the other hand, the roughness gives rise to in-plane demagnetizing fields at the edges of terraces, therefore reducing the shape anisotropy and favoring PMA [202].

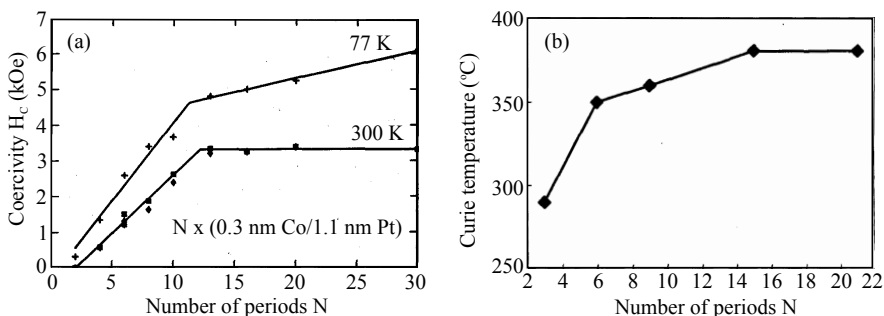


Figure 4.4: Magnetic properties of Co/Pt multilayers depending on number of bilayer periods. (a) Coercivity of [Co(0.3 nm)/Pt(1.1 nm)]<sub>N</sub> multilayers at room temperature and liquid nitrogen (LN) temperature [203]. (b) Curie temperature of [Co(0.3 nm)/Pt(0.8 nm)]<sub>N</sub> multilayers [204].

In a similar way, the coercivity  $H_C$  of the multilayers follows an increasing trend as long as smooth interface structure and homogeneity are preserved. Above a critical thickness,  $H_C$  stays flat (300 K) or increases much more slowly (77 K) with increasing  $N$ , see Figure 4.4(a) [203].

The Curie temperature  $T_C$  of [Co/Pt]<sub>N</sub> multilayers increases rapidly as the number of periods increases for smaller  $N$  values, such that a 70°C increment is observed between  $N=3$  and  $N=9$  [204]. Beyond this point, only a small increase in  $T_C$ , 20°C, observed as multilayer repetition reaches  $N=21$ , see Figure 4.4(b).

## 4.2 Thin film fabrication and characterization instruments

A magnetron sputtering deposition system was primarily used in this work to fabricate [Co/Pt]<sub>N</sub> multilayer thin films. Atomic force microscopy (AFM) and x-ray reflectivity (XRR) methods were used for structural analysis of the single layers as well as the multilayer stacks. The magnetic characterization of *as-deposited* samples was done using magnetic force microscopy (MFM) and static magneto-optical Kerr effect (MOKE) magnetometry.

### 4.2.1 Magnetron sputtering

Magnetron sputtering is one of the widely used physical vapor deposition (PVD) techniques, particularly in fabrication of magnetic thin films for magnetic recording and HDD industry [8,205], and it is capable to deposit high-quality, uniform thin films under vacuum conditions.

Sputtering takes place due to a linear momentum transfer from the accelerated positive argon ions ( $Ar^+$ ) to the solid target material. In the DC sputtering technique, high-purity argon gas is introduced to the chamber and is ionized by means of the strong applied electric fields as well as the gas-electron collisions. The accelerated positive ions bombard the negatively charged target material. If the kinetic energy of  $Ar^+$  ions is sufficient, clusters of atoms are sputtered from the target material towards the grounded substrate. In magnetron sputtering, a permanent magnet array is placed behind the target in order to achieve higher ionization rates by trapping the charged particles in a ring-formed area in the vicinity. Magnetic target materials require stronger permanent magnet configurations to suppress their own magnetic fields. Besides of DC sputtering, radio frequency (RF) sputtering guns can be used, where a radio frequency (13.56 MHz) electric field is applied to the target. The magnetron sputtering process is schematically shown in Figure 4.5(a).

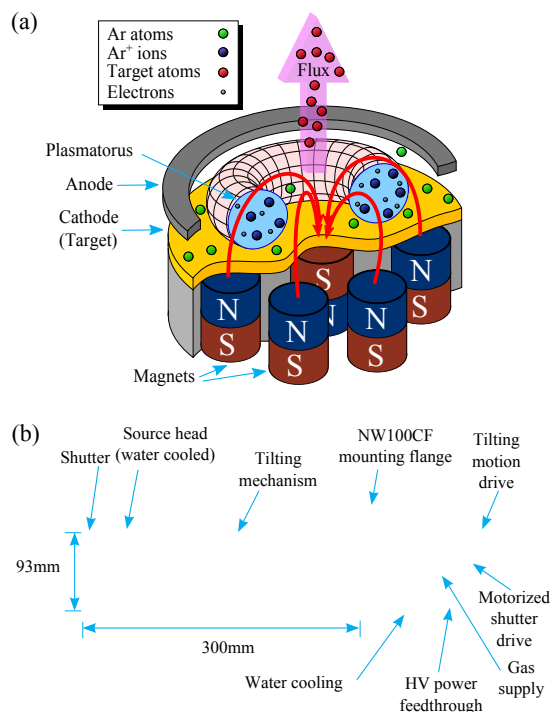


Figure 4.5: (a) Schematics of magnetron sputtering mechanism. Argon ions and electrons are trapped by the magnetic field (field lines are depicted by red arrows) and generate a plasmatorus which results in an efficient ionization rate. High voltage is applied between anode ring and target (cathode) to accelerate argon ions towards the target material. Sputtered target atoms are directed to the substrate holder. (b) Components of magnetron sputtering gun used in sample fabrication. The gun is used in *sputter-up* geometry.

In this study, we employed a magnetron sputtering chamber located in the Nanocluster at the Helmholtz Nanoelectronic Facility (HNF). The chamber is equipped with 4 RF and 4 DC sputter guns (Mantis Deposition Systems, see Figure 4.5(a)), quartz crystal microbalance (QCM) as well as a motorized manipulator with linear (z-shift) and rotational motion drivers. Manipulator can rotate the sample holder up to 80 RPM for uniform depositions. Moreover, any surface treatment is possible by means of heater and RF bias voltage. The main components of EpiCentre manipulator is shown in Figure 4.6. The chamber is pumped by a turbo molecular pump and an ion getter pump down to mid  $5 \times 10^{-11}$  mbar pressures. Depositions typically take place at an Ar pressure of low  $10^{-3}$  mbar.

During the deposition of the multilayer stacks, the pneumatic shutters of the manip-

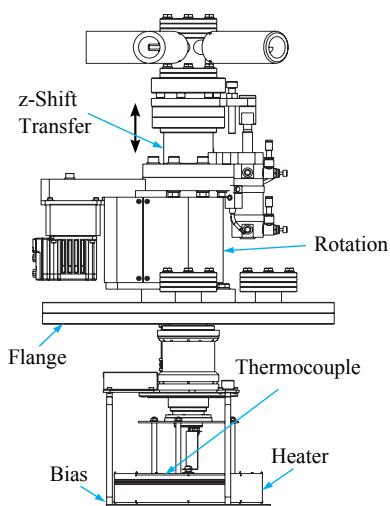


Figure 4.6: Schematics of the manipulator used in thin film fabrication processes. The rotatable sample holder is located at the bottom of the manipulator. During the deposition, sample holder can be rotated and heated. Bias can be applied in order to clean the substrate by sputtering.

ulator and sputter guns are controlled by a software. Precise shutter timing plays a critical role in controlling the thickness of depositions which typically takes only seconds.

#### Quartz crystal microbalance

The thickness of the deposition was indirectly monitored using a quartz crystal microbalance (QCM) located in the vicinity of the substrate holder. The material flux from the targets deposits on the crystal surface as well as the substrate surface. The additional mass per unit area is calculated by measuring the change in frequency of the quartz crystal resonator. The QCM can be calibrated via *ex-situ* thickness measurements by XRR and it is as precise as 0.1 Å/sec.

#### 4.2.2 Atomic/Magnetic force microscopy

In atomic force microscopy, a nano-scale sharp tip on a cantilever (see Figure 4.7) is engaged and scanned over the surface with a feedback mechanism that maintains a constant force or a constant distance between the tip and the sample surface. The cantilever is driven either in DC (contact) mode or in AC (non-contact) mode. The feedback mechanism uses a laser source impinging on the back surface of the cantilever such that the reflected laser beam is captured by an optical detection system and enables to map out the surface topography. The surface image is formed by rastering a defined area usually on micrometer length-scales.

In this study, we employed a Cyber S AFM device from Asylum Research. The



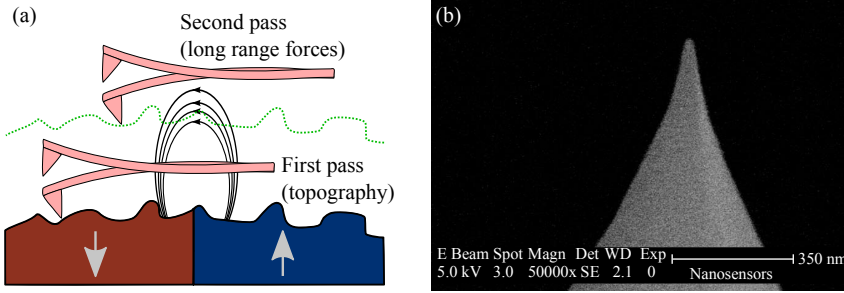


Figure 4.7: (a) Schematic picture of the two-pass scan motion of a magnetic AFM tip in AC mode. The first pass monitors the surface topography. Then, the tip is lifted by a constant amount from the surface (dotted line). In the second step the tip only detects the long-range magnetic forces. (b) A micrograph of the magnetic tip used in this thesis. Image taken from [206].

software of the system allows one to control the scanning of the tip such that the first pass is followed by a second one in which the tip is lifted above ( $\Delta h$ ) the sample surface. This mode of operation is called as *nap mode* and can be used to subtract the surface topography from any other force sensed by the raised tip depending on its physical properties. For instance, a typical AFM tip can be coated with a magnetic layer to be used for magnetic force microscopy (MFM). Slight thickening of the tip may result in lower lateral resolution, but the tip can be used to detect magnetic stray fields that typically reach up to a few tens of nm above the surface. By subtracting the surface topography, an image of magnetic domains can be obtained.

In the AC-mode, a better signal-to-noise ratio can be obtained by measuring the dynamic properties of the vibrating cantilever, namely, phase and frequency modulation. Then, the signal depends on the force derivative,  $\Delta\Phi \sim (-Q/k)\frac{\partial F}{\partial z}$ , where  $Q$  and  $k$  are the quality factor and spring constant of the cantilever, respectively.

The magnetic tips used in this thesis are provided from Nanosensors and have different magnetic properties. Company descriptions PPP-MFMR, PPP-LM-MFMR and PPP-LC-MFMR stand for standard, low momentum and low coercivity tip, respectively.

### 4.2.3 X-ray reflectivity

X-ray reflectivity (XRR) technique uses x-ray diffraction at lower incidence angles ( $\theta < 3^\circ$ ) that gives rise to total external reflection of the x-rays from the interfaces of thin films. The intensity of the reflected x-ray beam gives insight into the density, thickness and roughness of mono- or poly-crystalline thin film structures. Therefore, XRR is considered to be a non-destructive tool with a precision of the order of the

x-ray wavelength.

The reflectivity signal is recorded in  $\omega/2\theta$  geometry, where  $\omega$  is the true incident angle, which is fixed according to the reflection surface. All XRR measurements presented in this thesis were made on the five-axes goniometer of a Phillips X'Pert MRD diffractometer using Cu  $K_\alpha$  radiation. A typical reflectivity signal first shows a drop of intensity at an angle determined by the electron density of the thin film. As the incidence angle increases, a series of Kiessig fringes is observed. These fringes allow one to calculate the thickness of the thin film layer using the equation below.

$$d = \frac{\lambda}{2} \frac{1}{\theta_{m+1} - \theta_m} \quad (4.2)$$

The distance between the fringes is inversely proportional to the layer thickness. The surface or interface roughness is a factor that reduces the amplitude of the fringes. Unlike the single layers, it is difficult to calculate the thicknesses of multilayer stacks. Therefore, we used the X'Pert Reflectivity software package to simulate the XRR signal and obtain the structure from the fitting parameters.

#### 4.2.4 Magneto-optical Kerr effect magnetometry

MOKE magnetometry is a quick and efficient method for characterization of magnetic thin films with reflective surfaces. The fundamental aspects of the magneto-optical Kerr effect was extensively discussed earlier. This subsection is dedicated to the layout of the experimental setup (see [Figure 4.8](#)).

In our experiments, MOKE magnetometry was used in the polar geometry in order to confirm the perpendicular magnetic anisotropy of  $[\text{Co/Pt}]_N$  multilayers. Despite the fact that no quantitative magnetization information is obtained, one can qualitatively measure the magnetization as a function of the external magnetic field. The coercive fields ( $H_C$ ) of multilayers with different bilayer repetition rate  $N$  and varying temperature  $T$  were compared in this study.

A cw diode laser producing a collimated light at a wavelength of 470 nm was employed as a light source. The laser beam was polarized using a Glan-Thompson prism and was directed towards the sample through the electro-magnets, which have a bore in order to access the sample surface. The reflected laser beam was modulated by an optical chopper at 620 Hz frequency. In order to detect the Kerr rotation, we employed a set of a half-wave plate and a Wollaston prism. The  $\lambda/2$  plate before the Wollaston prism rotates the polarization such that s- and p-polarized components of the beam are split into equal intensities. Each component was measured by a balanced photodiode (PD)

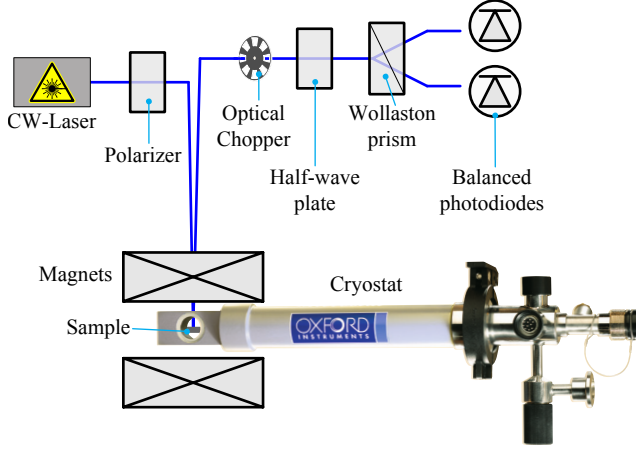


Figure 4.8: The layout of static magneto-optical Kerr magnetometry setup in polar geometry. Linearly polarized cw laser beam was used as a light source. A pair of half-wave plate and Wollaston prism was used to split s- and p-polarized components to be measured by the balanced photodiodes. The optical chopper modulated the laser beam and was used as reference signal for the lock-in amplifiers during detection.

and recorded using lock-in amplifiers as a function of the external magnetic field. The photodiode amplifiers allowed us to acquire the output signals as difference and sum of PD1 and PD2. Therefore, the magnetic signal was separated from other optical contributions.

Low temperature measurements were carried out by cooling the sample using a Helium cryostat with optical access (Oxford Instruments). Details about the cryostat can be found in [Appendix B](#).

### Detection of the Kerr rotation

Prior to the MOKE measurement, the intensities  $I_1$  and  $I_2$  from PD1 and PD2 were equalized so that the difference signal  $\Delta I \approx 0$ . As the magnetic field is swept from positive to negative maximum, the ellipticity and polarization angle of reflected light result in a sizable  $\Delta I$ .

In order to describe the polarization state of the light upon reflection from a magnetic surface, Jones matrices are employed [120].

$$\mathbf{J}_{ref} = \underbrace{\begin{pmatrix} r_{ss} & r_{sp} \\ r_{ps} & r_{pp} \end{pmatrix}}_{\text{sample}} \cdot \underbrace{\begin{pmatrix} 1 & 0 \\ 0 & 0 \end{pmatrix}}_{\text{polarizer}} \cdot \underbrace{\begin{pmatrix} E_p \\ E_s \end{pmatrix}}_{\text{light}} = E_p \begin{pmatrix} r_{ss} \\ r_{ps} \end{pmatrix} \quad (4.3)$$

where  $E_p$  and  $E_s$  are the electric field components parallel and perpendicular to the plane of incidence, and  $r_{ij}$  are Fresnel reflection coefficients.

After reflection, the laser beam is split into two orthogonally polarized beams by the Wollaston prism and analyzed by balanced photodiodes. The Jones vectors of two beams recorded by the photodiodes PD1 and PD2 are represented as follows:

$$\mathbf{J}_{PD1} = \begin{pmatrix} 1 & 0 \\ 0 & 0 \end{pmatrix} \cdot \begin{pmatrix} \cos \varphi & \sin \varphi \\ -\sin \varphi & \cos \varphi \end{pmatrix} \cdot \begin{pmatrix} r_{ss} \\ r_{ps} \end{pmatrix} \cdot E_p = \begin{pmatrix} r_{ss} \cos \varphi + r_{ps} \sin \varphi \\ 0 \end{pmatrix} \cdot E_p \quad (4.4)$$

and

$$\mathbf{J}_{PD2} = \begin{pmatrix} 0 & 0 \\ 0 & 1 \end{pmatrix} \cdot \begin{pmatrix} \cos \varphi & \sin \varphi \\ -\sin \varphi & \cos \varphi \end{pmatrix} \cdot \begin{pmatrix} r_{ss} \\ r_{ps} \end{pmatrix} \cdot E_p = \begin{pmatrix} 0 \\ -r_{ss} \sin \varphi + r_{ps} \cos \varphi \end{pmatrix} \cdot E_p \quad (4.5)$$

The normalized differential signal is then expressed in terms of the Fresnel reflection coefficients [207].

$$\frac{I_1 - I_2}{I_1 + I_2} = \frac{\mathbf{J}_{PD1} \mathbf{J}_{PD1}^* - \mathbf{J}_{PD2} \mathbf{J}_{PD2}^*}{\mathbf{J}_{PD1} \mathbf{J}_{PD1}^* + \mathbf{J}_{PD2} \mathbf{J}_{PD2}^*} \propto 2\theta_K \propto \frac{r_{ps}}{r_{ss}} \quad (4.6)$$

In the polar MOKE case, s and p polarizations are indistinguishable, thus the form of the Jones matrix is invariant with respect to the incident beam.

### 4.3 Taguchi's method for roughness minimization

The deposition of sub-nm thickness layers requires the optimization of growth parameters and a precise calibration of the instruments. Preliminary depositions were done in order to optimize the interface smoothness using Taguchi's optimization method [208]. The roughness of each layer was measured using AFM and the results were used in the statistical approach for finding the optimum growth conditions. XRR was employed to measure the actual film thickness as well as to calibrate the growth rates.

Taguchi's method is a statistical approach used in the design of experiments (DOE) to calculate the effect of each parameter on any measurable experimental output - the surface roughness in this study. Investigating the effect of the sputtering parameters such as temperature, pressure, sputtering power and sample-target distance within three different control levels for each would normally require  $3^4$  experiments [209,210]. However, with the help of statistical calculations this number can be reduced to 9. Taguchi's method employs the signal to noise ratio (SNR) as a performance statistic value for optimization. When the smaller experimental output value is required

(smaller-the-better) SNR is calculated using the equation:

$$SNR = -10 \log C_i \quad (4.7)$$

where  $C_i$  refers to the average of the squares of each roughness measurement for sample number  $i$ . The next step is to calculate the impact of a particular parameter level using the average of the SNR values which involves only that particular level.

$$X_i = m_{X_i} - m \quad (4.8)$$

In the formula above,  $m$  represents the average of the SNR values for all 9 experiments. The optimum level for any parameter is the one which gives the maximum SNR, since the  $\{-\log\}$  function is a monotonic decreasing function. A concise information about this optimization method can be found in Ref. [211].

### 4.3.1 Roughness minimization

The roughness minimization study was carried out prior to the multilayer deposition aiming a smoother film growth. Platinum was chosen as a test material since it is the most inert one among the materials to be grown. Therefore, it allows us to perform *ex-situ* surface characterization measurements without oxidation. Three process levels were determined for the corresponding sputtering parameters as shown in Table 4.1. Nine Pt layers, in total, were grown on different Si(001) wafers and the AFM study was performed for each sample following the deposition. The surface roughness was measured at three different positions on each surface to acquire more statistics for the calculation.

Table 4.1: Sputtering process parameters and their levels.

Symbol	Process parameter	Level 1	Level 2	Level 3
A	Temperature	RT	400°C	600°C
B	Pressure	Low	Mid	High
C	Power	43 W	60 W	80 W
D	Distance	80 mm	100 mm	120 mm

Among those experiments, two topography images are shown in Figure 4.9 in order to compare the effect of the parameters. Platinum layers in experiments Nr.3 and Nr.7 (see Table 4.2 for details) were grown using the same sputtering power, but in different combinations of temperature and pressure. It is clear from the comparison that the grain sizes of Platinum grown on the hotter substrate are much larger than in the case of the colder substrates. This can be attributed to the recrystallization of

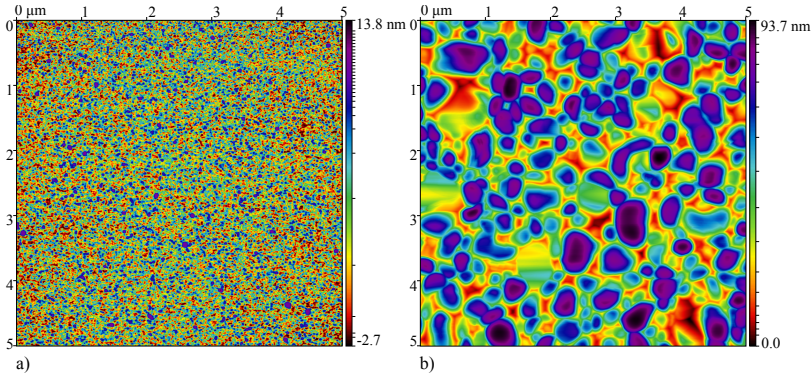


Figure 4.9: Surface topographies of Pt layers measured by AFM in  $5 \times 5 \mu\text{m}^2$  area. Layers were grown at a) low temperature - high pressure (Exp. Nr.3) and b) high temperature - low pressure (Exp. Nr.7). The same sputtering power was used for both layers.

the grains at elevated temperatures. Recrystallization also apparently resulted in a large surface roughness.

Surface roughness measurements (RMS) and calculated  $C_i$  and SNR values are given in Table 4.2. Based on these data, one can calculate the effect of each factor on the surface roughness. A complete picture of the deposition parameters and their levels is given in Figure 4.10

Table 4.2:  $L_9$  ( $3^4$ ) orthogonal array and experimental results of the surface roughness measured by AFM. Control factors A, B, C and D stand for temperature, pressure, power and distance, respectively.

Number of experiment	Control factors				Roughness (nm)			$C_i$	SNR (dB)
	A	B	C	D	1 <sup>st</sup>	2 <sup>nd</sup>	3 <sup>rd</sup>		
1	A1	B1	C1	D1	0.69	0.72	0.72	0.50	2.973
2	A1	B2	C2	D2	1.00	1.03	1.06	1.06	-0.259
3	A1	B3	C3	D3	1.24	1.23	1.21	1.50	-1.774
4	A2	B1	C2	D3	4.70	4.81	4.80	22.75	-13.571
5	A2	B2	C3	D1	5.56	5.64	5.50	30.99	-14.912
6	A2	B3	C1	D2	4.49	4.52	4.46	20.16	-13.045
7	A3	B1	C3	D2	4.23	4.60	4.43	19.56	-12.914
8	A3	B2	C1	D3	7.82	8.02	7.98	63.05	-17.997
9	A3	B3	C2	D1	5.54	5.41	5.44	29.85	-14.750

In this section, four deposition parameters and three levels per each were statistically analyzed in order to minimize the surface roughness of the Platinum layer. The analysis indicated that low temperature (A1), low pressure (B1) and low sputtering

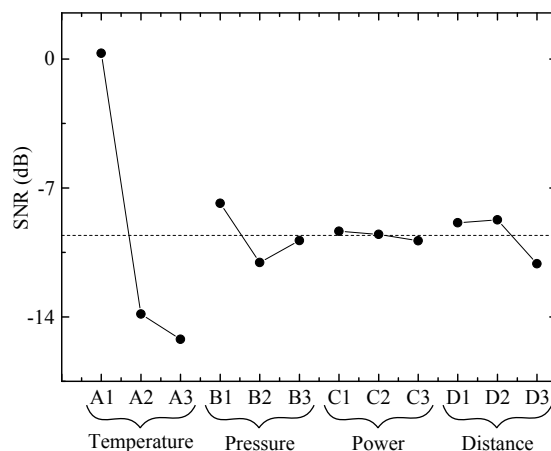


Figure 4.10: Results of the Taguchi's method for sputtering parameters.

power (C1) resulted in the lowest surface roughness. The sample-target distance was optimum at 10 cm (D2) according to the analysis. However, the diverging material flux could have caused an inhomogeneous film growth. Therefore, the sample-target distance was set to 8 cm. The above described optimization process was not repeated for the other materials used in the multilayer system, but the same trend is followed in the growth. Here, it has to be noted that the target materials erode as a consequence of long sputtering time. Thus, the pressure or the power might be insufficient to ignite the plasma. Due to the change of the parameters, one would expect some minor changes in the thin film structure [212].

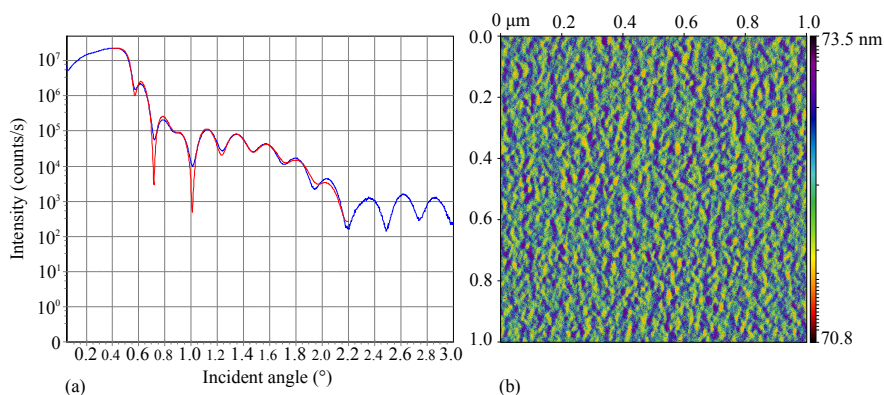


Figure 4.11: Structural characterization of the Tantalum buffer layer. (a) XRR measurements (blue) and the fitting curve (red). The fitting curve is between  $0.4$  and  $2.2^\circ$ . (b) AFM measurements over  $1 \times 1 \mu\text{m}^2$  sampling area.

The above analysis shows that the Platinum layers on SiO<sub>2</sub> have sub-nm roughness under optimum conditions. Nevertheless, a smoother buffer layer is needed to grow Co/Pt multilayers with well-defined interfaces. As tantalum buffer layers are widely used for growing such smooth interfaces, we chose tantalum as well.

A Ta (20 nm) layer was deposited on SiO<sub>2</sub> substrate and its structural analysis was done using XRR and AFM techniques. Figure 4.11(a) shows the measured XRR signal and its fitting curve. A simulation of the XRR data first confirmed that the Ta layer is oxidized and formed a Ta<sub>2</sub>O<sub>5</sub> (~ 3 nm) layer. SiO<sub>2</sub>/Ta and Ta/Ta<sub>2</sub>O<sub>5</sub> interfaces have a roughness of 0.48 and 0.44 nm, respectively. In order to verify the surface roughness, the AFM measurement was performed on the same sample. An analysis of the AFM data shown in Figure 4.11(b) results in 0.14 nm (RMS) roughness.

#### 4.4 [Co/Pt]<sub>N</sub> multilayer fabrication

[Co(0.4 nm)/Pt(0.7 nm)]<sub>N</sub> multilayers were grown on top of oxidized Si(001) wafers by magnetron sputtering at room temperature. The silicon wafers were cut in 10 × 10 mm<sup>2</sup> dimensions and cleaned in iso-propanol bath before introducing into the UHV chamber. The wafers were baked out in the load-lock chamber at 100°C to remove any water contamination. Uniform layer growth is ensured by rotating the sample holder at 10 RPM. The deposition rate for each material was monitored by quartz crystal microbalance that was calibrated by the x-ray reflectivity method. A buffer layer of Ta (5 nm) was deposited prior to the multilayer growth in order to achieve a good interface smoothness. After the [Co/Pt]<sub>N</sub> deposition, a Pt capping layer (1-2 nm) was deposited on top of the multilayer to prevent surface oxidation. Element selective microscopy has proven that even 1 nm of Pt layer fully covers the top surface. A brief overview of the sputtering parameters is given in the Table 4.3.

Table 4.3: Sputtering parameters used in growth of [Co(0.4 nm)/Pt(0.7 nm)]<sub>N</sub> multilayer system.

Material	Gun type	Power	Pressure	Rate
Ta	RF	60 W	2.9 E-3 mbar	0.1 Å/sec
Co	RF	50 W	2.9 E-3 mbar	0.1 Å/sec
Pt	DC	26 W	2.9 E-3 mbar	0.3 Å/sec

Figure 4.12 shows the general layout of ferromagnetic [Co/Pt]<sub>N</sub> multilayer system used in this thesis.



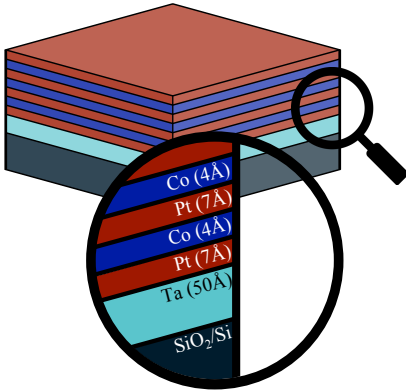


Figure 4.12: A layout of [Co/Pt]<sub>N</sub> multilayer system used in this thesis. The multilayer stack was grown on native oxide silicon substrates. A tantalum layer was used to maintain a smooth interface.

## 4.5 Analysis and results

### 4.5.1 Structural analysis

After fabrication of the [Co/Pt]<sub>N</sub> multilayers with  $N = 1, 3, 5, 7$  and  $9$ , an XRR study was performed on these multilayer stacks in order to confirm the thicknesses. The XRR measurements of all multilayers are shown in Figure 4.13. In this waterfall graph, one can qualitatively see that the distances between fringes are getting shorter with the increasing bilayer repetition. We also show the measured thickness values and their deviations from the nominal thickness values as inset. The largest experimental error here is 7.4% and indicates that the depositions are highly consistent as desired. We note that, a precise simulation of thickness, roughness and density parameters of individual layers is extremely difficult especially when each layer has a thickness comparable to the x-ray wavelength.

In Figure 4.14, an XRR simulation of the [Co/Pt]<sub>3</sub> sample is given. The fitting results show that the error for the thickness of the ultrathin films can reach up to 57%. However, this error bar corresponds to only a few Ångströms of thickness. The large error is attributed to the precision of both experiment and fitting procedure. The XRR fitting method gives better precision in the case of thicker films, which was used for calibration of growth rate in this study.

For further structural analysis of [Co/Pt]<sub>N</sub> multilayers, we performed AFM studies (data shown below together with MFM data). It was already known that Ta and Pt layer grow in polycrystalline form. By this measurement, the polycrystalline growth of [Co/Pt] is also confirmed.

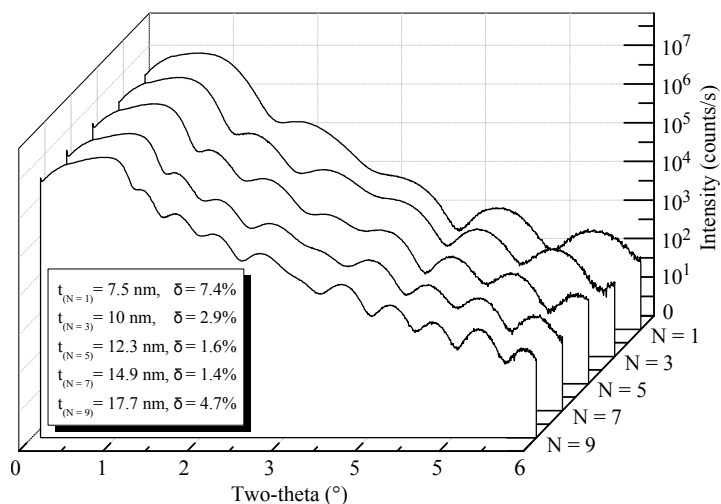


Figure 4.13: XRR measurements of multilayers for  $N = 1, 3, 5, 7$  and  $9$ . The total thicknesses of the multilayer stacks are extracted from fitting the data. Measured total thicknesses and their deviations from the nominal thicknesses are given as inset.

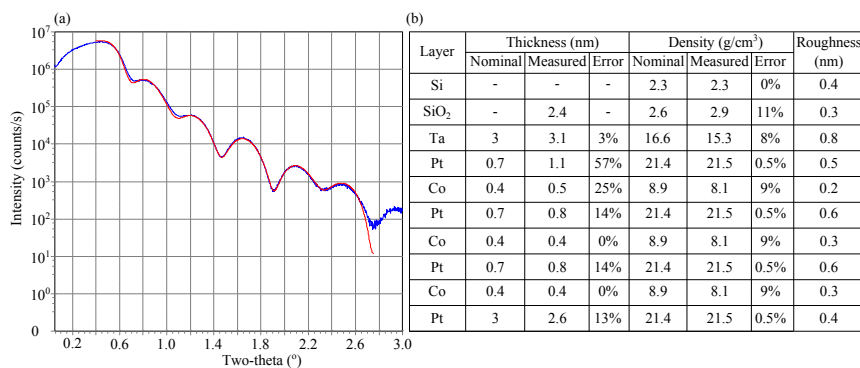


Figure 4.14: XRR simulation to the data taken from  $[\text{Co/Pt}]_3$  multilayer. (a) XRR data (blue) and simulation (red) curves. (b) Comparison of nominal and measured values.

## 4.5.2 Static magnetic characterization

### Polar MOKE

The static magnetic characterization of the multilayers was performed in two different experimental techniques. MOKE magnetometry and MFM were employed in order to measure hysteresis loops and to obtain magnetic domain maps, respectively. Here, in Figure 4.15(a), we show magnetic hysteresis loops of a  $[\text{Co/Pt}]_3$  multilayer at varying

temperatures from 50 K to 300 K. The squareness of the loops indicates PMA with 100% remanent magnetization at all temperatures. In addition, we extracted coercive field ( $H_C$ ) values from the curves and plotted them in Figure 4.15(b) as a function of temperature T for N=3 as well as the bilayer repetition number N for T=300 K.

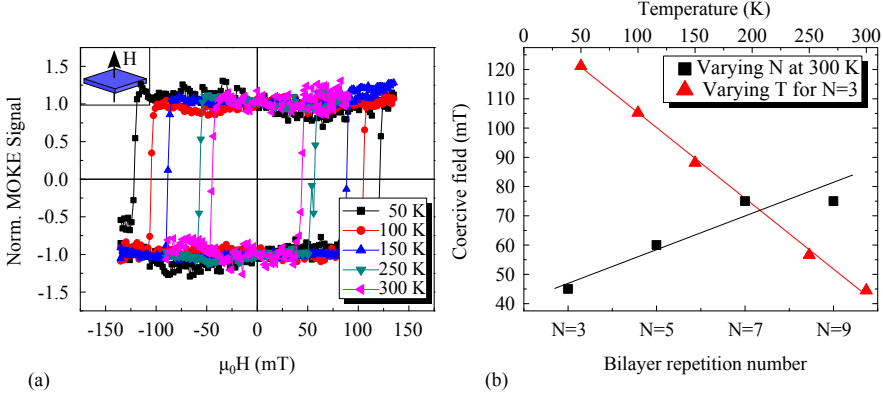


Figure 4.15: Static magnetic characterization as a function of temperature and multilayer repetition. (a) Magnetic hysteresis curves of  $[\text{Co/Pt}]_3$  sample at temperatures between 50 K and 300 K show PMA and 100% at all temperatures. (b) Coercive fields of multilayers with varying  $N$  measured at 300 K (black squares and lower abscissa) and for  $[\text{Co/Pt}]_3$  measured at varying  $T$  (red triangles and upper abscissa). The full lines are guides for the eye.

The sharp magnetization reversal and full remanence (squareness) of sputtered  $[\text{Co/Pt}]_N$  multilayers have been attributed to the domain wall pinning rather than the domain nucleation [95].

## MFM

The first MFM measurements of an *as-deposited*  $[\text{Co/Pt}]_3$  multilayer were performed using a magnetized tip with large magnetic moments (PPP-MFMR, Nanosensors<sup>TM</sup>). After the first scan, as shown in Figure 4.16(a), a single domain structure was observed in a  $10 \times 10 \mu\text{m}^2$  area, in contrary to the expectations to observe ground state domains. Then, a larger area ( $25 \times 25 \mu\text{m}^2$ ) was measured using the same scan rate and number of lines per scan, which means that the tip moved faster within the given area. Consequently, a magnetic domain pattern was observed around the  $10 \times 10 \mu\text{m}^2$  square that is magnetically reversed by this particular tip. Further scans on the same area proceeded the magnetization reversal. The evolution of the domain pattern is shown in Figure 4.16(b), (c) and (d).

Tip-induced magnetization reversal is an evidence that using a low magnetic moment

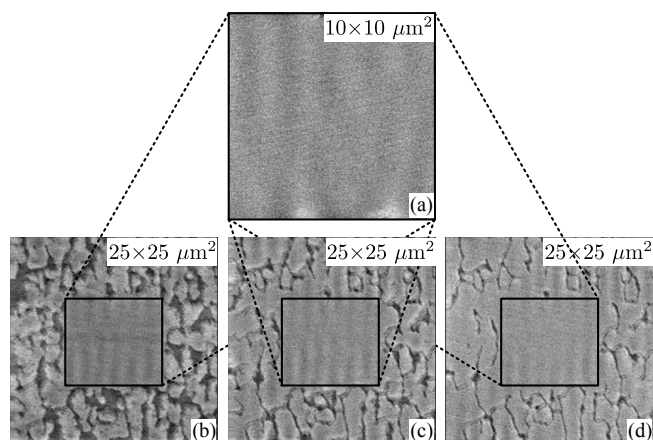


Figure 4.16: Magnetic force microscopy images of an *as-deposited* [Co/Pt]<sub>3</sub> multilayer using a magnetized tip with large magnetic moments. First scan within  $10 \times 10 \mu\text{m}^2$  area switched the magnetization completely (a). Further scans were made on a larger area, but with a faster tip velocity (b), (c) and (d). The visible domain structure vanishes slowly as the tip scans repeatedly.

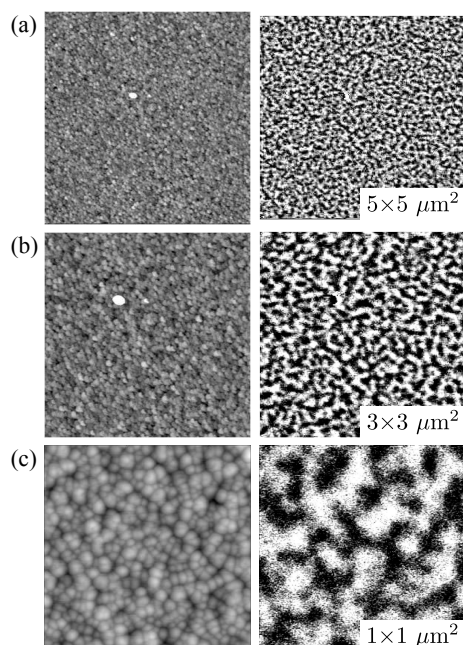


Figure 4.17: Topography (left) and magnetic (right) images of [Co/Pt]<sub>5</sub> multilayer with different magnification. Magnetic domain images of *as-deposited* samples confirms labyrinth-like domains of  $\sim 100$  nm width.

MFM tip is a necessity in order to observe the magnetic structure of the surface without modification. For this reason, PPP-LM-MFMR tips provided from Nanosensors<sup>TM</sup> were employed. Repetitive measurements on the same area on the surface confirmed that magnetic domains are persistent against tip-induced field. In Figure 4.17, the surface topography (left) and magnetic domain (right) images of [Co/Pt]<sub>5</sub> multilayer are shown for the same area, but at different scales. The magnetic domains take a labyrinth-like shape with  $\sim 100$  nm width.

### XMCD

A preliminary XMCD measurement was performed on the Co L-edge in order to confirm the use of the samples for the further XMCD-PEEM imaging experiments. In this measurement, the magnetic field strength was altered between +5 and -5 T with a constant x-ray beam polarization<sup>1</sup>.

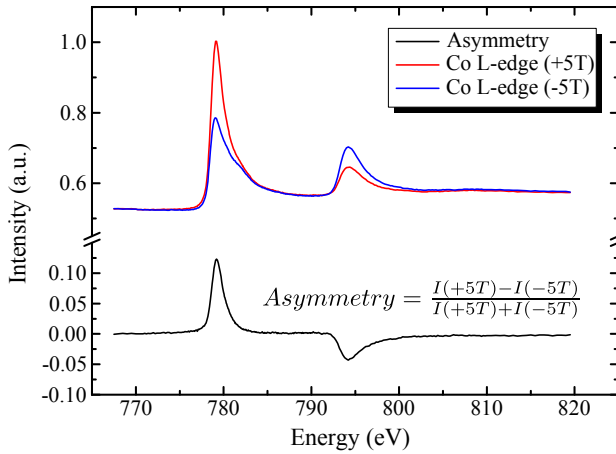


Figure 4.18: Normalized XMCD signal at Co L-edge obtained by alternating magnetic field direction.

The spectrum given in Figure 4.18 shows the data from two magnetic states and the calculated asymmetry. The asymmetry at the L<sub>3</sub>-edge is around 10%. The spectrum also indicates no measurable oxidation of the Co layer.

Our attempt to obtain XMCD signal from Pt layers also aimed at elucidating the possible role of Pt magnetic moments in the AOS phenomenon. XMCD spectra were earlier obtained from the Pt L-edges [57] and N-edges [213]. Recently, Willems *et*

<sup>1</sup>We acknowledge Dr. M. Imtiaz Khan and Dr. Stefan Cramm from FZ Jülich Beamline at BESSY-II storage ring for obtaining XMCD data.

*al.* measured Pt O<sub>2,3</sub> and N<sub>6,7</sub> edges using a free-electron laser facility and imaged domain patterns of both Pt and Co layers [214]. This study revealed an inverted domain contrast due to the opposite sign of the MCD effect at the Co M-edge and Pt N-edge. However, it is known from time-resolved XMCD experiments in the XUV range that the Co/Pt interface follows the magnetization of the Co layer [215]. In this study, we were able to reach the energy of the N<sub>1,2,3</sub>-edges. Nevertheless, the signal level was very low and *possible* imaging of magnetic domain pattern at the Co/Pt was not possible.



# Chapter 5

## Experimental techniques

According to the literature, all-optical switching of the magnetization in thin films follows a full demagnetization, i.e., a complete quenching of the magnetization. However, magnetization reversal happens only if the optimum sample and laser beam conditions are fulfilled. In order to be able to fully demagnetize a thin film sample such as Ni, GdFeCo or Co/Pt, the pump laser fluence must be of the order of  $\text{mJ}/\text{cm}^2$  [32], as described in Chapter 3. Such a pump fluence with femtosecond temporal duration can be achieved by using a laser amplifier system. In this section, the components of the laser amplifier system will be described.

One of our main goals is to image the resulting magnetic domain structures following the laser illumination. To achieve this goal we built a magneto-optical Kerr microscope, which is coupled to the laser system. This setup allowed *in-situ* imaging of the magnetic domains. In order to enhance the lateral resolution, we also employed a photoemission electron microscopy (PEEM). The added benefit of the latter technique is element selectivity and a detailed image of the domain structure.

### 5.1 Description of the femtosecond laser system

The femtosecond laser system used in the experiments is provided from *Spectra Physics GmbH* and consists of the following units:

- *Millennia*, a continuous wave solid state laser ( $\text{Nd}:\text{YVO}_4$ ), is pumping the seed laser with 4.3 W pump power at a wavelength of 532 nm
- *Tsunami*, as a seed laser ( $\text{Ti}:\text{Sapphire}$ ), is capable of generating a series of femtosecond pulses at 80 MHz repetition rate with a central wavelength of  $\lambda_r \approx 800$  nm
- *Empower* is a Q-switched,  $\text{Nd}:\text{YLF}$  laser and is pumping the gain medium of the amplifier



- *Spitfire Pro*, pulsed regenerative amplifier (Ti:Sapphire), is used for energy amplification of the nJ pulses from *Tsunami* by six orders of magnitude ( $\times 10^6$ )

This system, see Figure 5.1, can generate  $\leq 70$  fs laser pulses of  $\sim 1$  mJ pulse energy at 1 kHz repetition rate and can reach a peak power of  $\sim 10^{10}$  W. The control software of the system allows adjustment of the Pockels cells timing in the cavity and tuning of the repetition rate from 1 kHz down to 20 Hz, with an additional option of manual trigger to generate single pulses.

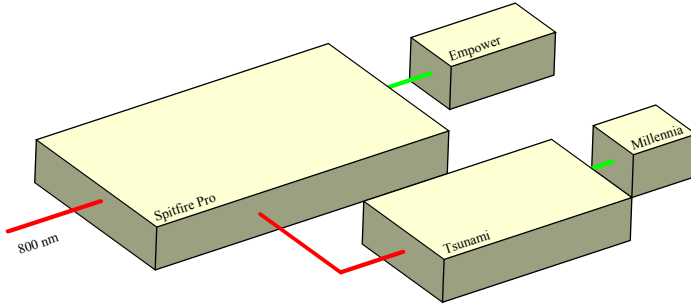


Figure 5.1: The layout of the femtosecond laser system. *Tsunami* laser oscillator is used as a seed laser and pumped by a solid-state pump laser, *Millennia*. The gain medium of *Spitfire Pro* amplifier is pumped by *Empower*. The output beam has 800 nm of wavelength 1 mJ of energy per pulse.

### 5.1.1 Laser amplifier

The mode-locked seed laser is pumped by a CW frequency-doubled Nd:YVO<sub>4</sub> laser and emits  $\leq 100$  fs pulses separated in time as determined by one round-trip through the oscillator cavity. Provided from the seed laser, the femtosecond pulses are focused on the gain medium. The time-delay generator (TDG) controls the selection of individual pulses from the pulse train and injection into the regenerative amplifier by Pockels cells. The pump laser of the amplifier synchronously provides the energy for the gain medium to excite it just prior to the arrival of seed pulses.

Today, the most widely used laser gain medium in mode-locked laser systems is Ti:sapphire. Ti:sapphire is a crystalline Al<sub>2</sub>O<sub>3</sub> doped with Ti<sub>2</sub>O<sub>3</sub> where a small percentage of Ti<sup>+3</sup> ions is substituted with Al<sup>+3</sup> ions [216]. Octahedrally coordinated Ti<sup>+3</sup> ions in 3d<sup>1</sup> coordination are the lasing ions [216, 217], since they form the 4-level energy diagram as shown in Figure 5.2. Both absorption and emission bands of Ti:sapphire are the broadest of any commercial laser. Broad emission spectrum allows these lasers to generate ultrashort pulses [216, 218].

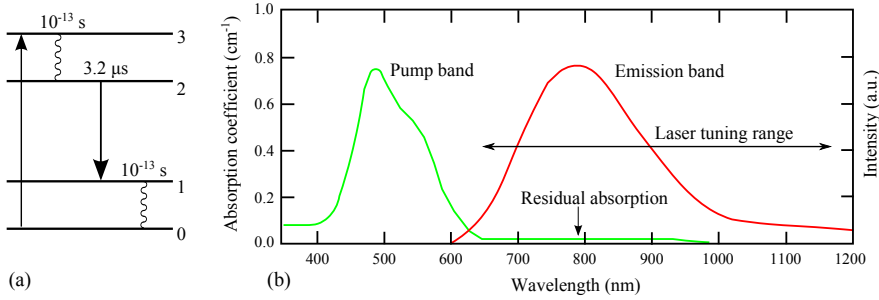


Figure 5.2: (a) Simplified 4-level energy diagram and transitions, taken from [219]. Population inversion takes place at the excited state ( $E = 2$ ) which has a longer lifetime,  $3.2 \mu\text{s}$  for Ti:sapphire. (b) The absorption (pump) and emission bands of a Ti:sapphire crystal. The emission signal shows a peak around 500 nm that allows the crystal to be pumped by frequency-doubled output of a Nd:YLF laser. The maximum of the gain curve (emission band) is located at 800 nm. Figure adapted from [217].

A Ti:sapphire crystal shows high resistance against thermally induced stress, and thus allows long-lasting operational times. However, the high peak power of the amplified laser pulses may create a hazard on the crystal. Furthermore, due to the self focusing effect, the peak power of a pulse in the Ti:sapphire crystal must be limited to  $\sim 10 \text{ GW/cm}^2$ . In order to avoid such crystal hazards, a technique called chirped pulse amplification (CPA) has been developed [220]. This achievement has been awarded by a Nobel prize in 2018.

The fundamental relationship between the duration of an unchirped pulse and its bandwidth is that the shorter pulse durations exhibit a broader bandwidth. This relation is termed as time-bandwidth product and is given for the Gaussian pulses by:

$$\frac{c}{\lambda^2} \Delta\lambda \cdot \Delta\tau \geq 0.441 \tag{5.1}$$

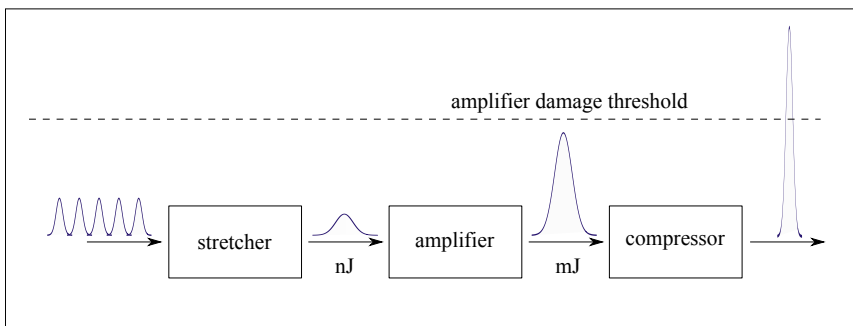


Figure 5.3: A diagram of chirped pulse amplification system.

where  $\lambda$  is the central wavelength,  $\tau$  is the pulse duration and  $c$  is the speed of light. The time-bandwidth product defines the shortest pulse duration. For instance, the seed laser pulses have 46 nm bandwidth at 800 nm central wavelength, and the corresponding pulse duration can be  $\sim 20$  fs. In order to reach the bandwidth-limited pulses, the seed pulses are stretched exploiting the wavelength diversity in their broad bandwidth. Certain wavelengths are delayed relative to the others due to the group velocity dispersion (GVD). This is realized by the grating-based stretcher, see Figure 5.4(a).

A light pulse impinging on a diffraction grating experiences a dispersion and the wavelength components are spatially separated. The dispersed spectrum can be temporally broadened by making shorter (blueish) wavelengths to travel a longer path than the longer (reddish) wavelengths. This will cause reddish wavelengths to exit the stretcher first. Due to the temporal broadening, the peak power of a pulse is reduced while the energy per pulse is kept constant.

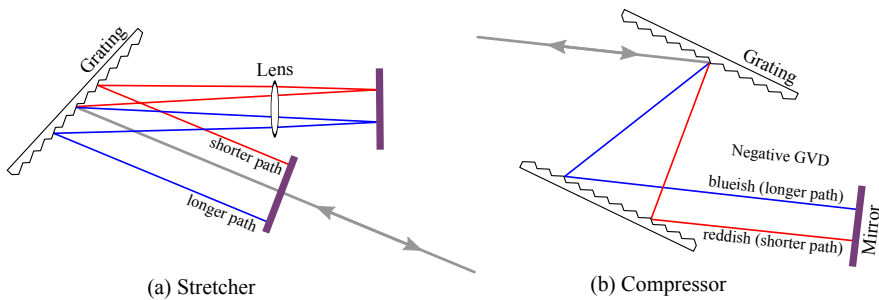


Figure 5.4: Working principles of (a) stretcher and (b) compressor. The fs pulses with a broad bandwidth impinge on the grating of the stretcher which results in a dispersion of the wavelengths. The path difference between reddish and blueish wavelengths temporally broadens the pulse. After amplification process, pulses are directed to the compressor part in order to reverse stretching. Here, it is noted that the pulses are initially flipped by a horizontal retroreflector. Figure adapted from [221].

The stretched pulses are then safely focused on the gain medium which is placed in a cavity resonator. Inside the resonator, pulses are first picked up and thereafter, following a certain amount of round-trips, released by the Pockels cells with a frequency of 1 kHz.

In the compressor part, the spatially spread beam is flipped by a retroreflector so that the reddish wavelengths are forced to take a longer path, hence allowing the blueish wavelengths to catch up. This recompresses the pulse duration to the femtosecond timescales.

## 5.2 Time-resolved MOKE setup

The time-resolved MOKE signal is obtained using a pump-probe technique, where a laser pulse excites the magnetic system and a second, less intense pulse, with a well-defined time delay, measures the magnetic state. The time evolution of magnetic state within tens of picoseconds is plotted by repeating the measurement, while varying the time delay between pump and probe pulses. In between pumping laser pulses, we applied either static or pulsed magnetic fields in order to reset the magnetization to a defined state.

An overview of the experimental setup is shown in [Figure 5.5](#). The fundamental beam is frequency-doubled using a  $\beta$ -barium borate (BBO) crystal in order to separate the blue probe-beam from the scattered light of the red pump-beam. The two colors are split by a dichroic mirror (DCM). The red beam passes through a delay line in order to vary the delay between the beam paths and to find the zero delay position. Following the DCM, the blue beam is transmitted through the prism compressor in order to compensate the chirp effect. The polarization of the pump beam is tuned to linear or circular depending on the experiment. For the probe beam, a linear polarization is used due to the necessity in the MOKE signal detection. The detection of the MOKE signal is done as in the static MOKE setup ([Subsection 4.2.4](#)). The only difference is that the 1 kHz beam modulation is taken from the reference signal of the amplifier, instead of an optical chopper.

### 5.2.1 Determination of pulse duration

In order to provide the required time-resolution in the measurement of ultrafast processes, it is essential to control the pulse duration. As a general rule, the pulse duration has to be much shorter than the timescale of the event. The measured signal is given as the convolution of temporal function of the physical process  $f(t)$  and probe pulse  $g(t)$ :

$$|f * g| \equiv \frac{1}{\sqrt{2\pi}} \int_{-\infty}^{\infty} g(x)f(t-x)dx \quad (5.2)$$

The pulse duration of the fundamental beam can be adjusted using the gratings compressor of the amplifier shown in [Figure 5.4 \(b\)](#). While determining the pulse duration in the femtosecond range, electronic devices are too slow and using another ultrashort pulse is a necessity. The most common method is the *autocorrelation* technique [[222](#)].

**The pulse duration of the red beam** was measured by a commercial autocorrelator capable of detecting 800 nm wavelength (PulseCheck<sup>TM</sup> from APE GmbH). This

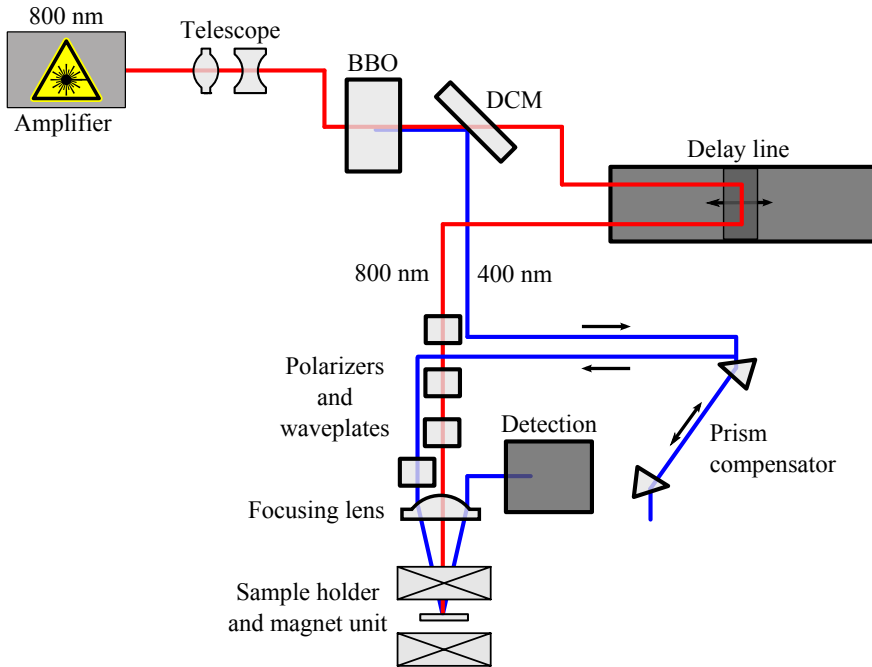


Figure 5.5: Overview of beam path for the time-resolved MOKE experiment. Ultra-short laser pulses with 800 nm wavelength are amplified up to 1 mJ which are needed for excitation of magnetic system. The beam size is reduced using Galilean-type telescope in order to fit beam diameter to the optics. BBO crystal generates the second harmonics (400 nm) of the fundamental. The two colors are separated by dichroic mirror (DCM). Time delay between pump and probe pulses are set by a linear delay line. The probe pulse duration is compressed against the effect of chirp using a pair of prisms. Beam paths are equal between BBO and sample for both colors. In figure, beam paths not to scale.

technique is based on the interference of a laser pulse with an equal pulse split from the same beam. Both pulses are aligned into a non-linear crystal (BBO) at a defined angle such that a third frequency-doubled beam is generated. This third beam is only generated when two pulse spatially and temporally overlap. Therefore, a delay stage is employed to temporally shift the pulses and maximize the signal. The shape of the autocorrelation signal is then a result of the *convolution* of the two pulses [222].

In our experimental setup, the pulse duration of red beam is measured at the sample position. When the beam passes through many optical elements, broadening of the pulses due to the group velocity dispersion (GVD) must be taken into account. This problem is overcome by pre-compensating the pulses with the grating compressor, what typically results in an autocorrelation signal of  $\sim 80$  fs duration. Since the

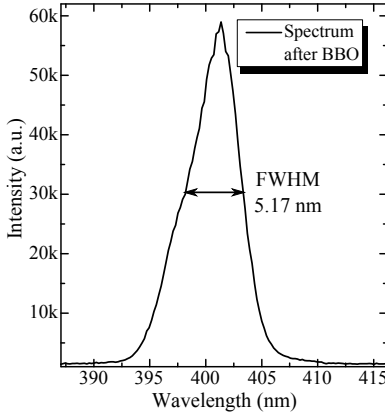


Figure 5.6: Spectrum of the blue beam measured after the BBO crystal. FWHM and the central wavelength are 5.17 nm and 401.4 nm, respectively. Conversion of bandwidth to the pulse duration for transform limited pulses corresponds to  $\sim 46$  fs.

convolution of two Gaussian pulses is a Gaussian pulse as well, the autocorrelation signal is 1.41 times the original pulse. Consequently, pump pulses are found to be around 55 fs -very close to the value specified by the laser design.

**The pulse duration of the blue beam** was measured with a similar technique called *cross-correlation*. Cross-correlation is a convolution of two unequal pulses, i.e. blue and red. Since the pulse duration of red beam is known, the blue pulse duration can be estimated by signal deconvolution. The cross-correlation signal is measured using a two-photon absorption in a photodiode, while temporally scanning the red beam using the delay line. An appropriate photodiode must be relatively insensitive to the single red and blue pulses, but generates strong signal when the photons arrive at the same time. This can be achieved if the band gap is larger than single photon energies, but smaller than their sum [223]. In our setup, a SiC photodiode was employed.

Prior to the pulse duration measurements, the bandwidth-limited pulse duration was estimated based on Equation 5.1. First, the spectrum after the BBO crystal was recorded (Figure 5.6) and the bandwidth is converted to the pulse duration of transform limited pulses using the ToptiCalc software. Accordingly, the blue pulse duration can be as short as  $\tau \sim 46$  fs, nevertheless, due to GVD effects, the measured pulse duration was much longer at the sample position. Therefore, in order to further compress the pulse duration, a prism dispersion compensation system is used. The system is described in the paragraph below.

**The prism compensator** splits the blueish and reddish spectral components of the pulse according to their dispersion. The geometry of the prisms gives rise to a optical path difference between shorter and longer wavelengths. This means that the blueish wavelengths come temporally closer to the reddish wavelengths, see Figure 5.7.

Therefore, compression of pulse duration requires a precise positioning of prisms.

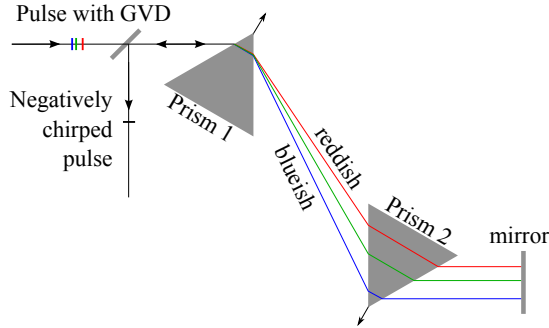


Figure 5.7: Prism dispersion compensator consists of two prism and a mirror. The optical path inside the prisms and the distance in between define the amount of negative GVD. Reproduced from [224].

Cross-correlation measurements were done with a fixed prism distance while the optical path was varied. Table 5.1 shows the temporal FWHM of the cross-correlation signal as a function of the prism 1 position in the direction of arrow.

Table 5.1: Temporal FWHM of cross-correlation signal as a function of prism position.

Prism 1 position	3 mm	5 mm	7 mm	9 mm	11 mm	13 mm
FWHM	178.5 fs	158.3 fs	165 fs	145 fs	128.2 fs	101.5 fs

Finally, the cross-correlation pulse duration values  $\Delta t_{CC}$  were converted to blue beam pulse durations  $\Delta t_{400}$  using the approximation,  $\Delta t_{CC} = [(\Delta t_{800})^2 + (\Delta t_{400})^2]^{1/2}$ , where  $\Delta t$  is the FWHM of individual laser pulse [223]. We were able to compress  $\lambda=400$  nm pulse duration down to  $\tau \sim 85$  fs.

### 5.3 Magneto-optical Kerr microscopy

Methods for magnetic domain imaging can be classified in terms of their physical interaction, information depth as well as spatial and temporal resolution. Magneto-optical Kerr microscopy is one of the fastest techniques regarding the image acquisition time [120, 225]. Our quasi-static all-optical switching experiments required an *in-situ* imaging of the magnetic domains during and after the laser illumination. Therefore, we built a tabletop wide-field Kerr microscopy and coupled it to the femtosecond laser beam as shown in Figure 5.8. Attaching the sample on the micro-step 3D stage, different areas on the sample surface could be illuminated and imaged. This microscope was designed to be sensitive to the out-of-plane magnetization and Köhler illumina-

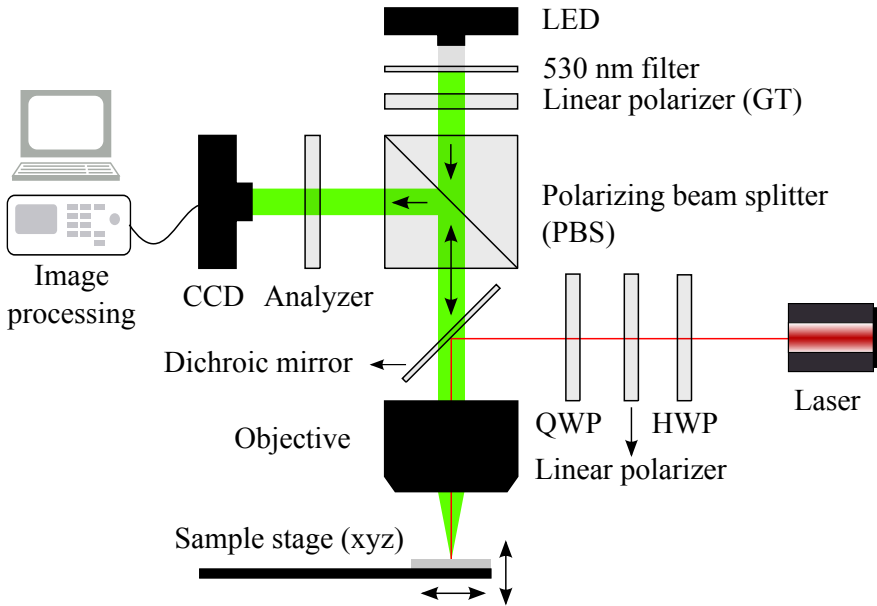


Figure 5.8: Schematics of magneto-optical Kerr microscopy coupled to the fs laser beam (top-view, not to scale). A light-emitting diode (LED) was used as a light source for the Kerr microscope. White LED beam was filtered by 530 nm glass filter in order to separate from imaging beam as well as to maximize the Kerr rotation. The reflected imaging beam was directed towards the charge-coupled-device (CCD) camera by a polarizing beam splitter. Magnetic contrast was detected by a polarization analyzer. While imaging the magnetic domains, the laser beam was focused to the sample through the same objective lens. Laser fluence was tuned using the combination of a Glan-Thompson (GT) linear polarizer and half wave plate (HWP). Polarization state was controlled by the quarter wave plate (QWP). In all-optical switching experiments, laser wavelength and pulse durations were fixed at  $\lambda = 800$  nm and  $\tau \leq 70$  fs, respectively.

tion principles were used in order to achieve an evenly distributed illumination [226]. After reflection from the magnetic surface, the polarization of the light is slightly rotated owing to the magneto-optical Kerr effect. Then, the light is directed towards the CCD camera using a polarizing beam splitter. The imaging beam travels through the analyzer, which is used to detect the magnetic contrast.

The laser beam was directed towards the sample using a shortpass dichroic mirror (DCM) and was focused on the sample surface using the same objective as the LED light. Laser beam fluence was tuned using a linear polarizer (LP) and half wave plate (HWP). Depending on the experimental requirements, linearly polarized light was transformed into circularly polarized light by the quarter wave plate (QWP) [227].



The polarization state was double-checked after reflection by DCM and transmission through the objective, however, no considerable perturbation was observed in the polarization state.

**Illumination** was maintained by using a typical light emitting diode (LED) light source. The advantages of using an LED source are that no cooling system is required and no speckles are observed unlike with the laser imaging methods [228]. A comparison of different light sources is given in Figure 5.9. In addition, LED light provides relatively stable illumination comparing the arc lamps. The white light from the LED source is filtered at 530 nm by a glass filter in order to separate imaging beam from the 800 nm laser beam. In addition, it is known from the literature that shorter wavelengths result in a larger Kerr rotation in Co/Pt multilayers [94].

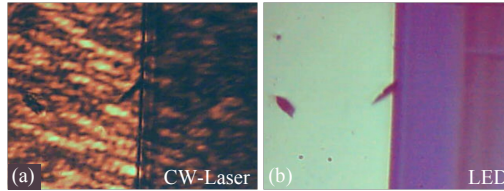


Figure 5.9: Comparison of light sources for optical microscopy. (a) CW-laser: speckles due to diffraction of coherent modes, (b) LED light.

**Köhler illumination** principles have to be applied in order to get rid of the image of the LED source by fully defocusing on the sample surface [226]. This is required for the brightest illumination as well. To achieve Köhler illumination, the emitted light from the LED source is focused at the back focal plane of the objective lens. As a result, the light rays are collimated by the objective lens which, therefore, ensures an even illumination at the sample surface.

**An aperture diaphragm** was centered to the beam in order to cancel out in-plane magnetization components and to be sensitive to only polar Kerr effects. For in-plane magnetic microscopy, the aperture diaphragm should be shifted to an off-centered position. A typical iris was used as aperture diaphragm and we controlled the brightness and resolution by opening and closing the aperture.

**A polarizing beam-splitter** decomposes the s- and p-polarized components of the incident beam onto two orthogonal axes by reflecting the s-component with the dielectric beam-splitter coating. In our experimental setup, we used a polarizing cube for both improving the extinction ratio of the incident polarization and to reflect the s-components towards the CCD camera.

**The magnetic contrast** was obtained by magneto-optical Kerr effect upon reflection from the surface of a ferromagnetic thin film. The imaging beam was initially p-polarized by a Glan-Thompson prism. A polarizing beam splitter (PBS) in the beam path has two-fold effect on the polarization. First, the incoming beam passes through the PBS to increase the extinction ratio. After being reflected from the magnetic surface the beam undergoes Kerr rotation and thus it gains an s-polarized component besides the initial p-polarization. The PBS reflects the s-polarized components of the beam  $90^\circ$  towards the CCD camera (Hamamatsu). A secondary Glan-Thompson prism was set to almost  $90^\circ$  angle with respect to the axis of the first one in order to detect the Kerr rotation. Kerr rotation differs only in sign for two domains with opposite sign. Therefore, nearly crossed polarizer and analyzer pair makes one domain to be brighter and the opposite domain to be darker. If this is not the case due to the elliptical polarization, a compensator (lambda quarter plate) could be introduced to the beam path before the analyzer [92]. In our experiments, magnetic contrast was sufficient for domain imaging and no compensator was introduced.

In order to enhance the magnetic contrast, dielectric anti-reflection coatings can be employed [92]. ZnS and  $\text{Si}_3\text{N}_4$  layers were grown on top of the Co/Pt multilayers. In spite of enhancement on the MOKE signal, these layers were not used for domain imaging due to the large surface roughness.

**Objective** is another critical component affecting the magnetic contrast. Due to the fact that we aim for the polar sensitivity in our microscope, the incidence angle should be as close as possible to the normal incidence. Therefore, we employed a 10X, plan-apochromat objective lens (*Mitutoyo*) with a low numerical aperture (NA) of 0.28. Low NA ensures that the incoming beam reflects back with a smaller angle. The drawback of lower NA, however, is the low resolution in accordance to Rayleigh criterion [120].

**Contrast enhancement** is required in most of the cases since the Kerr rotation is only around  $1^\circ$ . In order to enhance the magnetic contrast we make use of the *ImageJ* image processing software [229]. After magnetic image acquisition, we saturated the sample applying a magnetic field above the coercive field. The image of the saturated sample shows only homogeneous magnetic contrast on top of its topography and was saved as the background image. Then, the image showing magnetic contrast was divided by the background image in order to obtain pure magnetic contrast. Nevertheless, there was still some nonuniform background in the resulting image. ‘A posteriori shading correction’ and ‘Nonuniform background removal’ plugins of ImageJ software were used to remove the polynomial background from the magnetic contrast image.

During the laser illumination, imaging the magnetic domains without the contrast enhancement was quiet difficult. In order to make sure that the laser pulses affect the magnetic domain structure before image acquisition, we made use of an image processor (Hamamatsu). We first saved the topography image and instantaneously subtract this background image during the experiment which allowed us to perform real-time domain imaging.

**The resolution** of the Kerr microscope is theoretically limited by diffraction and is given by  $d \approx 1.21\lambda/2(NA)$  which amounts to  $\sim 1.15 \mu\text{m}$ . The spatial image resolution was experimentally determined by using the edge response method [230]. In Figure 5.10, image intensity profile was obtained from a horizontal rectangle which depicts the region of interest. The resolution is usually calculated as the distance range corresponding to the intensity values between 10%-90%. In our experiment, the spatial resolution is found to be below  $5 \mu\text{m}$ .

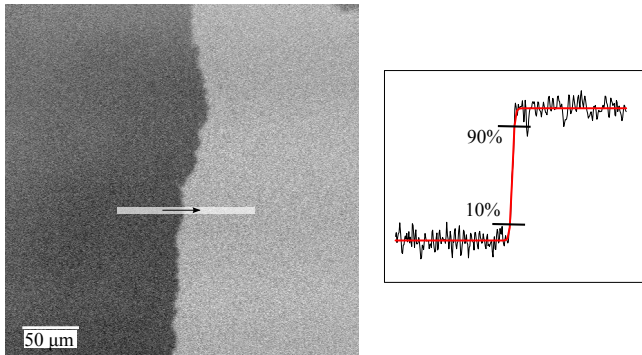


Figure 5.10: Measurement of spatial image resolution by edge response method. Intensity profile (white) and Boltzmann fit function (red) are obtained from 10-pixel-width horizontal rectangle.

**The quarter wave plate** is an optical element made of a birefringent transparent crystal. Birefringent crystals have a varying refractive index for different incidence polarizations. The crystal can be cut in such a way that the axes of maximum index  $n_1$  and minimum index  $n_2$  to be orthogonal to each other. Thickness  $d$  of the crystal is chosen to fulfill the following condition.

$$d(n_1 - n_2) = \lambda_0/4 \quad (5.3)$$

where  $\lambda_0$  is the vacuum wavelength. In this condition, a phase shift of  $\pi/2$  is introduced between two orthogonal components of linearly polarized light, and consequently circularly polarized light is produced [227].

## 5.4 X-ray photoemission electron microscopy

In this work, we used photoemission electron microscopy (PEEM) in connection with x-rays in order to exploit the x-ray magnetic circular dichroism (XMCD) effect for element-specific magnetic domain imaging. The physical mechanism of XMCD effect was already explained in Subsection 2.7.3. Here, we give a brief explanation of the x-rays-in/electrons-out imaging method.

From an experimental point of view, PEEM is used to magnify and to observe the microscopic distribution of the XMCD contrast on the surface of a ferromagnetic material. The XMCD contrast can be considered as a modulation of the  $L_3/L_2$  absorption intensity depending on the angle between magnetization and the helicity of the incoming x-rays. The photon energy is typically tuned to the core level of the desired element in order to obtain a magnetic image by collecting secondary electrons in a two-dimensional image detector. Then the magnetic contrast image is calculated using the images acquired by opposite helicities. Consequently, the magnetic contrast is enhanced and the topographic features are canceled out.

Photoemission electron microscopes use magnetic-electrostatic lenses for electron beam manipulation and focusing. The focusing ability is limited by chromatic and spherical aberration as well as diffraction. Today's microscopes did not reach the diffraction limit, however, aberration may still pose a problem. Aberration can be corrected using an electron mirror with a reflecting electrode which applies sufficiently high negative potential to reverse the propagation direction of electron beam and adjust the aberration coefficients [231].

In our experiments, a FE-LEEM P90 AC [232] photoemission electron microscope with aberration corrector (*SPECS Surface Nano Analysis GmbH*, see Figure 5.11(a)) was employed for *ex-situ* imaging of magnetic domains at high-resolution. The microscope is located at the UE56-1/SGM beam line of Research Centre Jülich, at BESSY-II storage ring in Helmholtz-Zentrum Berlin (HZB).

### 5.4.1 FE-LEEM P90 at UE56/1-SGM beamline

The x-rays used in this beamline are generated by UE56/1 elliptical undulator implemented at the BESSY-II storage ring and is capable of generating soft x-rays within the 55 - 1500 eV energy range. The undulator consists of periodic magnet-arrays that can manipulate the trajectory of the electrons and consequently the polarization of the generated radiation [233]. For magnetic imaging, XMCD requires x-rays of right and left circularly polarization. Circularly polarized x-rays are produced by shifting

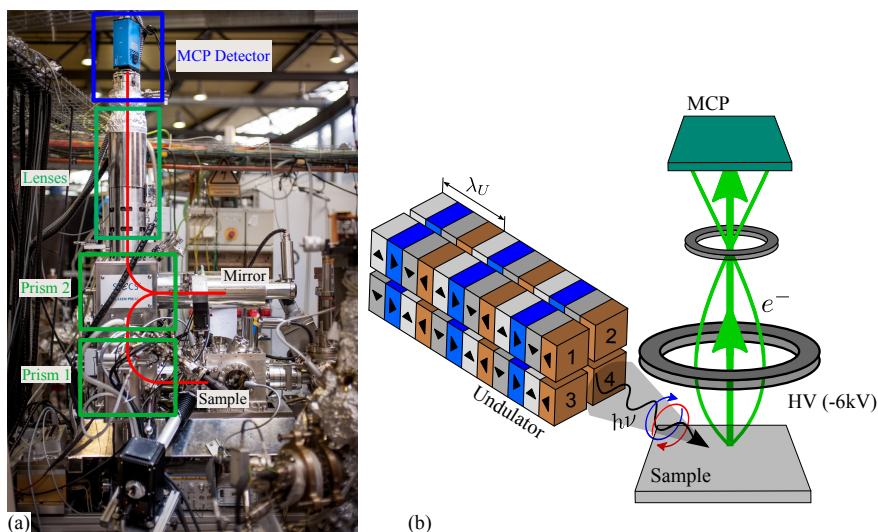


Figure 5.11: (a) A layout of the photoemission electron microscopy (the red line marks the electron path). (b) Schematics of imaging process. X-rays are generated in UE56/1 elliptical undulator and impinge on the sample at an angle of  $20^\circ$ . Circularly polarized x-rays are generated by shifting the crosswise magnet arrays for a quarter-period.

the magnet-array of undulator by  $\pm\lambda_u/4$ , where  $\lambda_u$  is the magnet periodicity. In order to guide the synchrotron radiation through the beamline, a set of guiding mirrors and spherical gratings is used [233].

The incident monochromatic x-ray photons illuminate the sample at an angle of  $20^\circ$  measured from the sample surface. The sample is at a potential of -6 kV with respect to the ground, which accelerates the electrons through lenses. The layout of the LEEM/PEEM microscope is shown in Figure 5.11(a). Prism 1 (used only in LEEM mode) separates the incoming electrons from the gun lenses and the reflected electrons from sample. The reflected electrons are then directed to the electron mirror for correction of spherical and chromathic aberration [231]. Prism 2 separates the electrons incoming from sample from the electrons reflected from the mirror. A set of lenses then projects the aberration corrected image with a final magnification to the multi-channel plate (MCP) detector. Figure 5.11(b) shows schematically the imaging process.

The PEEM instrument is also equipped with electron-beam, apparatus which was used for determining approximate  $T_C$  values of the samples, see Appendix C.

# Chapter 6

## Optical control of magnetization in Co/Pt multilayers<sup>1</sup>

Having discussed the fundamental considerations of the ultrafast magnetism phenomena in [Chapter 3](#), this chapter will focus on all-optical switching (AOS) experiments in [Co/Pt]<sub>N</sub> multilayers. All-optical switching denotes optically-induced magnetization reversal, where femtosecond laser pulses are used to manipulate the magnetization state. The term all-optical domain formation (AODF)<sup>2</sup> is preferred to describe the magnetic domains formed due to thermal processes as a result of the laser illumination.

### 6.1 Quasi-static all-optical switching of magnetization

#### 6.1.1 Methodology of all-optical switching experiments

In all-optical switching experiments, shown in [Figure 5.8](#), the fs-laser beam was precisely adjusted and characterized in order to establish a better control of the beam polarization, pulse duration, fluence and spot size. The polarization state of the beam was checked using two crossed Glan-Thompson (GT) polarizing prisms and a quarter-wave-plate (QWP) located in between the GTs. By rotating the QWP around the axis parallel to the beam propagation, the transmitted beam was first completely extinguished, so that linear polarization is ensured after the wave-plate. After the second GT prism is removed, right and left circularly polarized light was produced by rotating the QWP by  $\pm 45^\circ$  with respect to the plane of linear polarization. The pulse duration was measured by an autocorrelator after the objective lens. In all experiments, the laser pulse duration was kept below 70 fs. The laser power was measured using a thermal-sensor powermeter with  $\pm 5 \mu\text{W}$  precision. The spot size of the beam was measured using a knife-edge method exactly at the sample position. Details of

---

<sup>1</sup>Partly adapted from Parlak *et al.*, Phys. Rev. B, 98(21) 2018 [234].

<sup>2</sup>This term is used as ‘thermal demagnetization’ in some publications.

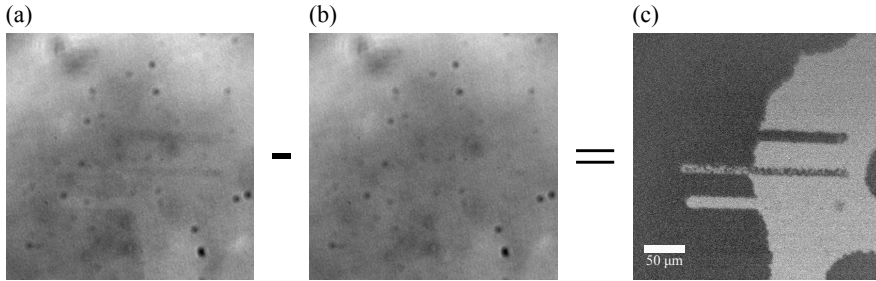


Figure 6.1: Contrast enhancement process of magnetic domain images. (a) Laser illuminated magnetic domains with very low contrast ratio. (b) Single domain magnetic image after sample saturation using a permanent magnet. (c) Background subtracted magnetic image with high contrast ratio and noise and structural imperfections removed.

the pulse duration and spot size measurements are given in [Appendix A](#). Precise positioning of the sample was carefully checked, because of its importance for preventing any possible variation of the spot size along the sample motion direction.

The low temperature switching experiments were carried out in the Helium-flow cryostat (see [Appendix B](#)). The window of the cryostat did not introduce measurable depolarization effects. The long working-distance objective allowed imaging of the sample located inside the cryostat.

Almost in all experiments, a long, vertical domain wall was induced with the help of a permanent magnet brought close to the sample. During the fs-laser illumination we made sure that there is no magnetic field in the affecting on the sample. After the laser illumination, images of the magnetic state were recorded with 0.52 s acquisition time and 5X frame accumulation. In the next step, the sample was magnetically saturated to form the background image that was then recorded for magnetic contrast enhancement (see [Figure 6.1](#)). The effects of uneven illumination were corrected by a polynomial background correction method using the ImageJ image processing program [229].

The size of the optically-induced magnetic domains is usually of the order of the lateral resolution of the Kerr microscopy. Therefore, magneto-optical images of those domains appear as an intermediate ‘grey-color’ depending on the ‘up’ and ‘down’ domain concentration ratio. In order to quantify the optically-induced magnetic domain state, we defined the normalized domain contrast parameter,  $p$ , which ranges between bright and dark colors associated with the saturated domain states. The normalized domain contrast averaged over a certain illuminated area is determined by

the fractions of ‘up’ and ‘down’ domains,  $f_{\uparrow}$  and  $f_{\downarrow}$  respectively, where  $f_{\uparrow} + f_{\downarrow} = 1$ . Accordingly, the averaged net magnetization pointing perpendicular to the film plane is proportional to  $p = (f_{\uparrow} - f_{\downarrow} \times 100)$ .

In order to prepare samples for XMCD-PEEM experiments, the samples were first structured by photolithography and sputtering techniques to mark the regions of interest. These regions were illuminated using the laser beam at our laser laboratory in Research Centre Jülich. The markers allow the determination of the illuminated positions using the microscope’s  $\sim 100 \mu\text{m}$  FOV on  $5 \times 5 \mu\text{m}^2$  samples. When the position was found, images were recorded using RCP and LCP x-rays tuned to the Co L<sub>3</sub> absorption edge at 778.1 eV. The XMCD-PEEM imaging technique allowed us to observe individual magnetic domains. The domain images were binarized using ImageJ software for their quantitative analyses.

### 6.1.2 AOS dependence on laser fluence

Earlier experiments show that a homogeneously magnetized film breaks into randomly distributed domains when exposed to a large optically-induced thermal load [34, 160, 169]. In order to define the optimum fluence required for all-optical switching, and to avoid magnetic film overheating, the laser fluence was gradually increased until domain formation was observed. The sample was mounted on a linear stage and moved with the minimum possible velocity ( $1 \mu\text{m/s}$ ). Figures 6.2 (a)-(c) show the domain structure of the [Co/Pt]<sub>3</sub> multilayer after illumination with three laser fluence levels (0.68, 0.80 and  $1.31 \text{ mJ/cm}^2$ ).

At the same time, each of the Figures 6.2 (a)-(c) shows also the light polarization dependent response for left circularly ( $\sigma^-$ ), right circularly ( $\sigma^+$ ), and linearly ( $\pi$ ) polarized light in the same field of view. Examination of the magnetic contrast reveals two types of magnetic responses of the illuminated area: (i) all-optical domain formation, denoting the formation of random distributions of domains; and (ii) all-optical switching, meaning the complete magnetization reversal of the illuminated area. A detailed analysis of the illuminated areas using x-ray photoemission electron microscopy confirms that no magnetization tilt is induced.

In order to analyze the magnetic contrast in the obtained images, the  $p$  profiles of the laser illuminated lines in Figure 6.2 (d)-(f) have been measured within the areas of the dashed rectangles shown in Figure 6.2 (a)-(c). The  $p$  value is defined by horizontal binning the pixel intensities within the defined rectangles. The  $p$  profiles are plotted along the black and red arrows. Comparing the  $p$  profiles of the laser illuminated lines with the reference bright and dark levels of homogeneously magnetized areas, we



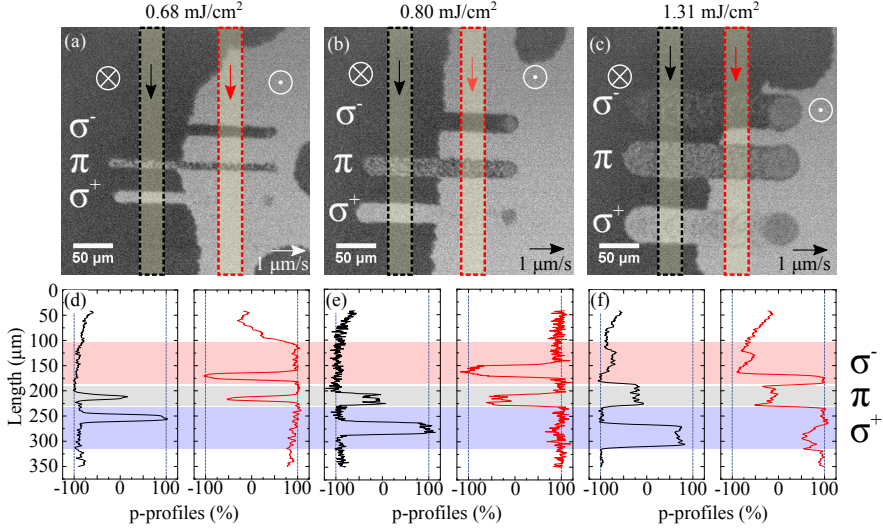


Figure 6.2: Laser fluence dependence of AOS in a  $[\text{Co/Pt}]_3$  multilayer. Kerr microscopy images show laser illuminated areas after inducing AOS/AODF with a laser fluence of (a)  $0.68 \text{ mJ/cm}^2$ , (b)  $0.80 \text{ mJ/cm}^2$  and (c)  $1.31 \text{ mJ/cm}^2$ . Profiles of the normalized domain contrast  $p$  are given in (d)-(f) for areas marked by dashed rectangles in the corresponding Kerr microscopy images (a)-(c). The relative positions of  $\sigma^+$ ,  $\pi$ , and  $\sigma^-$  polarized light are depicted by blue, gray and red backgrounds respectively.

observe that the  $[\text{Co/Pt}]_3$  multilayer exhibits a full AO-HDS at  $0.68$  and  $0.80 \text{ mJ/cm}^2$  laser fluences. At an increased laser fluence of  $1.31 \text{ mJ/cm}^2$ , the analysis shows a helicity-dependent AODF with the  $p$  values close to  $\pm 75\%$  for both left and right circularly polarized light. On the other hand, linearly polarized light results in  $p \approx 0\%$  for all tested laser fluences. Below the laser fluence of  $0.68 \text{ mJ/cm}^2$ , neither AOS nor AODF was observed (no domain formation). These results confirm earlier reported observations that a certain optimum heating in connection with the light helicity is necessary in order to observe AOS [34, 166].

### 6.1.3 AOS dependence on number of pulses

As noted in **Chapter 3**, AOS in ferromagnetic thin films requires multiple laser pulses. To elucidate the effect of pulse accumulation on AOS and AODF in more detail, the sample surface was illuminated in two different ways. First, the sample was moved with different speeds in order to indirectly vary the number of pulses per unit area. And second, a chosen spot was illuminated without moving the sample for an exactly defined time interval. These two cases are described in the following.

### 6.1.3.1 Sweeping beam

In the first experiment, the sample sweeping speed was varied from  $1 \mu\text{m/s}$  to  $50 \text{ mm/s}$  in order to control the areal pulse density while the laser fluence was kept *constant* at  $1.15 \text{ mJ/cm}^2$ , which is slightly larger than the minimum required fluence. This made the lines broader and allowed us to obtain better statistics in terms of the  $p$  profiles along the illuminated lines as shown in [Figure 6.3](#).

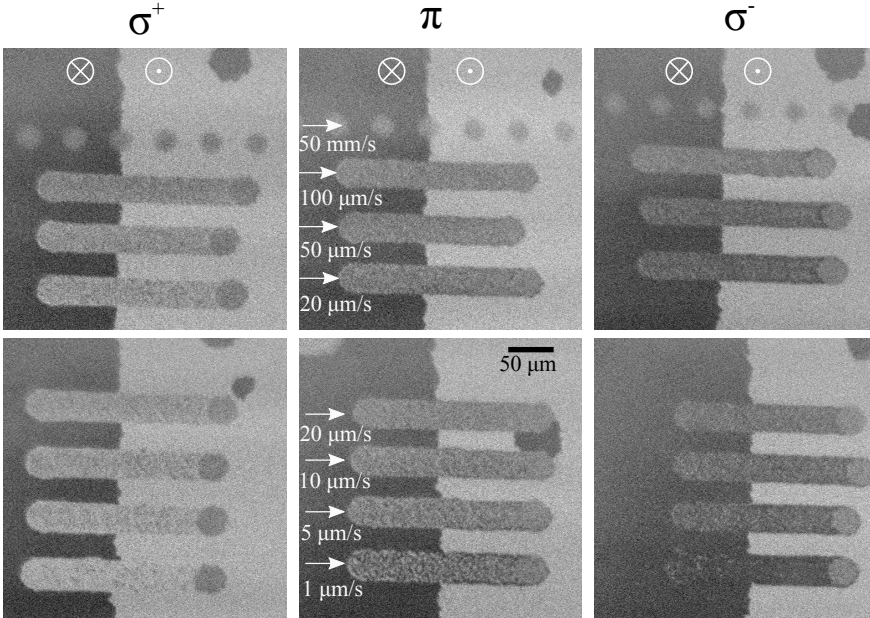


Figure 6.3: Number of pulse dependency of AOS in a  $[\text{Co/Pt}]_3$  multilayer. Kerr microscopy images show the illuminated lines with a laser fluence of  $1.15 \text{ mJ/cm}^2$ . The sample was swept with different speeds from  $1 \mu\text{m/s}$  (bottom) to  $50 \text{ mm/s}$  (top) where the individual pulses landed on different positions. The domain contrast becomes distinguishable for  $\sigma^+$  (left),  $\pi$  (middle) and  $\sigma^-$  as the sample is moved at slower speed.

For the analysis of the  $p$ -profiles from the illuminated lines, a horizontally-elongated rectangular box was chosen, which covers the line itself as well as the white and black background domains. An example of this process is given in [Appendix D](#).

To take the number of pulses into account for the lines which are formed due to a huge number of pulses, we define the *areal pulse density* (APD) term, which depends only on the sample motion speed. This term describes how many pulses impinge on the unit area and neglects the fact that the pulses have a Gaussian intensity profile. For the calculation of the areal pulse density, a unit area is chosen as depicted by the

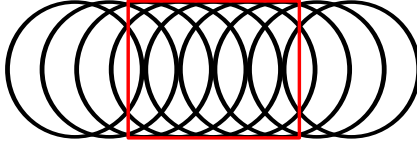


Figure 6.4: Calculation of areal pulse density for a laser illuminated line. The unit area depicted by red rectangle.

red rectangle in Figure 6.4.

The short edge of the rectangle is the  $1/e^2$  diameter of the beam, while the long edge is defined as sweeping speed times the illumination time period. The number of pulses per unit area is then calculated by Equation 6.1, where laser repetition rate and beam diameter are constants during the experiment.

$$\text{Areal pulse density} = \frac{\overbrace{\text{Repetition rate} \times \text{Time}}^{\text{Number of pulses}}}{\underbrace{\text{Diameter} \times \text{Speed} \times \text{Time}}_{\text{Unit area}}} = \frac{\text{Repetition rate}}{\text{Diameter} \times \text{Speed}} \quad (6.1)$$

The calculated  $p$ -values as a function of areal pulse density (and sample sweeping speed) are plotted in Figure 6.5 for three different beam polarizations. Our analysis confirms that a larger *areal pulse density* results in a stronger domain contrast, which means that almost a complete magnetization reversal is achieved with right or left circular polarizations. As the sample is swept faster, the  $p$ -values approach zero for both helicities. The behavior of the  $p$ -values fit logarithm of the sweeping speed. On the other hand, the  $p$ -profiles for linearly polarized beam remain constant with a slight offset from zero. A small offset is assumed to originate from the finite size of the

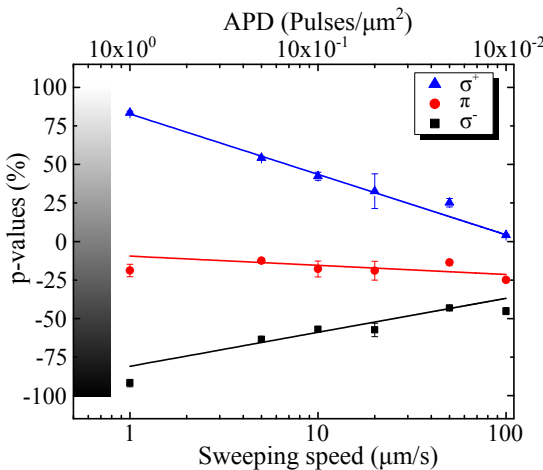


Figure 6.5: Normalized domain contrast,  $p$ -values for three different polarizations as a function of log of sample sweeping speed. The laser fluence was kept constant at  $1.15 \text{ mJ/cm}^2$ . The APD is given in the upper abscissa. The lines are linear fitting curves for the data points. A gray-scale is given on the left side which represents the actual domain contrast. We note that +100% and -100% represent white and black background domains, respectively.

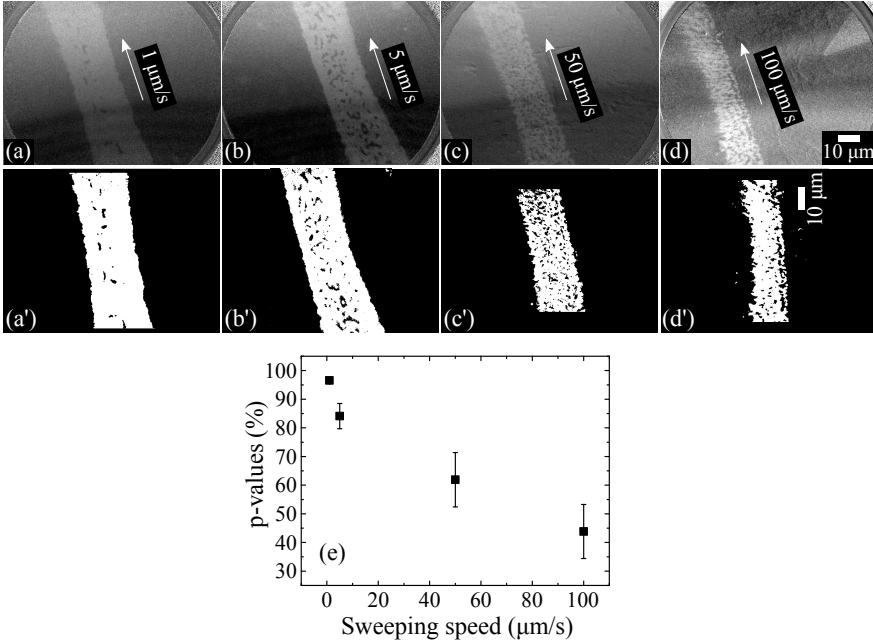


Figure 6.6: XMCD-PEEM images of optically induced magnetic domains on dark background domains with  $104 \mu\text{m}$  FOV. Laser fluence ( $0.89 \text{ mJ}/\text{cm}^2$ ) and polarization state ( $\sigma^+$ ) were constant while the sample was moving at different velocities: (a)  $1 \mu\text{m}/\text{s}$ , (b)  $5 \mu\text{m}/\text{s}$ , (c)  $50 \mu\text{m}/\text{s}$  and (d)  $100 \mu\text{m}/\text{s}$ . The binarized images (a')-(d') are shown under each XMCD-PEEM image. At lower speeds (a' and b'), magnetization at the edges of the lines is completely switched in accordance with Gaussian intensity profile. The ratios of the white and black domains are calculated in the region of interest using image processing software. These ratios, then, converted to the  $p$ -values which are shown in (e). Larger error bars in higher speeds are due to the undefined edges as a result of increased pulse-to-pulse distance.

sampling area. All-optical domain formation is independent of the initial background magnetization.

The above-described experimental results highlight the importance of the number of pulses for a given laser fluence. However, no observable effect of the Gaussian intensity profile was observed due to the low resolution of the magneto-optical Kerr microscopy. In order to improve the magnetic lateral resolution, we employed XMCD-PEEM microscopy for a detailed imaging of the illuminated lines. A set of magnetic domain images obtained at different sample sweeping speeds is shown in Figure 6.6 (a)-(d).

The raw images presented in Figure 6.6 (a)-(d) exhibit an uneven x-ray illumination

due to the beam profile, which prohibits a quantitative analysis. Unwanted x-ray beam profile and the effects of uneven illumination were corrected particularly using the *adaptive threshold correction* method in ImageJ. Then, the images of the illuminated area were transformed into a binary representation in order to calculate the ratio of white and black domains in the region of interest. The results are shown in Figure 6.6 (a')-(d'). In the first two images ((a') and (b')), a complete AOS is observed at the edges of the lines, while black domains still exist at the central part in accordance with a Gaussian intensity profile. In case of the sweeping speed of 50 and 100  $\mu\text{m/s}$  ((c') and (d')), the lateral distance between the pulses is increased, which gives rise to the undefined edges for the lines, and therefore, no profile is observed.

The calculated white-black domain ratios were converted into  $p$ -values as shown in Figure 6.6(e). We conclude that the results of XMCD images are in good agreement with the Kerr microscopy images. The  $p$ -values are calculated as an average over the illuminated area and the lateral profiles are neglected.

In Figure 6.7, we present the sweeping speed dependence of the  $p$ -values for all tested laser fluences. These and the earlier results presented above point to the fact that a complete AOS requires the slowest available sweeping speed, i.e., the largest areal pulse density and an optimum laser fluence just above an intensity threshold. At increased laser fluences, however, only *helicity-dependent* AODF is observed.

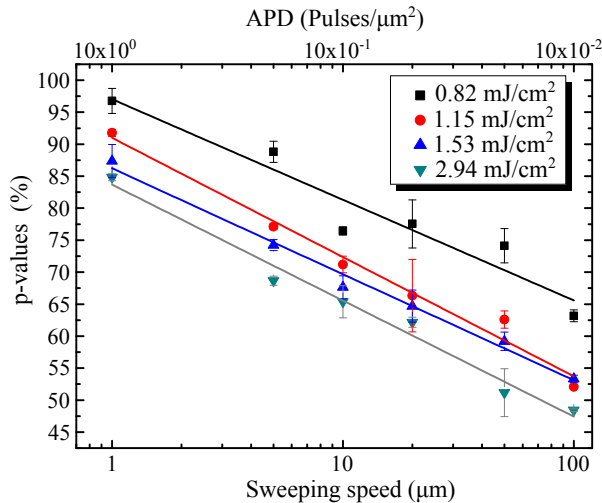


Figure 6.7: Normalized domain contrast,  $p$ -values, for given laser fluences as a function of the sweeping speed. Only  $\sigma^+$  polarization is presented for simplicity. The lines are linear fitting curves for through data points.

This fact has been further confirmed for our samples using a laser beam with much faster pulse repetition rate. Figure 6.8 shows the AOS results for the same [Co/Pt]<sub>3</sub> sample using the laser beam with 5.2 MHz repetition rate and 38 fs pulse duration. In this experiment, the sample movement was not precisely controlled and therefore the areal pulse density was not clearly defined. Nevertheless, a complete and homogeneous helicity-dependent AOS is observed for  $\sigma^+$  and  $\sigma^-$  polarizations. This means that sweeping speed does not matter at higher repetition rates of the laser beam<sup>3</sup>.

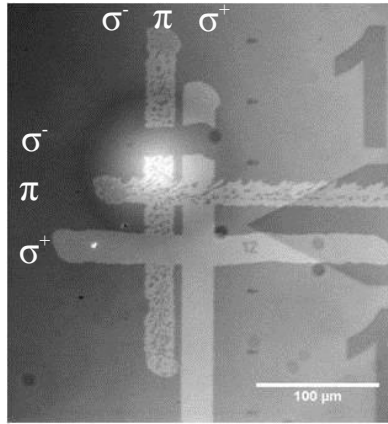


Figure 6.8: Kerr microscopy images of illuminated areas using 5.2 MHz repetition rate and 38 fs pulse duration. Vertical lines were drawn first, then followed by horizontal ones. Complete AOS is observed for both  $\sigma^+$  and  $\sigma^-$  polarizations. We note that the bright spot, which appears on the image is due the uneven sample illumination.

### 6.1.3.2 Static beam

In order to elucidate the effect of pulse accumulation on AOS and AODF in more detail, a chosen spot at the sample surface was illuminated without moving the beam across the sample surface, see Figure 6.9. The number of pulses impinging on the sample was defined by opening a beam shutter for a defined period of time. Only the single pulse illumination was done with the help of the translation stage by increasing its speed to 50 mm/s, such that there is no spatial overlap between consecutive pulses. We started the illumination with a low laser fluence of 0.80 mJ/cm<sup>2</sup>, where single pulses resulted in no observable effects (see inside of the red dashed rectangle in Figure 6.9 (a)). For an increased laser fluence of 1.31 mJ/cm<sup>2</sup>, single pulses result in AODF regardless of the beam polarization, as shown in the first two rows of spots in Figure 6.9 (b). Further accumulation of pulses ( $\geq 10^3$ ) at both 0.8 and 1.31 mJ/cm<sup>2</sup>

<sup>3</sup>We acknowledge C. Riedel and Dr. A. Kakay at Helmholtz-Zentrum Dresden for both switching and imaging experiments using a high-repetition rate laser.

laser fluence levels resulted in (i) AODF at the center of the spot, (ii) an increase of the spot diameter, and (iii) the formation of a completely switched ‘AOS ring’ at the perimeter of an illuminated spot. The evolution of the radial intensity profile with respect to an increasing number of pulses is shown in Figure 6.9 (c)-(d).

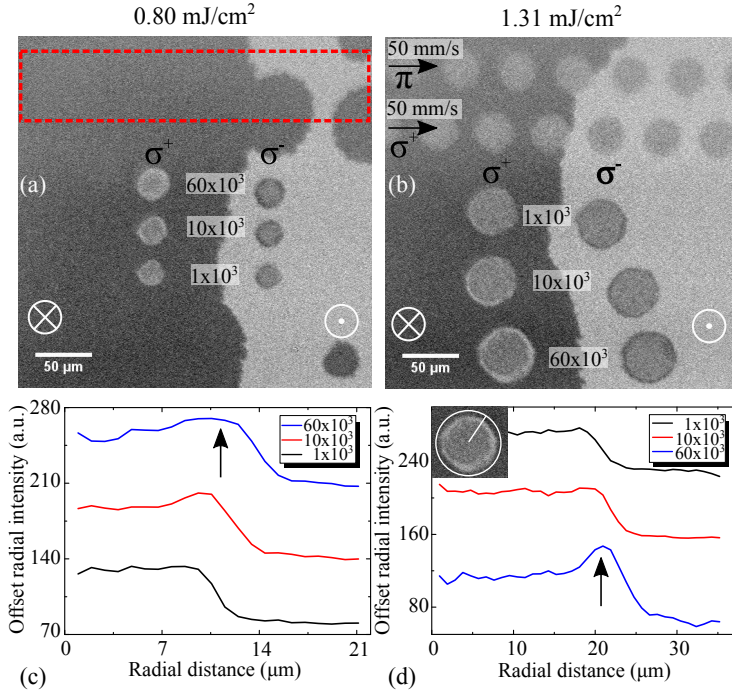


Figure 6.9: Kerr microscopy images of the [Co/Pt]<sub>3</sub> multilayer after laser illumination on a chosen spot. The dashed rectangle in (a) depicts the area illuminated by the single pulses with a fluence of 0.80 mJ/cm<sup>2</sup> with no observable AOS or AODF. The effect of single pulses is not observed by optical imaging. Below this area the sample was illuminated with a static beam with 1 kHz repetition rate for varying time durations. Right ( $\sigma^+$ ) and left ( $\sigma^-$ ) circularly polarized light was exposed to white and black background domains, respectively. (b) The same approach with 1.31 mJ/cm<sup>2</sup> laser fluence. The first two rows from the top show AODF as a result of single-pulse illumination regardless of polarization. (c) and (d) The radial intensity profiles of the corresponding spots. The inset in (d) shows the region of interest. The profiles are vertically offset for clarity and arrows mark the fully switched ‘AOS ring’ at the perimeter of the illuminated spot. Note that the three larger round domains (top right) and one smaller domain (bottom right) are not optically induced domains. They are the background domains induced by a static external magnetic field.

We note that the broadening of the optically induced magnetic domain lines in the experiment shown in Figure 6.2 was associated with  $1/e^2$  diameter broadening of the laser pulses that scales with the increasing laser fluence. In contrast, in the latter

experiment shown in Figure 6.9, the *broadening* of the laser illuminated spots scales with the *number of pulses*. This is especially evident at a laser fluence of  $0.80 \text{ mJ/cm}^2$ , where the area of the AODF spot size increases 1.25 times between  $10^3$  and  $6 \times 10^4$  pulses. Since the laser fluence is the same for every illuminated position, this effect can be ascribed to a *radial heat propagation* around the illuminated spot.

In order to investigate the onset and evolution of the ‘AOS ring’ and its dependence on the pulse accumulation, we illuminated a defined spot using a varying number of pulses. As the magnetic domains upon low number of pulses are either not formed or beyond the resolution of Kerr microscopy, we employed XMCD-PEEM imaging to explore the domain evolution as a function of the fluence and number of pulses. The set of domain images are shown in Figure 6.10.

It is important to note here that single pulses at  $\sim 2 \text{ Hz}$  repetition and  $1.02 \text{ mJ/cm}^2$  fluence do not induce magnetic domains. However, at  $1 \text{ kHz}$ , there are domains observed. This leads to the conclusion that not only the accumulation of pulses is critical for AOS, but also the frequency of pulses is an important factor. The qualitative analysis shows that the ‘AOS ring’ does not appear up to  $1 \times 10^3$  pulses. For a further understanding, we illuminated pulses by manually triggering for 1 to 500 times and imaged using the XMCD-PEEM technique, see Figure 6.11.

The analysis revealed that the spot size rapidly increases at first, and saturates at a large number of pulses, and at 200 pulses, the ‘AOS ring’ starts to partially form. However, this cannot be quantitatively shown as a clear peak, since the spots are not perfectly round and the ‘AOS ring’ is very narrow.

#### 6.1.4 AOS dependence on bilayer repetition

A natural question to ask at this point is, which parameters actually determine the ‘optimum’ laser fluence interval at which AOS occurs. In order to expand our insight, we varied the coercivity ( $H_C$ ) of the  $[\text{Co/Pt}]_N$  multilayers by changing the bilayer repetition number  $N$ , and looked for the optimum laser fluence to induce AOS. First, a  $[\text{Co/Pt}]_3$  sample was illuminated with a fluence ( $0.82 \text{ mJ/cm}^2$ ) which is already known to be able to switch this sample (see Figure 6.12 (a)). Then, keeping the laser fluence constant, the  $[\text{Co/Pt}]_5$  multilayer was illuminated. As Figure 6.12 (b) shows, this fluence turned out to be insufficient to induce either AODF or AOS. In order to induce AODF/AOS in the  $[\text{Co/Pt}]_5$  sample, the fluence had to be increased by  $\sim 0.3 \text{ mJ/cm}^2$ , i.e., by more than 30% (Figure 6.12 (c)). For the multilayer with  $N=7$  the fluence must be increased by yet another  $\sim 0.3 \text{ mJ/cm}^2$  to achieve AODF, shown in Figures 5 (d) and (e).



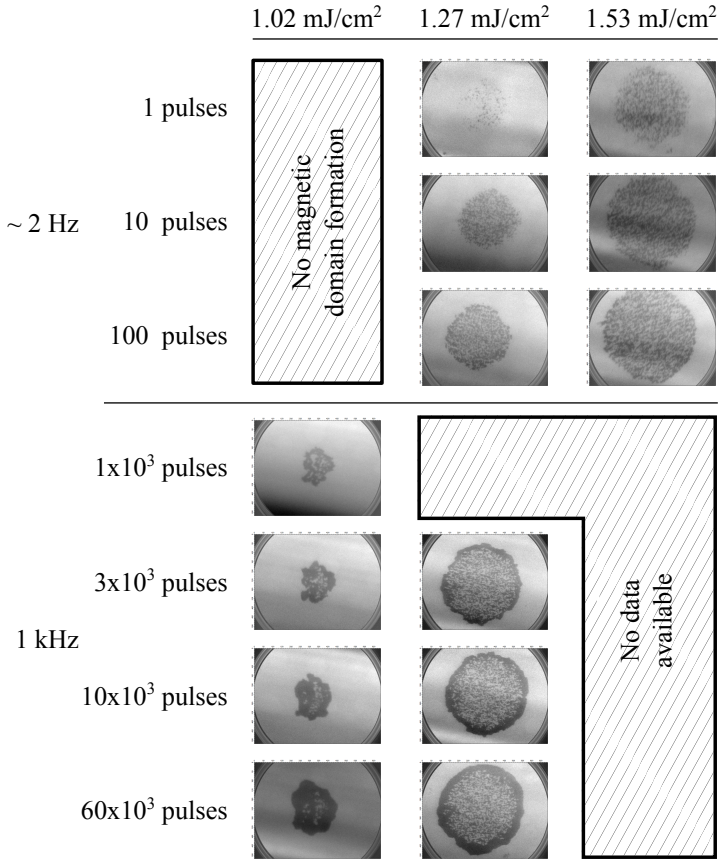


Figure 6.10: XMCD-PEEM images of magnetic domains formed upon 1 to  $60 \times 10^3$  pulses. From left to right, laser fluence increases from 1.02 to 1.53 mJ/cm<sup>2</sup>. We note that pulses between 1 and 100 were manually triggered with a repetition rate of  $\sim 2$  Hz, while larger number of pulses were controlled with a timed shutter. At 1.02 mJ/cm<sup>2</sup> fluence, no magnetic domain was formed for 1, 10 and 100 pulses. Domains appear at the larger fluences even with a single pulse. ‘AOS ring’ formation is not observed below  $1 \times 10^3$  pulses. For 1.53 mJ/cm<sup>2</sup>, no data available because of experimental reasons.

In order to elucidate the relation between coercive fields  $H_C$  and the minimum fluence  $F_{min}$  required for the onset of AODF, we calculated the ratio  $F_{min}/H_C$  that turns out to be almost the same for all samples,  $F_{min}/H_C \sim 0.018 \text{ mJ cm}^{-2} \text{ mT}^{-1}$ , thus revealing the important role of  $H_C$  for determining  $F_{min}$ . It is noted that in the latter experiment, the increased laser fluence did not result in the line broadening similar to the one shown in Figure 6.2 even though an increase of the laser fluence by  $\sim 72\%$  was necessary to induce AODF in the sample with  $N=7$  compared to  $N=3$ . In all these

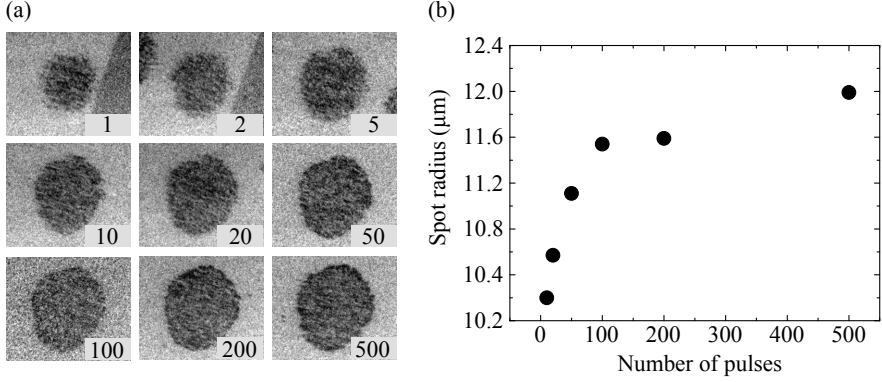


Figure 6.11: Evolution of spot size as a function of number of pulses. (a) Images of magnetic domains acquired by XMCD-PEEM imaging. The domains were formed by manually-triggered ( $\sim 2$  Hz) pulses. (b) Spot radii were calculated from radial intensity profiles.

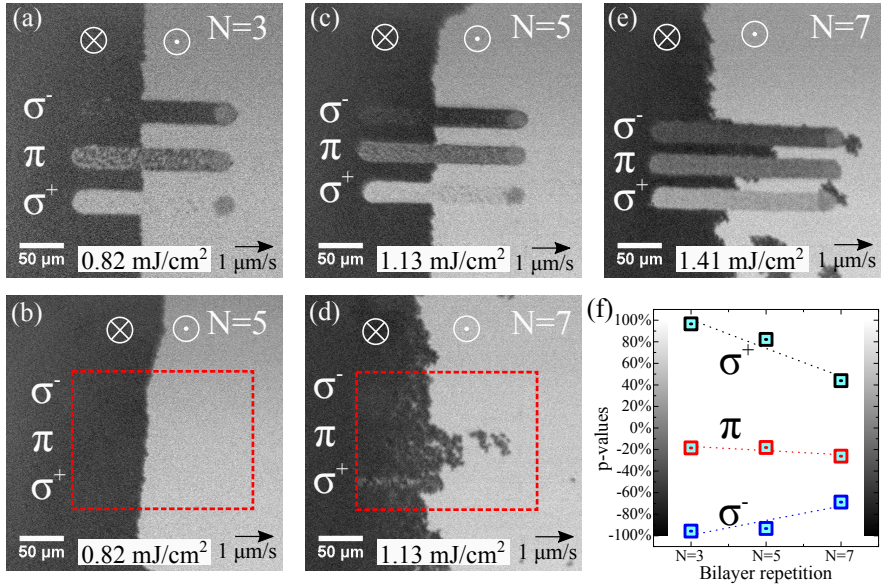


Figure 6.12: Kerr microscopy images of  $[\text{Co/Pt}]_N$  multilayers for (a)  $N=3$ , (b)-(c)  $N=5$ , and (d)-(e)  $N=7$ . For every  $N$ , laser fluence was tuned in order to reach the minimum level  $F_{min}$  required to achieve AODF. Dashed red rectangles in (b) and (d) depict the laser illuminated areas for  $N=5$  and  $7$ , where the fluence level  $F_{min}$  determined for  $N=3$  and  $5$ , respectively, is not sufficient to affect the magnetization. (f) Normalized domain contrast,  $p$ -values, as a function of  $N$  and beam polarization. See Appendix D for  $p$ -profiles. The dotted lines are guides for the eyes. The error bars are inside the squares.

experiments, the laser fluence was increased very slowly in steps of only  $0.05 \text{ mJ/cm}^2$  in order to identify the minimum fluence  $F_{min}$  affecting the particular sample.

Figure 6.12 (f) shows the  $p$  values calculated from the scans along the illuminated lines. We find that the  $p$  values vary with  $N$  and have the highest value for the multilayer with the lowest  $N$ .

## 6.2 Domain formation and relaxation mechanism

The above observations show that the *optically induced heating* is the essential parameter affecting AOS. Therefore, in the next step the  $[\text{Co/Pt}]_3$  multilayer was cooled down to cryogenic temperatures in order to reduce the maximum temperature reached due to optically induced heating of the sample, and to partially inhibit AOS and AODF processes. In addition, the time interval between consecutive pulses was increased by lowering the laser repetition rate. This allowed a more efficient cooling of the sample during the period between impinging laser pulses. In Figure 6.13(a)-(c), the horizontal direction (from the left to the right) represents an increase of the pulse-to-pulse time interval from 1 to 50 ms corresponding to laser pulse repetition rates from 1 kHz to 20 Hz. The vertical direction (from the top to the bottom) represents an increase of the number of laser pulses from  $10^3$  to  $3 \times 10^4$  applied to one particular spot.

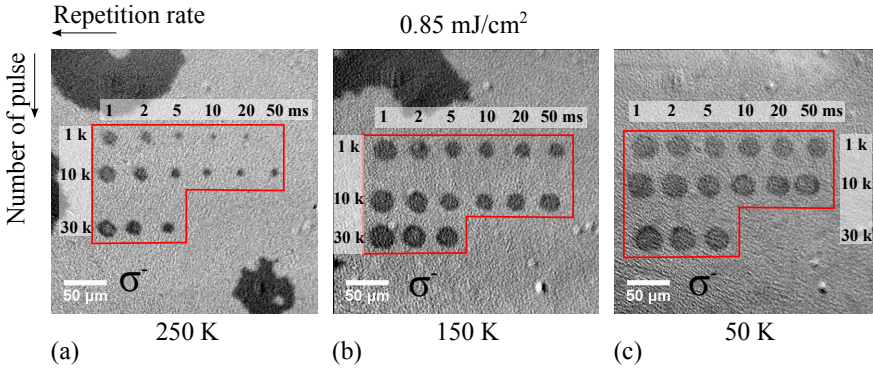


Figure 6.13: Kerr microscopy images of a  $[\text{Co/Pt}]_3$  multilayer at three different temperatures of (a) 250 K, (b) 150 K, and (c) 50 K. The laser repetition rate was varied from 1 to 0.02 kHz (corresponding pulse-to-pulse time intervals of 1 to 50 ms) in the horizontal direction. In addition, the number of pulses was kept constant in horizontal direction, but was varied along vertical direction from  $10^3$  to  $3 \times 10^4$ .

At 250 K (Figure 6.13 (a)), we observe a clear decrease of the optically induced spot diameter when tuning the laser pulse train towards lower repetition rates. In the extreme case, at  $10^3$  pulses with 50 ms pulse-to-pulse time interval (the top right

position in (a)), the optically induced domains did not form at all or their size was below the resolution limit. Since the average power, number of pulses, and the light polarization for every illuminated spot along the horizontal direction were kept constant, we associate the observed changes with the relaxation process as happening on the millisecond timescale.

Contrary to the measurement at 250 K, at lower temperatures, we first observe that all optically induced spots are nearly equal in size (particularly at 50 K) regardless of the laser repetition rate. In addition, the diameters of the spots illuminated at lower temperatures are much larger than the spots illuminated at higher temperatures, despite the fact that laser repetition rate and number of pulses per illuminated spot are the same. These observations are in contrast to the general expectation that a lower temperature reached by the laser pulses should lead to a less efficient AOS/AODF and therefore should result in smaller spot sizes. These counter-intuitive results indicate that the variation of the *ambient* temperature of the sample plays a minor role in the process of domain formation, although it decisively influences the *relaxation* process after the fs pulse illumination. These relaxation processes are obviously more efficient at higher ambient temperature.

### 6.2.1 Heat assisted magnetic recording

Apart from studying the all-optical switching phenomena, we examined also the heat assisted magnetic recording effect. In this case, the  $[\text{Co/Pt}]_3$  multilayer was illuminated with a circularly polarized fs-laser beam at fixed fluence, and was moved at 30

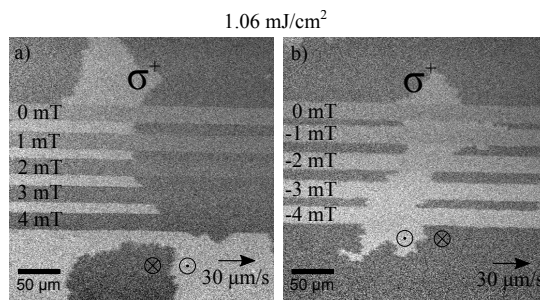


Figure 6.14: Demonstration of heat assisted magnetic recording in Co/Pt multilayers. The sample was illuminated with a circularly polarized ( $\sigma^+$ ) fs-laser beam at 30  $\mu\text{m/s}$  sample sweeping velocity. During laser illumination, an external magnetic field applied from 0 mT to a) 4 mT and b) -4 mT. The magnetic contrast of the laser illuminated lines gradually increases with increasing magnetic field and the magnetization completely saturates at  $\pm 4$  mT.

$\mu\text{m/s}$ , which was previously shown to be way above the optimum for AOS, i.e. no AOS is expected at this sweeping speed. During laser illumination, an external magnetic field was applied using an electromagnet. The magnetic field was gradually increased up to  $\pm 4$  mT from top to the bottom, as shown in Figure 6.14. The magnetic contrast of the laser illuminated horizontal lines is increased as the strength of applied field rises. We observe a saturation of the magnetization, namely full switching under  $\pm 4$  mT applied field. Considering the fact that the  $[\text{Co/Pt}]_3$  multilayer has a coercive field ( $H_C$ ) of 45 mT, optically-induced heating makes it possible to switch the sample with only 10% of  $H_C$ .

### 6.3 Discussion

In this section, we first discuss the results of optically induced magnetization reversal experiments from a quasi-static perspective. Then we explain the mechanisms of AOS and AODF effects from a domain wall dynamics point of view.

#### 6.3.1 Laser intensity threshold for AOS

In the earliest phase of the experiments, we determined the optimum laser fluence and number of pulses. The laser fluence dependence of the AOS experiments pointed to the existence of a threshold, above which laser pulses can reverse the magnetization of thin films. However, AOS does not take place at a sharply defined laser fluence. Instead, it is observed within a narrow range of laser intensities. It is broadly assumed that this range corresponds to a narrow range of temperatures, where the upper limit of this temperature range is related to the Curie temperature ( $T_C$ ) and the lower limit to the ‘AOS’ threshold. Above the  $T_C$  threshold, the sample is overheated, and upon cooling, it relaxes into an assembly of small domains. Below the ‘AOS’ threshold, on the other hand, the domain structure exhibits no change. These thresholds are illustrated for two different laser fluences in Figure 6.15.

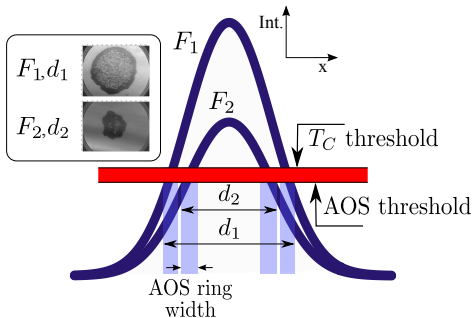


Figure 6.15: 2D schematics of a Gaussian laser intensity profile for different fluences  $F_1$  and  $F_2$  that gives rise to AOS only in ring-like areas (light blue), where the local laser fluence is between upper ( $T_C$ ) and lower (AOS) thresholds (red band).

The width of the switched lines in Figure 6.2 as well as the width of ‘AOS rings’ shown in Figure 6.10 are defined by the overlap between the threshold lines and the laser fluence in agreement with a Gaussian intensity profile. We note that the ring-like switching is due to the 3D projection of the overlapping zones which are depicted by the light blue bars in the figure above.

As the importance of  $T_C$  in AOS was already highlighted, the hypothesis was further supported by varying  $T_C$  of the multilayers by changing their bilayer repetition numbers ( $N$ ) (see Figure 6.12). In this experiment, the widths of the written lines were intentionally kept the same in order to determine the minimum laser fluence  $F_{min}$  needed for the onset of switching domains. The effect of  $T_C$  for different bilayer repetitions is illustrated in Figure 6.16. The larger  $F_{min}$  required for larger  $N$  is attributed to the increased thresholds due to the enhanced Curie temperature of the multilayer.

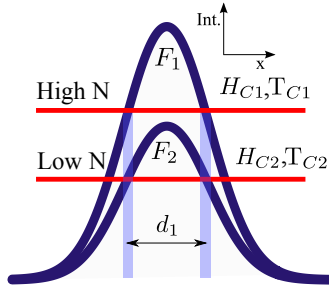


Figure 6.16: 2D schematics of the Gaussian intensity profiles for different laser fluences that resulted in the same width (light blue) in multilayers with different  $N$ .

We note that this technique does not exclusively test the effect of  $T_C$ , since the increased number of bilayers will also change  $H_C$  and the optical coefficients. We further investigated the effect of  $H_C$  within the experiments shown in Figure 6.13. The results will be discussed below. More importantly, the increased thickness of samples and number of interfaces led us to consider the role of the optical coefficients, e.g., absorption processes which may significantly affect the required fluence. Therefore, we calculated the reflectance ( $R$ ), transmittance ( $T$ ) and absorptance ( $A$ ) profiles of  $\text{Pt}(20\text{\AA})/[\text{Co}(4\text{\AA})/\text{Pt}(\text{\AA})]_N$  structures as a function of bilayer repetition  $N$  using the IMD simulation software package [235]. The profiles are shown in Figure 6.17 and the corresponding data are given in Table 6.1

In the experiments mentioned above, we used laser fluences of 0.82, 1.13 and 1.41  $\text{mJ}/\text{cm}^2$  for  $N=3$ , 5 and 7, respectively. That amounts to an increase of fluence about 38% between  $N=3$  and  $N=5$ , and 25% between  $N=5$  and  $N=7$ . On the other hand, according to the simulation, 38% of the beam intensity is transmitted through the 3rd bilayer, whereas 28% is transmitted to the 5th bilayer. This indicates a loss of intensity of 10% between the 3rd and 5th bilayer, and 7% between 5th and 7th

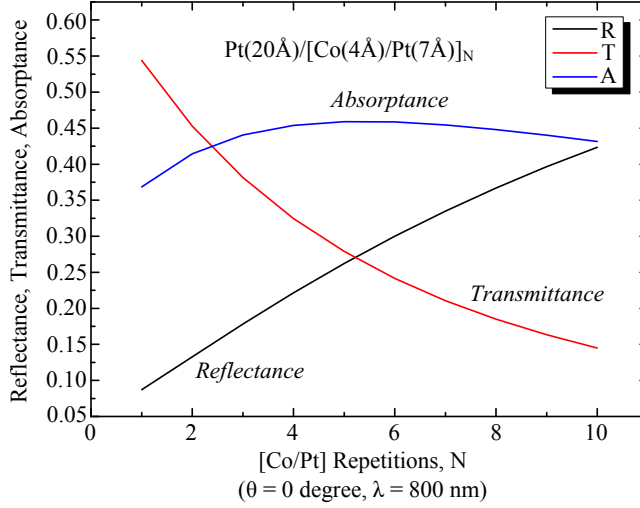


Figure 6.17: Simulation of reflectance (R), transmittance (T) and absorptance (A) coefficients for varying bilayer repetitions of  $[\text{Co/Pt}]_N$  multilayers.

Table 6.1: Reflectance, transmittance and absorptance ratios calculated using IMD software. The loss of intensity (transmittance) is 10% between 3rd and 5th bilayers, and 7% between 5th and 7th bilayers.

Repetition	Reflectance	Transmittance	Absorptance
N=3	18%	38%	44%
N=5	26%	28%	46%
N=7	33.5%	21%	45.5%

bilayers. Comparing the increase and the loss of laser intensity, it is clear that we do not only compensate the missing intensity due to absorption, but we also compensate the increased Curie temperature of the samples with higher bilayer repetition.

### 6.3.2 Domain wall dynamics model

In the quasi-dynamical domain formation and relaxation experiments (shown in Figure 6.13), the non-equilibrium sample temperature was controlled by tuning the time interval between the consecutive laser pulses. As a consequence, a continuous drop in the spot diameter was observed when the system was allowed to dissipate the thermal energy from the illuminated area for a longer time. We ascribe this process to a thermal gradient driven domain wall motion from the cooler areas towards the hotter areas of the sample, as supported by a number of experimental and theoretical studies. Immediately after the random domain formation with the first single pulse, DWs start drifting towards the spot center keeping in mind that the decaying temperature

follows the Gaussian intensity profile imprinted by laser beam. As a result, the larger time interval between the pulses results in formation of smaller spots, in agreement with the experimental observations. The time interval between the pulses allows a rough estimate of the DW speed: assuming that the laser induced spot of  $\sim 15 \mu\text{m}$  radius (Figure 6.13(c) top right) can collapse within 50 ms pulse-to-pulse time interval (Figure 6.13(a) top right), the domain wall velocity is estimated to be of the order of  $3 \times 10^{-4}$  m/s. We note that it is an indirect estimate of the *minimum* DW velocity, because in fact, the DW velocity could be much higher, especially initially when the thermal gradient is the strongest. It is important to discuss the driving forces that make the domain walls move to the center and even force domains to completely collapse in the absence of applied magnetic field. There is a number of mechanisms that have been proposed and some of them are briefly revisited below.

The effects of a thermal gradient on the domain wall motion were treated in different aspects. Schlickeiser *et al.* modeled the DW motion considering thermodynamic principles, mainly the maximization of entropy [236]. The so-called entropic torque pushes the DWs towards the hotter region [236, 237]. According to Hinzke *et al.*, the DW motion is induced via magnonic spin currents due to the spin-Seebeck effect (SSE) [238]. While the magnons travel from the hotter into the cooler regions, however, the conservation of angular momentum drags the DW into the hotter regions [238]. Besides the theory, a number of experimental results support the mechanism of DW motion towards hotter regions [161, 239].

In addition to thermal effects, several studies predict small and bubble-like domains to collapse under a pure magnetostatic tension. Mansuripur used computer simulations to study the relaxation dynamics of domain nuclei [90]. Once the nuclei have formed in an applied field, domains were left to relax under the pressure of the wall energy and the forces of demagnetization in the absence of the field. Consequently, the larger nuclei merge and they push the smaller ones towards collapse. Moon *et al.*, in addition, showed the domain walls to exhibit an elastic nature that minimizes the DW length, because of finite DW energy density  $\sigma_w$ . The range of the elastic tension effect can reach up to  $20 \mu\text{m}$  from the nucleation center [240].

In our experiments, a striking observation was made when the samples were illuminated by laser at low temperatures. Cooling the sample below room temperature results in a drop of the *ambient* temperature and the rise of the sample coercivity  $H_C$ . One can therefore expect that a *larger* laser fluence would be required in order to reach the domain formation threshold that scales with  $T_C$  ( $H_C$ ), of the sample in accordance with the schematics sketched in Figure 6.16. Contrary to this expectation,



however, the optically induced spots at low temperatures are much larger compared to the spots illuminated at 250 K. At the same time, our experiments at low temperatures show that all the spots appear to have the same size regardless of the pulse-to-pulse interval. This observation is in agreement with the above-discussed mechanism of the thermal gradient induced DW motion towards the hot spot center. We assume that the DW motion that proceeds via DW creep from one pinning center to another, as introduced in [Subsection 2.5.2.2](#). If the ratio between the activation energy to overcome the energy barrier of a pinning center and the thermal energy,  $\Delta E/k_B T$ , increases at low temperatures, the thermal gradient driven DW motion stops, thus preventing the collapse of the optically induced spots and consequently results in larger spots.

### 6.3.3 Role of laser pulse accumulation<sup>4</sup>

The accumulation of pulses has a two-fold effect on the illuminated spot. First, the ‘AOS-ring’ is formed, second, its radius is increased. The latter is basically attributed to the 2D heat diffusion process as formulated in [Equation 3.3](#). Here, we focus on the question why the accumulation of pulses is needed for an efficient all-optical switching.

As the first fs laser pulse impinges on the film surface, the magnetization spontaneously breaks into domains of various size. This happens in pico- to nano-second time scale. The laser pulse also leads on, a slower time scale, to an increase of the temperature by  $T_P$ , which then exponentially decays due to thermal dissipation with a time constant  $t_0$ :

$$T(t) = T_{ambient} + T_P \exp\left(-\frac{t}{t_0}\right) \quad (6.2)$$

Temperature-gradient or magnetostatically induced driving forces give rise to a shrinking of the spot radius. The actual domain wall motion proceeds in steps from pinning center to pinning center. We are interested in the number of jumps that occur in a given time interval  $\tau$  that can be the pulse-to-pulse time interval  $\Delta t$  in the case of a pulse train or  $\tau = \infty$  for the cases of a single pulse or the last pulse of a pulse train. The number of jumps  $n(\tau)$  in time  $\tau$  is given by

$$n(\tau) = \int_0^\tau p(t) dt \quad (6.3)$$

where  $p(t)$  is the rate of the jumps scaling with  $\exp(-\Delta E/kT(t))$ . The amount of collapse of the illuminated area is given by  $n(\tau)\Delta R$ , where  $\Delta R$  is the average distance of a single domain wall jump. A dependence of  $n(\tau)$  on both  $\tau$  and  $T$  is a general result and holds for a variable temperature  $T(t)$ . [Figure 6.18](#) shows the dependence

<sup>4</sup>PD. Dr. Daniel Bürgler is greatly appreciated for the simulations presented in this subsection.

of  $n$  as a function of the sample temperature  $T_{sample}$  and the time interval  $\tau$ . The simulation is performed with the parameters such that the experimental observations in Figure 6.13 are reproduced.

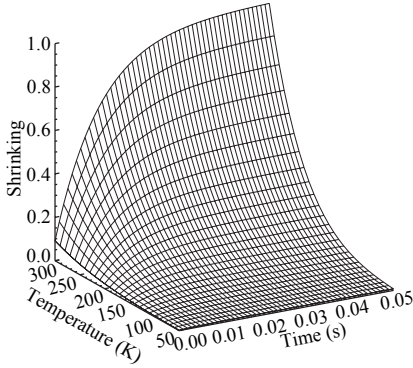


Figure 6.18: Number of domain wall jumps from one pinning center to another as a function of pinning temperature and time. The simulation parameters were adjusted to reproduce the experimental observations.

The simulation results to an activation energy of  $\Delta E \approx 0.86eV$ , which is a reasonable order of magnitude. However, the model does not account for the influence of the number of pulses on the growth of the ‘AOS-ring’ and stabilization of the illuminated spot. The formation of the AOS-ring can be incorporated to a MCD-driven helicity-dependent domain growth mechanism. As the number of pulse increases, magnetic domains selectively grow at the perimeter of the spot and increase the domain wall length. Consequently, more pinning centers are encountered for a given domain wall and it becomes more resistant to move towards the spot centre. The evolution of spot size and the ‘AOS-ring’ as a function number of pulses is shown in Figure 6.19.

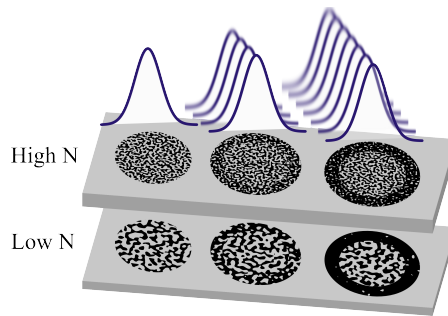


Figure 6.19: Schematics of domain sizes in multilayers with high  $N$  (upper row) and low  $N$  (lower row). Larger  $N$  multilayers have smaller ground-state domain sizes due to an increased dipolar field. The preferential growth of ‘black’ domains is illustrated as a function the number of circularly polarized laser pulses. Domain growth takes place at the perimeter where the optimum AOS fluence condition is met.

In order to describe the growth of the optically-induced magnetic spots, as well as,

the diameter of the surrounding ‘AOS-ring’, with an increased temperature due to the accumulation of a large number of laser pulses, we use the phrase ‘radial propagation of the thermal gradient’. The effect is schematically shown in Figure 6.20. The Gaussian shapes here represent the heat provided by the pulses, instead of the laser fluence.

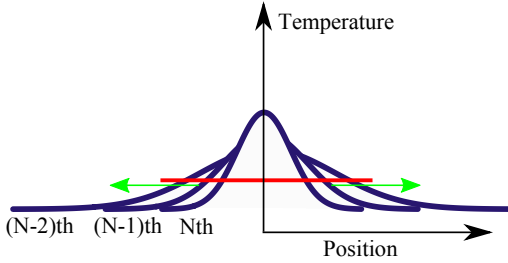


Figure 6.20: Radial propagation of the thermal gradient. We note that the Gaussian shapes represent the *heat distribution* in lateral dimensions associated with subsequent laser pulses. The red line depicts the temperature threshold for AOS. As the heat dissipated, the intersection moves radially along the green arrows.

When  $N$  pulses impinge on the sample surface, the heat associated with these pulses accumulates and creates a slowly rising background temperature. Due to this, heat is propagating radially from the illumination center. The intersection where AOS threshold (red line) and the sample temperature (Gaussians) met shifts outwards resulting in larger ‘AOS ring’.

### 6.3.4 General overview of AOS by domain wall motion

Based on the above arguments, we propose a physical model involving three inter-linked mechanisms: optically induced equilibrium heating, magnetic circular dichroism (MCD), and the thermal gradient driven DW motion. In our model, the laser pulse first heats up the magnetic system which, upon cooling down, causes initially a random domain formation with equally distributed ‘up’ and ‘down’ domains. Subsequent pulses further heat the system what results in a thermal gradient extending radially away from the hottest area at the center of the illuminated spot. A constant supply of heat maintains the AODF at the center of the spot. On the other hand, AOS forms at the perimeter of the illuminated area where the laser fluence at this part allows a MCD-driven helicity-dependent domain growth, see Figure 6.19. In addition to the domain growth, domain walls experience a drift towards the center, which in turn leads to a collapse of the illuminated spots. We assume that the DW drift velocity depends on the domain size and is less efficient for the larger domains, because of the increased possibility of encountering more pinning centers. As the number of pulses impinging at the specific spot increases, the MCD-driven AOS regions are forming and the thermal gradient flattens due to the lateral heat propagation. These evolving processes result in a magnetic stabilization of the illuminated area due to the stronger

pinning (larger domain walls) and smaller driving force (weaker thermal gradient).

The experimental results that we obtained on the bilayer repetition dependence of AOS/AODF (presented in Figure 6.12) can be also better explained using the above physical picture. We recall that we observed a lower normalized domain contrast  $p$  in larger bilayer repetitions (larger  $N$ ) despite the fact that we illuminated the samples with minimum required laser fluence to manipulate the magnetizations. The sample with larger intrinsic domains (as in [Co/Pt]<sub>3</sub> multilayer) displays higher switching probability. In other words, larger domains in lower  $N$  multilayers that are formed by the first laser pulses can merge easier by the statistical process, while smaller domains in higher  $N$  multilayers can collapse faster leading to incomplete switching for the same number of pulses. As discussed above, in case of circularly polarized pulses, the domain growth is ascribed to the MCD effect. This accumulative process is enhanced with a number of pulses, until the switched domains merge together to yield a complete switching.

To complete the physical picture, we interpret our above-described results in a perspective of domain wall dynamics. We observed incomplete all-optical switching with increasing laser fluence in the scanned lines (Figure 6.2). However, laser-induced magnetic domains are formed depending on the beam helicity. This is attributed to the incomplete domain growth, because of the excessive heat transferred into the multilayer system.

## 6.4 Conclusions

Our analysis shows that the optically induced all-optical magnetization switching in [Co/Pt] <sub>$N$</sub>  multilayers is a consequence of multiple pulse accumulation, and it involves material heating, magnetic circular dichroism, as well as the thermal gradient driven domain wall motion mechanisms. In our physical picture, first, the laser pulse heats up the material, thus causing a randomly distributed multidomain state. Optically induced magnetic domains, driven by a strong thermal gradient, move towards the spot center. The subsequent laser pulses at an optimum intensity level provide thermal energy for helicity-dependent domain growth due to the broken magnetic symmetry via magnetic circular dichroism. Nevertheless, the role of the inverse Faraday effect as a contribution to the symmetry breaking of the switching process requires further investigation. The process of growth and collapse of optically induced domains is finally stopped due to the domain wall pinning and thermal gradient flattening.

The all-optical switching (AOS) efficiency is expected to be higher for materials with

larger domains, since the individual domains can merge and become more resistant against the collapse under the thermal gradient. This argument is supported by the AOS experiments on the multilayers, where the sample coercivity, Curie temperature and the domain size are tuned. In all samples, as the number of pulses impinging at the specific spot on the sample increases, the thermal gradient flattens due to lateral heat propagation and leads to a stabilized magnetic domain state due to the stronger pinning and smaller driving force.

The above physical picture points to the importance of the domain relaxation dynamics and the material properties affecting the magnetic domain size. We expect that the analysis will contribute to the understanding of the laser-induced switching process and the further optimization of the optically switchable magnetic materials.

# Chapter 7

## Domain wall drift driven by laser pulses

In this chapter we demonstrate that magnetic domain walls can be manipulated with femtosecond laser illumination. We present the XMCD-PEEM images showing domain wall drift upon moving a laser beam along the surface. A quantitative analysis is performed to calculate the elongation of domains.

### 7.1 Introduction

Manipulation of the magnetic domain wall (DW) displacement has been considered as an important phenomenon for memory applications [241]. For a review of domain-wall based memory devices, the reader is referred to Ref. [242]. Besides memory devices, a displacement of DWs has already been proposed as a method to be used in artificial learning in neural networks [243]. Therefore, control of the DW motion attracts growing interest. A temperature gradient is one of the driving forces for DW motion [236, 237, 244]. Laser beams provide an appropriate thermal gradient on illuminated surfaces in accordance to their intensity profiles.

The current literature on all-optical switching of *ferrimagnetic* materials points to a domain wall drift (DWD) driven by a series of laser pulses [239, 245, 246]. This phenomenon was also confirmed in our experiments on GdFeCo test samples as shown in [Figure 7.1](#). In this work, we were motivated by observing the DWD effect in Co/Pt multilayers in accordance to a thermal gradient generated by moving laser beams.

### 7.2 Results and analysis

Unlike *ferrimagnetic* GdFeCo layers, we observed no domain wall drift in Kerr microscopy images of *ferromagnetic* Co/Pt layers as presented in [Chapter 6](#) in detail. Nevertheless, XMCD-PEEM images of the illuminated areas of the sample allowed

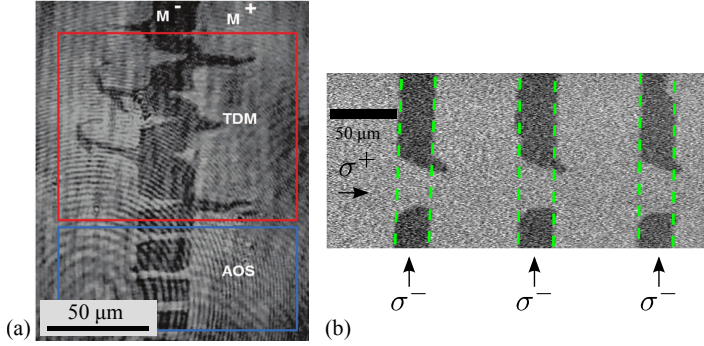


Figure 7.1: Domain wall drift (DWD) in ferrimagnetic layers imaged with magneto-optical microscopy. (a)  $\text{Tb}_{70}\text{Fe}_{30}$  alloy example from Hassdenteufel *et al.* [246]. Laser beam was swept across the magnetic domain in a zigzag-like pattern. Inside the blue box, a circularly polarized beam switched the black domain into a white domain. On the other hand, a linearly polarized beam gives rise to DWD inside the red box. (b) Kerr microscopy image of our  $\text{Gd}_{22}\text{Fe}_{70}\text{Co}_8$  test sample first illuminated vertically with  $\sigma^-$  polarization. The borders of the resulting black domains are depicted with green dashed lines. Then, the laser beam with  $\sigma^+$  polarization was swept horizontally over the existing domains. Opposite helicity caused not only switching of the domains, but also DWD in the black domains along the propagation direction at the crossing point.

larger magnification and gave the first indication of DWD. In Figure 7.2, optically induced magnetic domains were produced by sweeping the laser beam at constant fluence ( $0.71 \text{ mJ/cm}^2$ ) and different polarizations. First, we swept a circularly polarized ( $\sigma^+$ ) laser beam horizontally across the magnetic surface, then  $\sigma^-$ ,  $\pi$  and  $\sigma^+$  polarized beams were swept vertically. At the intersection point there is a clear evidence of DWD along the laser beam sweeping direction for opposite helicities.

At a fluence of  $0.71 \text{ mJ/cm}^2$ , sweeping the laser beam results in a complete AOS. In other words, there is no sub-domain structure observed along or across the switched lines. We were motivated to find out how the domains follow the thermal gradient, which is formed by the moving beam. Therefore, the laser fluence was increased up to  $1.06 \text{ mJ/cm}^2$  in order to form smaller domains due to uncompleted AOS. The crossed domain structures shown in Figure 7.3 were created using the procedure described above.

In Figure 7.3, we observe elongation and partial alignment of domains along the beam sweeping direction. In order to describe our observation quantitatively, we performed an analysis on the binarized images. In this process, the images in the red frames were first cropped, and then binarized using *ImageJ* software. In the next

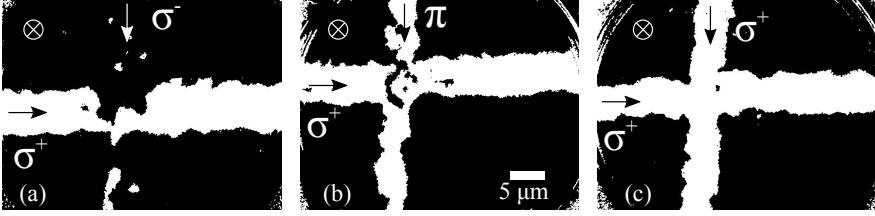


Figure 7.2: XMCD-PEEM images (binarized) of magnetic domain crosses created after laser illumination using different beam polarizations. First, the horizontal lines were made using a  $\sigma^+$  polarized beam, then these lines were crossed vertically using different polarizations.

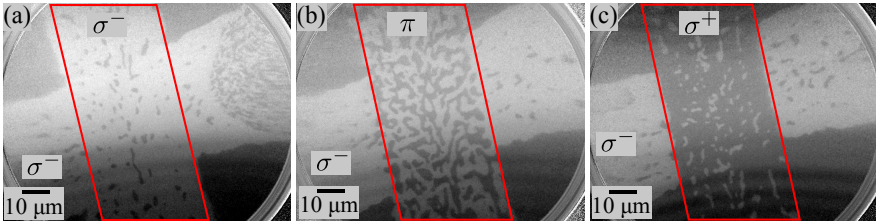


Figure 7.3: XMCD-PEEM images showing magnetic domain structure at the intersection of two lines created by sweeping of laser beam with given polarizations. Domains created with  $\sigma^-$  polarized beam were crossed with (a)  $\sigma^-$ , (b)  $\pi$  and (c)  $\sigma^+$  polarized beams. Laser fluence of  $1.06 \text{ mJ/cm}^2$  allowed formation of smaller domains due to slight over-heating of illuminated area.

step, the images were binned as lines both vertically and horizontally, then the domain lengths were calculated along and across the lines. Figure 7.4 shows the histogram of domain lengths in pixels<sup>1</sup>. In other words, the frequency of white and black domain lengths were calculated for each line in both horizontal and vertical directions. The statistical elongation ( $\epsilon$ ) is calculated using the mean domain lengths for both type of domains (white and black) and for both directions.

The results of the analysis (Figure 7.4) shows an asymmetry in mean the domain length of the black domains in (a)  $\sigma^-$  (23%) and white domains in (c)  $\sigma^+$  (15%), which points to an elongation in the laser beam sweeping direction. This elongation is further quantified for individual domains in terms of the *aspect ratio* with the help of *ImageJ* software package. Figure 7.5 shows the aspect ratio of the domains as a function of their horizontal position in the cropped images. Domains with larger aspect ratios are aggregated at the center of the image, where the laser beam has a larger intensity.

<sup>1</sup>Dr. Slavomír Nemšák is greatly appreciated for his contribution to the analysis



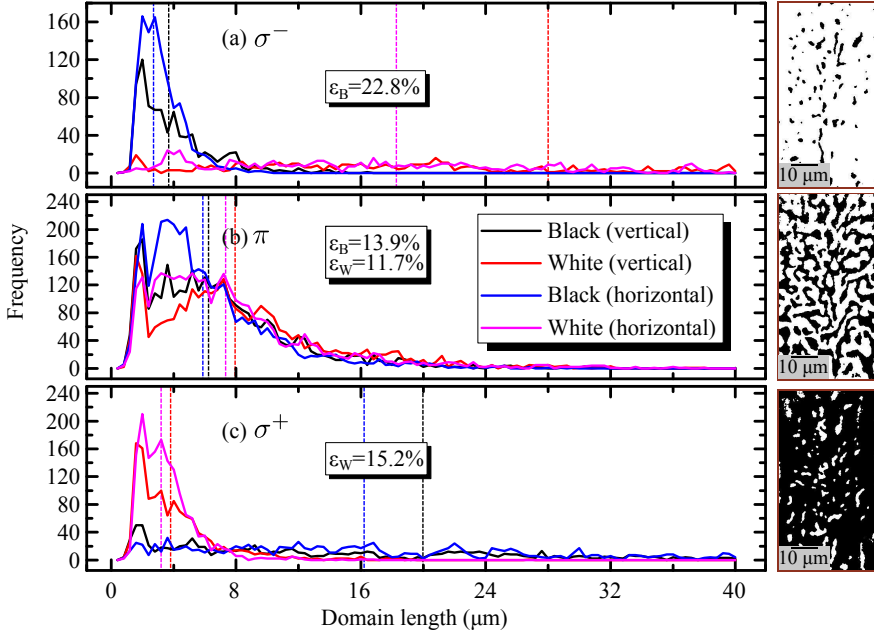


Figure 7.4: Histogram of the lengths of white and black domains in vertical and horizontal directions. The calculation was made over the cropped areas given at the right side of each graph. The mean domain lengths are depicted by dashed lines. The statistical elongation of domains is calculated using the mean domain lengths and given as  $\varepsilon_B$  and  $\varepsilon_W$  for black and white domains, respectively.

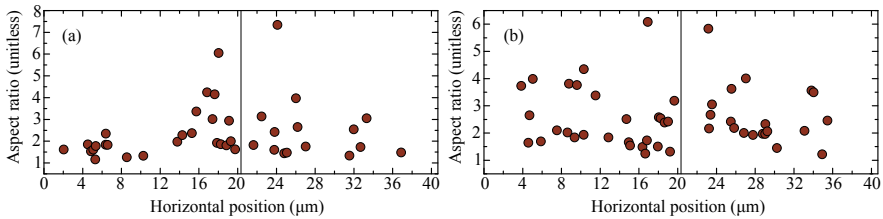


Figure 7.5: Aspect ratios of individual domains as a function of the horizontal position. (a) black domains after  $\sigma^-$  and (b) white domains after  $\sigma^+$  polarized laser beam. Domains with larger aspect ratios are aggregated at the center of the image where the laser has larger intensity.

### 7.3 Discussion and conclusion

In Chapter 6, we investigated the domain formation as a consequence of the laser illumination in a fixed lateral position, and proposed a model based on laser-induced thermal gradients. With the quantitative analysis presented in this chapter, we now

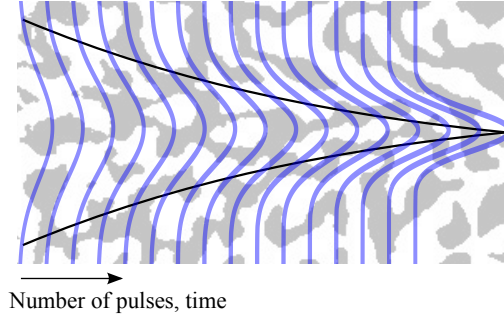


Figure 7.6: Illustration of a thermal gradient induced by a laser beam moving from left to right. The Gaussian profiles denote the heat transferred to the material by the consecutive pulses. The heat dissipates inside the material and generates an overall thermal gradient (black curves) between the left and right parts of the illuminated area. The domain alignment (shown in background) qualitatively agrees with the direction of the thermal gradient.

demonstrate a domain alignment by sweeping the laser beam. Furthermore, we also observe an alignment of domains towards the laser spot center. The orientation of the laser-induced domains can be ascribed to a moving thermal gradient. A thermal gradient generated by the sequence of laser pulses is illustrated in Figure 7.6. Considering the cooling time of the heated area, we calculated the typical time  $t$  for a region of size  $L$  to reach thermal equilibrium using the  $t \approx L^2/D$  approximation, where  $D$  is the heat diffusion term for in two-dimensions. The timescale of the heat diffusion is comparable to 1 ms, which is the time interval between consecutive laser pulses.

In order to describe the thermal gradient-induced DW motion, several models are proposed in the literature. It is widely accepted that DWs move in a thermal gradient towards the hotter area on the sample surface. Microscopically, this is attributed to magnons, which exert an adiabatic spin transfer torque (STT) on the DWs [247]. As a result of STT, domain walls are driven opposite to the propagation direction of the magnons, which are generated thermally [238, 248]. An alternative approach to DW motion is based on thermodynamical arguments. As the free energy of the wall decreases at higher temperatures, entropy and minimization of the energy act as a driving force to move domains towards the hotter regions [236].



# Chapter 8

## Ultrafast demagnetization dynamics of $[\text{Co}/\text{Pt}]_3$ multilayer - An outlook

In this chapter we present preliminary results showing the ultrafast demagnetization dynamics of  $[\text{Co}/\text{Pt}]_3$  multilayers. We optically pumped the samples using a linearly polarized laser beam and varied the laser fluence and the strength of the applied magnetic field. The fitting to the obtained curves revealed characteristic timescales of the ultrafast demagnetization and relaxation processes and served as a basis for further dedicated experimental investigation including circularly polarized light.

### 8.1 Introduction

The ultrafast demagnetization dynamics of Co/Pt multilayers has been investigated earlier by several groups [249–251]. After the discovery of AOS, the early magnetization dynamics (first few picoseconds) gained importance due to the attempts to achieve single pulse all-optical switching. Currently, it is widely accepted that AOS in ferromagnetic multilayers requires multiple laser pulses, although, the question on the origin of the deterministic magnetization reversal by means of circularly polarized pulses remains open.

Here, we investigate ultrafast demagnetization curves as a function of the laser fluence and applied magnetic field. The femtosecond laser system and the pump-probe setup used in this work have been introduced in [Chapter 5](#).

Within the period of this PhD project, preliminary results were obtained for linearly polarized pump pulses. A detailed investigation for the helicity-dependence of demagnetization curve under static and pulsed magnetic fields is particularly interesting, and is the subject of the follow-up PhD project.

## 8.2 Results

Ultrafast demagnetization curves were measured using the time-resolved MOKE setup sketched in Figure 5.5. The magnetic field was applied in either of two directions perpendicular to the film plane in order to record the demagnetization signal free of other optical contributions. Then, the traces were subtracted for eliminating the non-magnetic contributions. In order to increase the signal-to-noise ratio, each curve was measured for 3 to 6 cycles.

### 8.2.1 Laser fluence dependence

We first compare the demagnetization curves of the  $[\text{Co}/\text{Pt}]_3$  multilayer for different pump beam fluences under constant magnetic field. The laser fluence steps were chosen such that we could observe the transients from partial demagnetization to a full demagnetization. The pump beam was linearly polarized in p-plane. The magnetic field was set to  $\pm 85$  mT which is above the coercive field of the sample and was applied perpendicular to the surface. The normalized curves are presented in Figure 8.1.

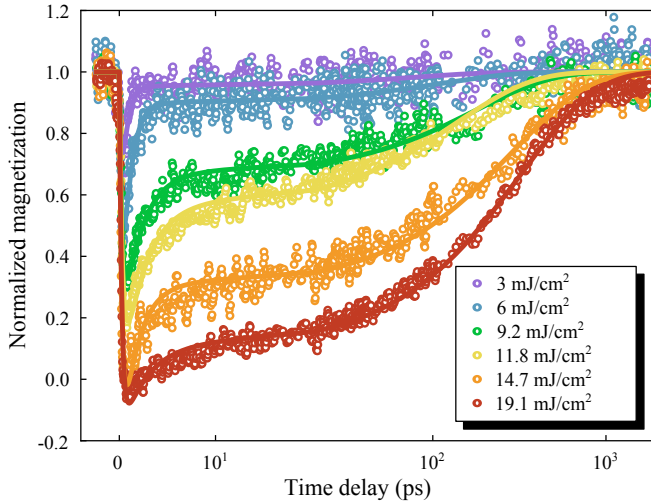


Figure 8.1: Ultrafast demagnetization curves of  $[\text{Co}/\text{Pt}]_3$  multilayer for varying laser pump beam fluences on a logarithmic scale. The pump beam polarization was linear and parallel to the plane. During the measurement, a continuous magnetic field of  $\pm 85$  mT was applied. The solid lines represent the fitting function based on three temperature model (3TM) (Equation 3.8).

The dynamic response of magnetization exhibits an ultrafast quenching with a demagnetization time  $\tau_M$  below 1 ps, which is followed by a relatively slow recovery within

0.1-1.2 ns depending on the excitation fluence. In order to estimate these characteristic timescales, the demagnetization curves were modeled using the function presented in Equation 3.8 (neglecting the convolution term). The time constants  $\tau_M$ ,  $\tau_E$  and  $\tau_R$ , coefficients  $A_1$  and  $A_2$  are the fitting parameters, which are extracted from the simulation. In addition to these parameters, the zero delay position  $t_0$  is determined by fitting. The characteristic timescales and amount of magnetization quenching are plotted in Figure 8.2.

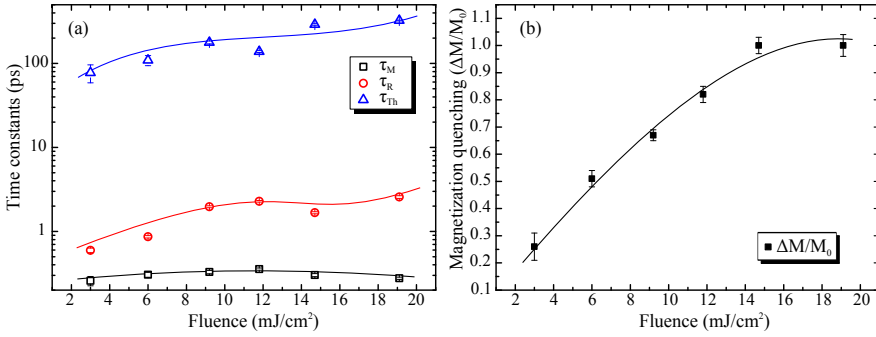


Figure 8.2: Time constants of the demagnetization curves (a) and magnetization quenching (b) as a function of pump beam fluence. The lines are guides to the eye.

Using the Equation 3.8 (including the convolution term), the parameters did not converge to meaningful values. Due to that, the amplitude, center and FWHM parameters of the Gaussian function were added to the above-mentioned six parameters. In order to reduce the number of parameters, we used a modified function for the first picoseconds of the curve.

$$\frac{\Delta M(t)}{M_0} = G(t) \otimes H(t) \left[ A_1 \left( 1 - e^{-\frac{-(t-t_0)}{\tau_M}} \right) e^{-\frac{-(t-t_0)}{\tau_E}} \right] \quad (8.1)$$

Equation 8.1 allows a better fitting around the zero delay and results in slightly changed demagnetization times. The fitting results and comparison of the demagnetization times are given in Figure 8.3.

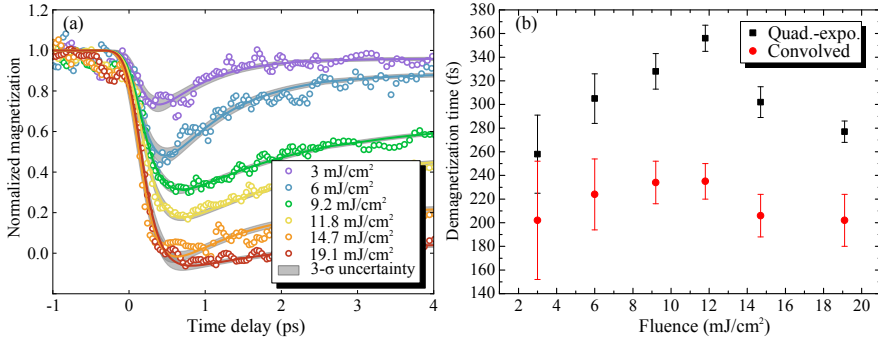


Figure 8.3: Curve fitting comparison with and without convolution. (a) Fitting curves using the bi-exponential function convolved with a Gaussian representing the instrumental time resolution. (b) Comparison of demagnetization time  $\tau_M$  for quadri-exponential function and Gaussian-convolved bi-exponential function.

### 8.2.2 Magnetic field dependence

During these measurements, we have kept the laser fluence constant at  $19 \text{ mJ}/\text{cm}^2$ , and varied the magnetic field in six different steps below and above the coercive field of  $[\text{Co}/\text{Pt}]_3$  multilayer. The obtained data are plotted in Figure 8.4. The curves are simulated using the Equation 3.8 excluding convolution.

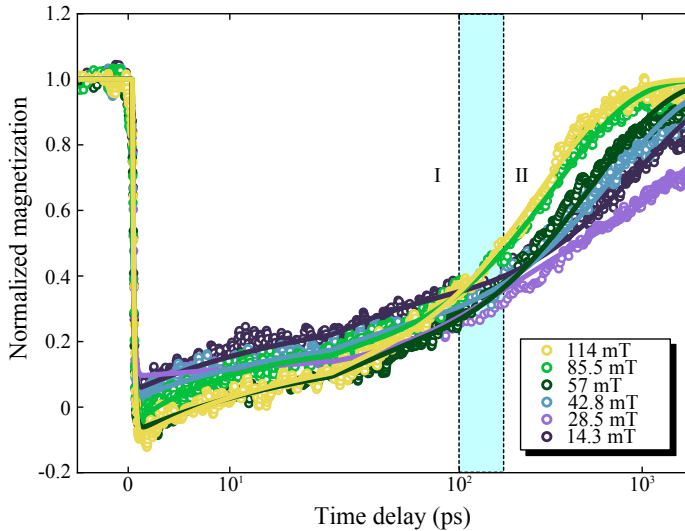


Figure 8.4: Ultrafast demagnetization curves of  $[\text{Co}/\text{Pt}]_3$  multilayer for varying magnetic field strength. For a better visibility, we plotted x-axis in a logarithmic scale. The shaded area, starting at 100 ps time delay, separates two regimes of magnetization relaxation processes.

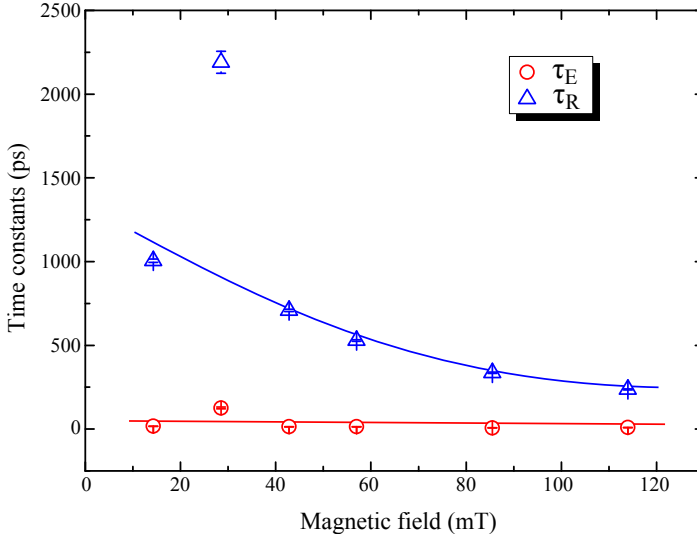


Figure 8.5: Magnetization relaxation time constants as a function of the applied magnetic field. The lines are guides to the eye.

We calculated the magnetization relaxation times  $\tau_E$  and  $\tau_R$  for two regimes depicted by I and II, respectively in Figure 8.4. The calculated time constants are presented in Figure 8.5.

### 8.3 Discussion

We measured ultrafast demagnetization curves using time-resolved MOKE setup in polar geometry. In the first part of the study, we fixed the applied magnetic field and varied laser beam fluence. Under this conditions, demagnetization takes place within approximately 300 fs, which is very typical for transition metals as well as their alloys and multilayers. The demagnetization time does not exhibit a considerable tendency on varying the pump beam fluence. In particular, the simulation of the first 4 ps of the curves using convolution (see Figure 8.3(b)) shows that the  $\tau_M$  values do not vary as a function of fluence. The ultrafast recovery time  $\tau_E$  scales with the amount of quenching which monotonically increases with increasing fluence. The long-term recovery time  $\tau_R$  is two orders of magnitude larger than  $\tau_E$ . The magnetization recovery occurs at  $\sim 1$  ns for the highest excitation fluence. The faster recovery time is attributed to the spin flip scattering in the reverse direction to those give rise to demagnetization.

In the second part of the study, we investigated the effect of the applied magnetic field, while the laser fluence is constant at  $19 \text{ mJ/cm}^2$ . According to the results of



fitting, the demagnetization time  $\tau_M$  is found to be around  $151 \pm 23$  fs, and does not change as a function of the applied field. As clearly seen in [Figure 8.4](#), magnetization relaxation takes place in two regimes.

In regime I, we observe a small magnetic field dependence on the magnetization quenching. The larger the applied field gives rise to more quenching of the magnetization in spite of the fixed laser fluence. On the other hand, we do not observe a measurable variation in  $\tau_E$ , (see [Figure 8.5](#)). This is a timescale in which the electrons are still hot and their energy dominates over the Zeeman energy. However, for long relaxation times (regime II), the magnetic field is more dominant and affects significantly the relaxation process. Here, we observe a monotonic decrease in the relaxation time as a function of the magnetic field strength. In this timescale, the spin reservoir starts to cool down and Zeeman energy becomes dominant. Therefore, we could expect the emerging magnetic domains and domain wall motion under magnetic field.

## 8.4 Conclusions

The presented results are preliminary, and show ultrafast demagnetization dynamics of  $[\text{Co}/\text{Pt}]_3$  multilayer as a function of laser fluence and applied magnetic field. We have found that demagnetization time  $\tau_M$  is independent of the above-mentioned parameters.

Our measurements show that two distinct mechanisms may play a role in the relaxation of magnetization. Furthermore, we showed the long-term relaxation, which is attributed to lattice-lattice interactions, is enhanced with applied magnetic field.

In the presented experiments, the pump beam was linearly polarized. Thus, a sign change at the magnetization vector was neither expected nor observed. However, up to the present, a detailed investigation of femtosecond dynamics using circularly polarized laser pulses as well as pulsed magnetic fields is missing in the literature. More detailed studies are in progress to clarify the mechanisms governing the magnetization relaxation in  $[\text{Co}/\text{Pt}]_N$  multilayers.

# Chapter 9

## Conclusion and outlook

The main focus of this work was to demonstrate and elucidate the mechanism of optically induced magnetization reversal in ferromagnetic thin films. Therefore, we have chosen the  $[\text{Co}(4\text{\AA})/\text{Pt}(7\text{\AA})]_N$  multilayer system, for which the preliminary AOS experiments were carried out. The multilayers were grown by the magnetron sputtering technique, where  $N=3, 5, 7$  and  $9$ . In order to image the laser-induced magnetic domains, we built a magneto-optical Kerr effect (MOKE) microscopy setup combined with the femtosecond laser system. In addition, we also employed a photoelectron emission microscope (PEEM), utilizing x-ray magnetic circular dichroism (XMCD) for imaging magnetic contrast with enhanced lateral resolution and element selectivity. The essential outcomes of these experiments are listed below.

At the beginning of this experimental work, we determined the optimum laser beam fluence required for *helicity-dependent* all-optical switching (HD-AOS). The analysis on magnetic images points to the fact that AOS occurs in a very narrow fluence range, which is associated with the thermal energy deposited into the sample by the laser pulses. According to the 2D projection of the Gaussian intensity profile, the optimum laser fluence range gives rise to an ‘AOS ring’ (an area of completely switched magnetization) at the perimeter of illuminated area. If the laser fluence is large enough to heat the sample close to Curie temperature ( $T_C$ ), the magnetization breaks into an assembly of smaller domains. Following the latter, we concluded that the fluence range for AOS is closely related to the temperature and is limited by  $T_C$ . Furthermore, we revealed that deterministic AOS is an accumulative process, i.e., a consequence of multiple pulse illumination. In our  $[\text{Co}/\text{Pt}]_3$  multilayers, the ‘AOS ring’ is initiated after  $\sim 500$  pulses and its width increased with number of pulses.

As we determined the main criteria for AOS, we then varied the laser beam and material parameters in order to further investigate the underlying mechanisms. We first tuned  $T_C$  as well as the coercive field  $H_C$  of the samples by increasing bilayer repetition number, i.e., the total thickness of the multilayers. As a consequence of the

increased  $N$ , the minimum laser fluence for the onset of helicity dependent magnetic domain formation has to be increased proportional to the thickness. However, AOS experiments at different temperatures showed that optically induced domain formation is more efficient at lower temperatures (higher  $H_C$ ), and suggested the omission of the coercive field argument.

In the low temperature experiments, we varied the number of the laser pulses as well as pulse repetition rate in order to analyze the effect of the thermal energy deposited into the sample. The repetition rate determined the size of optically induced magnetic domain spots. At room temperature, the spot size was inversely proportional to the time interval between the pulses. We attributed this effect to the thermal gradient-induced domain wall motion towards the hotter areas of the illuminated spots. The domain walls were pinned at lower temperatures (50 K) and therefore all spots emerged at the same diameter. The above-mentioned arguments led to the conclusion that AOS in ferromagnetic materials is a consequence of heating, thermal gradient driven domain wall motion and eventually laser helicity-dependent domain growth mechanisms.

Even though AOS in ferromagnets is widely accepted as an accumulative process, researchers put in a great effort to demonstrate single-pulse switching. On the other hand, writing a magnetic bit with a fs-pulse excitation would also require time to stabilize. In order to investigate the magnetization dynamics after a single-pulse excitation, we performed time-resolved MOKE experiments. A preliminary investigation using linearly polarized pulses showed demagnetization which is followed by a two-step relaxation. However, it is particularly important to investigate the helicity dependent (de)magnetization dynamics using a pulsed magnetic field source. This is the method to measure solely the effect of laser pulses. Also, multiple-pump/single-probe dynamics might be employed in order to measure reversal dynamics in ferromagnets. These questions remained open and as an outlook for the future.

We expect that our experimental study contributes the current understanding of all-optical switching in ferromagnetic materials. AOS promises fast and energy efficient magnetization reversal for future data storage devices. However, the results presented in the literature so far show that the reversal usually takes much longer time than the duration of the laser pulses. More importantly, for ferromagnetic materials, accumulation of multiple pulses is a necessity to achieve deterministic switching. Recently, the *toggle switching* has been reported when single pulse was focused down to the ground-state magnetic domain size [163]. This highlights the importance of spatial aspects in the reversal process. However, further reducing the laser spot is not possible due to the diffraction limit. Breaking the diffraction limit is possible by near-field transduc-

---

ers (NFT) devices which confine the light energy to a 20 nm spot [252]. Moreover, circularly polarization can be obtained in the near-field radiation [253]. Yet another approach for single-pulse switching should be controlling the domain sizes by patterning ferromagnetic layer. Using a lithography technique, ferromagnetic, single-domain nanopillars with a radius of a few tens of nanometers can be fabricated. Therefore, magnetization is not expected to break into smaller domains and only reverse upon laser illumination. The objective in these techniques should be to investigate the nature of the switching process. Their application in real devices, however, remains to be seen.



# Appendix A

## Gaussian beams

An ideal laser beam is assumed to exhibit a Gaussian intensity profile which corresponds to TEM<sub>00</sub> mode. In general, however, laser beams do not fit to the ideal case with slight deviations. This variance is described with a quality factor, so-called M-squared factor, where  $M^2=1$  represents the ideal Gaussian beam.

Transversal intensity distribution of TEM<sub>00</sub> mode is given by Gaussian function:

$$I \sim A_0 \exp\left(\frac{-2r^2}{w^2}\right) \quad (\text{A.1})$$

where  $A_0$  is the amplitude,  $r$  is the radial coordinate and  $w$  is the beam radius. The beam radius is defined as the spatial distance between the propagation axis ( $z$ ) and the point where the intensity decreases to  $\sim 13.5\%$  ( $1/e^2$ ). When focusing, the beam radius takes the minimum value which is called beam waist,  $w_0$ . In [Figure A.1](#), propagation of the Gaussian beam and its dimensions are shown.

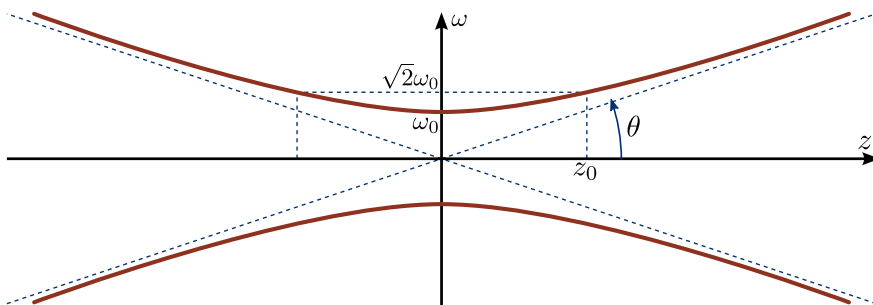


Figure A.1: Gaussian beam propagation around the focal point. The beam waist  $w_0$  is the smallest area at the focal point. Rayleigh range  $z_0$  is the position where the area is twice as larger than the beam waist. The beam diverges with propagation distance due to the diffraction. The divergence angle is given by  $\theta$ .

The distance where the area of the beam is twice as larger than the beam waist is called Rayleigh range and given by  $z_0 = \frac{\pi w_0^2}{\lambda}$ . The relation of beam radius around

Rayleigh range is given by the following formula.

$$\omega = \omega_0 \sqrt{1 + \left(\frac{z - z_1}{z_0}\right)^2} \quad (\text{A.2})$$

Away from the beam waist, the beam diverges with a hyperbolic outline and approach asymptotically to a defined angle  $\theta = \lambda/\pi\omega_0$ .

In order to measure the beam radius, *knife edge* method is a well-known technique. We employed a razor blade attached to a motorized linear stage with a precision of  $3 \mu\text{m}$ , and a powermeter. Laser beam intensity  $P$  was measured at different  $z$  positions while the beam is progressively covered by the blade. The beam radius  $\omega$  was calculated using the equation below.

$$P = P_0 + \frac{P_{max}}{2} \left(1 - \text{erf}\left(\frac{\sqrt{2}(x - x_0)}{\omega}\right)\right) \quad (\text{A.3})$$

where  $P_0$  is background power,  $P_{max}$  is maximal power and  $x_0$  is the position where intensity drops to half. Figure A.2 shows the (squared) beam radii at different  $z$  positions around Rayleigh range and the fitting function associated with Equation A.2.

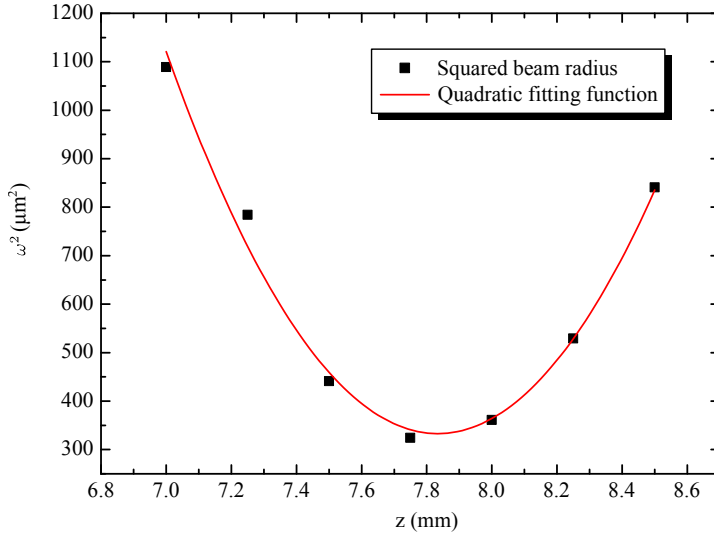


Figure A.2: Squared beam radii at different  $z$  positions around Rayleigh range.

From the fitting curve, we found parameters needed for calculating the  $M^2$  factor. The M-squared factor in our experiment is  $M^2 = 2.44 \pm 0.2$ , which is slightly larger than expected. This is attributed to the aberration due the lenses in focusing objective.

# Appendix B

## Cryostat

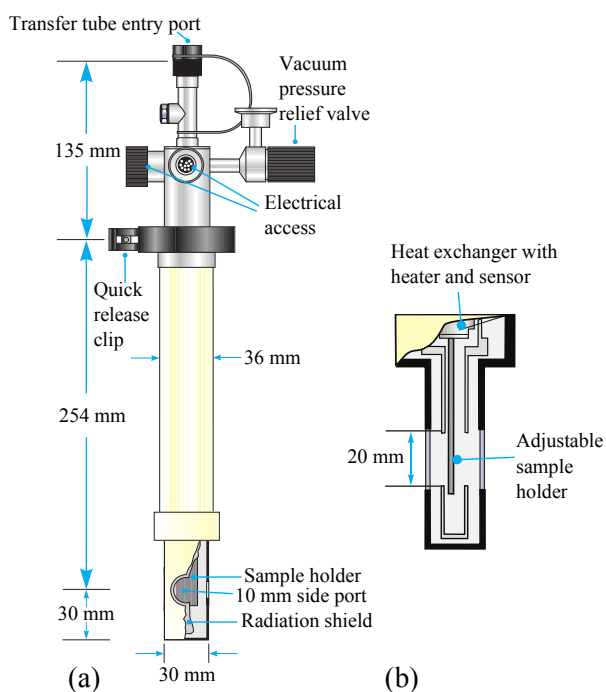


Figure B.1: Microstat™ He-R cryostat system (Oxford Instruments). (a) The body of cryostat and its dimensions. (b) Cross-section of sample holder unit with an optical window suitable for reflection and transmission experiments. The acceptance angle is around  $110^\circ$ .





# Appendix C

## Curie temperature of $[\text{Co}/\text{Pt}]_3$ multilayer

The Curie temperatures of multilayer samples were *not directly* measured. We estimated  $T_C$  of the  $[\text{Co}/\text{Pt}]_3$  multilayer using the XMCD-PEEM magnetic domain images while heating under UHV conditions.

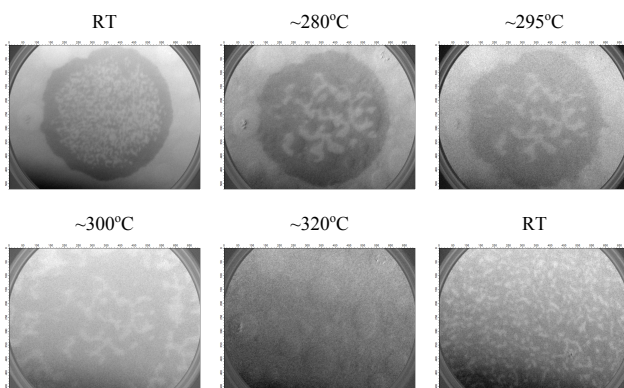


Figure C.1: XMCD-PEEM images of magnetic domains as a function of temperature (FOV:  $43 \mu\text{m}$ ). As the sample is heated from room temperature (RT) to  $\sim 295^\circ\text{C}$ , smaller domains inside the ‘AOS ring’ start to merge and form larger domains, while the ring is more or less stable. At  $\sim 295^\circ\text{C}$ , magnetic state completely vanishes. Magnetic domains emerge when the sample cooled down.

The results presented here are in consistence with Pitcher *et al.* [204] within our experimental precision.



# Appendix D

## Determination of the $p$ -values

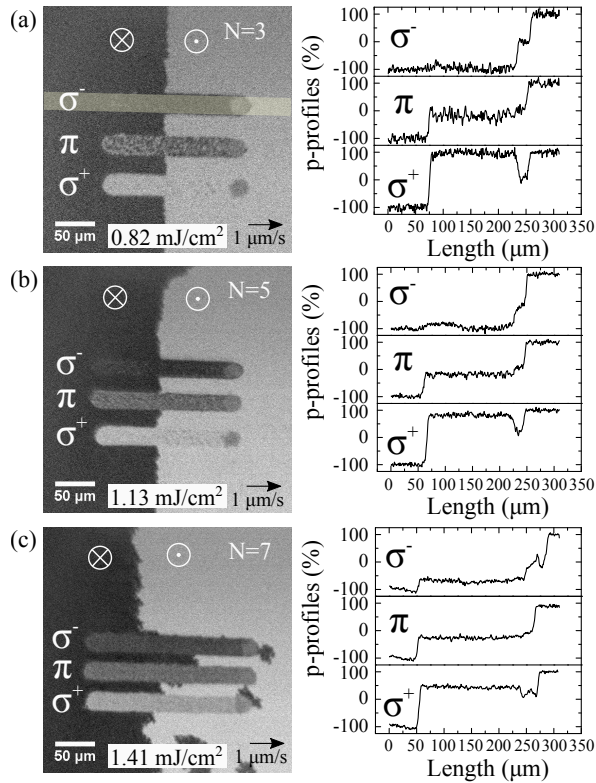


Figure D.1: Determination of  $p$ -values from horizontal profiles. Left: Magneto-optical images of optically-induced magnetic domains in  $[\text{Co}/\text{Pt}]_N$  multilayers of (a)  $N=3$ , (b)  $N=5$  and (c)  $N=7$  repetitions. Normalized domain contrast,  $p$ -values were measured along the horizontal lines as depicted exemplarily with the 30-pixels-wide framed area shown in the upper-left image for  $\sigma^-$  helicity. Right:  $p$ -profiles of the corresponding lines.  $\pm 100\%$  refers to the up and down background domains, respectively.



# Bibliography

- [1] V. Poulsen, “Method of recording and reproducing sounds or signals.” Nov. 13 1900, US Patent 661,619. (Cited in page 1).
- [2] F. Jorgensen, “The inventor Valdemar Poulsen,” *J. Magn. Magn. Mater.*, vol. 193, no. 1-3, pp. 1–7, 1999. (Cited in page 1).
- [3] K. Goda and M. Kitsuregawa, “The history of storage systems,” *Proc. IEEE*, vol. 100, no. Special Centennial Issue, pp. 1433–1440, 2012. (Cited in page 1).
- [4] M. Kief and R. Victora, “Materials for heat-assisted magnetic recording,” *MRS Bull.*, vol. 43, no. 2, pp. 87–92, 2018. (Cited in pages 1, 2).
- [5] A. Moser, K. Takano, D. T. Margulies, M. Albrecht, Y. Sonobe, Y. Ikeda, S. Sun, and E. E. Fullerton, “Magnetic recording: advancing into the future,” *J. Phys. D: Appl. Phys.*, vol. 35, no. 19, p. R157, 2002. (Cited in page 1).
- [6] M. N. Baibich, J. M. Broto, A. Fert, F. N. Van Dau, F. Petroff, P. Etienne, G. Creuzet, A. Friederich, and J. Chazelas, “Giant magnetoresistance of (001)Fe/(001)Cr magnetic superlattices,” *Phys. Rev. Lett.*, vol. 61, no. 21, p. 2472, 1988. (Cited in page 1).
- [7] G. Binasch, P. Grünberg, F. Saurenbach, and W. Zinn, “Enhanced magnetoresistance in layered magnetic structures with antiferromagnetic interlayer exchange,” *Phys. Rev. B*, vol. 39, no. 7, p. 4828, 1989. (Cited in pages 1, 13).
- [8] S. Piramanayagam, “Perpendicular recording media for hard disk drives,” *J. Appl. Phys.*, vol. 102, no. 1, p. 2, 2007. (Cited in pages 1, 57).
- [9] S. Piramanayagam and K. Srinivasan, “Recording media research for future hard disk drives,” *J. Magn. Magn. Mater.*, vol. 321, no. 6, pp. 485–494, 2009. (Cited in page 1).
- [10] S. Iwasaki, “Past and present of perpendicular magnetic recording,” *J. Magn. Magn. Mater.*, vol. 320, no. 22, pp. 2845–2849, 2008. (Cited in page 1).

- 
- [11] Y. Shiroishi, K. Fukuda, I. Tagawa, H. Iwasaki, S. Takenoiri, H. Tanaka, H. Mutoh, and N. Yoshikawa, “Future options for HDD storage,” *IEEE Trans. Magn.*, vol. 45, no. 10, pp. 3816–3822, 2009. (Cited in page 1).
- [12] T. Feldman and G. Gibson, “Shingled magnetic recording: areal density increase requires new data management,” *USENIX; login: Magazine*, vol. 38, no. 3, 2013. (Cited in page 2).
- [13] A. Amer, J. Holliday, D. D. Long, E. L. Miller, J.-F. Pâris, and T. Schwarz, “Data management and layout for shingled magnetic recording,” *IEEE Trans. Magn.*, vol. 47, no. 10, pp. 3691–3697, 2011. (Cited in page 2).
- [14] M. H. Kryder, E. C. Gage, T. W. McDaniel, W. A. Challener, R. E. Rottmayer, G. Ju, Y.-T. Hsia, and M. F. Erden, “Heat assisted magnetic recording,” *Proc. IEEE*, vol. 96, no. 11, pp. 1810–1835, 2008. (Cited in pages 2, 3).
- [15] M. A. Seigler, W. A. Challener, E. Gage, N. Gokemeijer, G. Ju, B. Lu, K. Pelhos, C. Peng, R. E. Rottmayer, X. Yang *et al.*, “Integrated heat assisted magnetic recording head: design and recording demonstration,” *IEEE Trans. Magn.*, vol. 44, no. 1, pp. 119–124, 2008. (Cited in page 2).
- [16] S. Okamoto, N. Kikuchi, M. Furuta, O. Kitakami, and T. Shimatsu, “Microwave assisted magnetic recording technologies and related physics,” *J. Phys. D: Appl. Phys.*, vol. 48, no. 35, p. 353001, 2015. (Cited in page 2).
- [17] J.-G. Zhu, X. Zhu, and Y. Tang, “Microwave assisted magnetic recording,” *IEEE Trans. Magn.*, vol. 44, no. 1, pp. 125–131, 2008. (Cited in page 2).
- [18] E. Hwang, R. Negi, and B. V. Kumar, “Signal processing for near 10 Tbit/in<sup>2</sup> density in two-dimensional magnetic recording (TDMR),” *IEEE Trans. Magn.*, vol. 46, no. 6, pp. 1813–1816, 2010. (Cited in page 2).
- [19] R. Wood, M. Williams, A. Kavcic, and J. Miles, “The feasibility of magnetic recording at 10 Terabits per square inch on conventional media,” *IEEE Trans. Magn.*, vol. 45, no. 2, pp. 917–923, 2009. (Cited in page 2).
- [20] C. A. Ross, “Patterned magnetic recording media,” *Annu. Rev. Mater. Res.*, vol. 31, no. 1, pp. 203–235, 2001. (Cited in page 2).
- [21] T. R. Albrecht, H. Arora, V. Ayanoor-Vitikkate, J.-M. Beaujour, D. Bedau, D. Berman, A. L. Bogdanov, Y.-A. Chapuis, J. Cushen, E. E. Dobisz *et al.*, “Bit-patterned magnetic recording: theory, media fabrication, and recording

- performance,” *IEEE Trans. Magn.*, vol. 51, no. 5, pp. 1–42, 2015. (Cited in page 2).
- [22] S. J. Greaves, Y. Kanai, and H. Muraoka, “Magnetic recording in patterned media at 5–10 Tb/in<sup>2</sup>,” *IEEE Trans. Magn.*, vol. 44, no. 11, pp. 3430–3433, 2008. (Cited in page 2).
- [23] IHS Markit, “SSD and HDD storage market tracker,” 2017, [Online; accessed 10-July-2019]. [Online]. Available: <https://technology.ihs.com/api/binary/590818?attachment=true> (Cited in page 2).
- [24] H. Richter, “The transition from longitudinal to perpendicular recording,” *J. Phys. D: Appl. Phys.*, vol. 40, no. 9, p. R149, 2007. (Cited in page 2).
- [25] H. Richter, A. Lyberatos, U. Nowak, R. F. L. Evans, and R. W. Chantrell, “The thermodynamic limits of magnetic recording,” *J. Appl. Phys.*, vol. 111, no. 3, p. 033909, 2012. (Cited in page 2).
- [26] D. Weller and A. Moser, “Thermal effect limits in ultrahigh-density magnetic recording,” *IEEE Trans. Magn.*, vol. 35, no. 6, pp. 4423–4439, 1999. (Cited in page 2).
- [27] S. H. Charap, P.-L. Lu, and Y. He, “Thermal stability of recorded information at high densities,” *IEEE Trans. Magn.*, vol. 33, no. 1, pp. 978–983, 1997. (Cited in page 3).
- [28] W. Challener, C. Peng, A. Itagi, D. Karns, W. Peng, Y. Peng, X. Yang, X. Zhu, N. Gokemeijer, Y.-T. Hsia *et al.*, “Heat-assisted magnetic recording by a near-field transducer with efficient optical energy transfer,” *Nat. Photonics*, vol. 3, no. 4, p. 220, 2009. (Cited in page 3).
- [29] D. Weller, G. Parker, O. Mosendz, A. Lyberatos, D. Mitin, N. Y. Safonova, and M. Albrecht, “FePt heat assisted magnetic recording media,” *J. Vac. Sci. Technol. B*, vol. 34, no. 6, p. 060801, 2016. (Cited in page 3).
- [30] A. Q. Wu, Y. Kubota, T. Klemmer, T. Rausch, C. Peng, Y. Peng, D. Karns, X. Zhu, Y. Ding, E. K. Chang *et al.*, “HAMR areal density demonstration of 1+ Tbpsi on spinstand,” *IEEE Trans. Magn.*, vol. 49, no. 2, pp. 779–782, 2013. (Cited in page 3).



- [31] M. Re, “HAMR: the next leap forward is now,” 2017, [Online; accessed 10-June-2019]. [Online]. Available: <https://blog.seagate.com/craftsman-ship/hamr-next-leap-forward-now/> (Cited in page 3).
- [32] E. Beaurepaire, J.-C. Merle, A. Daunois, and J.-Y. Bigot, “Ultrafast spin dynamics in ferromagnetic nickel,” *Phys. Rev. Lett.*, vol. 76, no. 22, p. 4250, 1996. (Cited in pages 4, 25, 36, 37, 38, 75).
- [33] C. Stanciu, F. Hansteen, A. Kimel, A. Kirilyuk, A. Tsukamoto, A. Itoh, and T. Rasing, “All-optical magnetic recording with circularly polarized light,” *Phys. Rev. Lett.*, vol. 99, no. 4, p. 047601, 2007. (Cited in pages 4, 41, 42, 43).
- [34] C.-H. Lambert, S. Mangin, B. C. S. Varaprasad, Y. Takahashi, M. Hehn, M. Cinchetti, G. Malinowski, K. Hono, Y. Fainman, M. Aeschlimann *et al.*, “All-optical control of ferromagnetic thin films and nanostructures,” *Science*, vol. 345, no. 6202, pp. 1337–1340, 2014. (Cited in pages 4, 47, 50, 53, 91, 92).
- [35] J. Stöhr and H. C. Siegmann, *Magnetism: From fundamentals to nanoscale dynamics*. Springer, 2006. (Cited in pages 8, 9, 11, 12, 15, 25, 26, 34, 38, 41).
- [36] J. M. Coey, *Magnetism and Magnetic Materials*. Cambridge University Press, 2010. (Cited in pages 8, 23).
- [37] B. D. Cullity and C. D. Graham, *Introduction to Magnetic Materials*. John Wiley & Sons, 2009. (Cited in page 8).
- [38] R. Skomski, *Simple models of magnetism*. Oxford University Press, 2008. (Cited in pages 8, 11, 21).
- [39] M. Wuttig and X. Liu, “Magnetism of Ultrathin Metal Films,” in *Ultrathin Metal Films*. Springer, 2004, pp. 61–124. (Cited in page 9).
- [40] E. C. Stoner, “Collective electron ferromagnetism,” *Proc. Royal Soc. A*, vol. 165, no. 922, pp. 372–414, 1938. (Cited in page 9).
- [41] P. Mohn, *Magnetism in the solid state: An introduction*. Springer, 2006. (Cited in page 9).
- [42] D. Jiles, *Introduction to magnetism and magnetic materials*. CRC press, 2015. (Cited in page 9).
- [43] M. Getzlaff, *Fundamentals of Magnetism*. Springer, 2007. (Cited in pages 9, 17, 18, 22).

- [44] L. Bergmann and C. Schaefer, *Lehrbuch der Experimentalphysik Band 6. Festkörper*. Walter de Gruyter, 2005. (Cited in page 11).
- [45] E. Şaşıoğlu, “First-principles study of the exchange interactions and Curie temperature in Heusler alloys,” Ph.D. dissertation, Mathematisch–Naturwissenschaftlich–Technischen Fakultät der Martin–Luther–Universität Halle, Wittenberg, 2006. (Cited in page 11).
- [46] R. Wu, “Fundamental properties of magnetic nanostructures: a survey,” in *Nanomagnetism: Ultrathin films, multilayers and nanostructures*, D. Mills and J. Bland, Eds. Elsevier, 2006, ch. 2, pp. 29–49. (Cited in page 11).
- [47] A. P. Guimarães, *Principles of nanomagnetism*. Springer, 2009. (Cited in page 11).
- [48] C. Vaz, J. Bland, and G. Lauhoff, “Magnetism in ultrathin film structures,” *Rep. Prog. Phys.*, vol. 71, no. 5, p. 056501, 2008. (Cited in pages 11, 13).
- [49] F. Hellman, A. Hoffmann, Y. Tserkovnyak, G. S. Beach, E. E. Fullerton, C. Leighton, A. H. MacDonald, D. C. Ralph, D. A. Arena, H. A. Dürr *et al.*, “Interface-induced phenomena in magnetism,” *Rev. Mod. Phys.*, vol. 89, no. 2, p. 025006, 2017. (Cited in pages 11, 12, 14, 39, 47).
- [50] K. Shanavas, Z. Popović, and S. Satpathy, “Theoretical model for Rashba spin-orbit interaction in d electrons,” *Phys. Rev. B*, vol. 90, no. 16, p. 165108, 2014. (Cited in page 12).
- [51] K. Bennemann, “Magnetic nanostructures,” *J. Phys. Condens. Matter*, vol. 22, no. 24, p. 243201, 2010. (Cited in page 13).
- [52] J. Nogués and I. K. Schuller, “Exchange bias,” *J. Magn. Magn. Mater.*, vol. 192, no. 2, pp. 203–232, 1999. (Cited in page 13).
- [53] J. Nogués, J. Sort, V. Langlais, V. Skumryev, S. Surinach, J. Muñoz, and M. Baró, “Exchange bias in nanostructures,” *Phys. Rep.*, vol. 422, no. 3, pp. 65–117, 2005. (Cited in page 13).
- [54] S. Parkin, N. More, and K. Roche, “Oscillations in exchange coupling and magnetoresistance in metallic superlattice structures: Co/Ru, Co/Cr, and Fe/Cr,” *Phys. Rev. Lett.*, vol. 64, no. 19, p. 2304, 1990. (Cited in page 13).

- [55] A. Fert, P. Grünberg, A. Barthélémy, F. Petroff, and W. Zinn, “Layered magnetic structures: interlayer exchange coupling and giant magnetoresistance,” *J. Magn. Magn. Mater.*, vol. 140, pp. 1–8, 1995. (Cited in page 13).
- [56] É. Trémolet de Lacheisserie, M. Schlenker, and D. Gignoux, *Magnetism: materials and applications*. Springer, 2005. (Cited in page 13).
- [57] P. Pouloupoulos, A. Scherz, F. Wilhelm, H. Wende, and K. Baberschke, “Direct probe of induced magnetic moments at interfaces via x-ray magnetic circular dichroism,” *Phys. Status Solidi A*, vol. 189, no. 2, pp. 293–300, 2002. (Cited in pages 14, 72).
- [58] J. Bartolomé, L. García, F. Bartolomé, F. Luis, F. Petroff, C. Deranlot, F. Wilhelm, and A. Rogalev, “Magnetic properties of Co nanoparticle granular films capped with Pt,” *J. Magn. Magn. Mater.*, vol. 316, no. 2, pp. e9–e12, 2007. (Cited in page 14).
- [59] P. Carcia, A. Meinhardt, and A. Suna, “Perpendicular magnetic anisotropy in Pd/Co thin film layered structures,” *Appl. Phys. Lett.*, vol. 47, no. 2, pp. 178–180, 1985. (Cited in pages 14, 17).
- [60] H. Yang, A. Thiaville, S. Rohart, A. Fert, and M. Chshiev, “Anatomy of Dzyaloshinskii-Moriya interaction at Co/Pt interfaces,” *Phys. Rev. Lett.*, vol. 115, no. 26, p. 267210, 2015. (Cited in page 14).
- [61] R. M. Rowan-Robinson, A. Stashkevich, Y. Roussigné, M. Belmeguenai, S.-M. Chérif, A. Thiaville, T. Hase, A. Hindmarch, and D. Atkinson, “The interfacial nature of proximity-induced magnetism and the Dzyaloshinskii-Moriya interaction at the Pt/Co interface,” *Sci. Rep.*, vol. 7, no. 1, p. 16835, 2017. (Cited in page 14).
- [62] S.-G. Je, P. Vallobra, T. Srivastava, J.-C. Rojas-Sánchez, T. H. Pham, M. Hehn, G. Malinowski, C. Baraduc, S. Auffret, G. Gaudin *et al.*, “Creation of magnetic Skyrmion bubble lattices by ultrafast laser in ultrathin films,” *Nano Lett.*, vol. 18, no. 11, pp. 7362–7371, 2018. (Cited in page 14).
- [63] C. Kittel, *Introduction to solid state physics*. Wiley New York, 2004. (Cited in page 15).
- [64] J. Lindner and M. Farle, “Magnetic anisotropy of heterostructures,” in *Magnetic Heterostructures*, H. Zabel and S. D. Bader, Eds. Springer, 2008, ch. 2, pp. 45–96. (Cited in page 15).

- [65] W. de Jonge, P. Bloemen, and F. den Broeder, “Experimental Investigations of Magnetic Anisotropy,” in *Ultrathin Magnetic Structures I: An introduction to the electronic, magnetic and structural properties*, J. A. C. Bland and B. Heinrich, Eds. Springer, 2006, ch. 2.3, pp. 65–86. (Cited in page 15).
- [66] J. Crangle, *Solid State Magnetism*. Springer, 1991. (Cited in page 16).
- [67] S. Chikazumi and C. D. Graham, *Physics of Ferromagnetism*. Oxford University Press, 2009. (Cited in page 16).
- [68] M. Johnson, P. Bloemen, F. Den Broeder, and J. De Vries, “Magnetic anisotropy in metallic multilayers,” *Rep. Prog. Phys.*, vol. 59, no. 11, p. 1409, 1996. (Cited in pages 17, 18).
- [69] P. Carcia, “Perpendicular magnetic anisotropy in Pd/Co and Pt/Co thin-film layered structures,” *J. Appl. Phys.*, vol. 63, no. 10, pp. 5066–5073, 1988. (Cited in pages 17, 53, 54, 56).
- [70] F. Den Broeder, D. Kuiper, A. Van de Mosselaer, and W. Hoving, “Perpendicular magnetic anisotropy of Co-Au multilayers induced by interface sharpening,” *Phys. Rev. Lett.*, vol. 60, no. 26, p. 2769, 1988. (Cited in page 17).
- [71] F. Den Broeder, W. Hoving, and P. Bloemen, “Magnetic anisotropy of multilayers,” *J. Magn. Magn. Mater.*, vol. 93, pp. 562–570, 1991. (Cited in pages 17, 18).
- [72] F. Den Broeder, E. Janssen, W. Hoving, and W. Zeper, “Perpendicular magnetic anisotropy and coercivity of Co/Ni multilayers,” *IEEE Trans. Magn.*, vol. 28, no. 5, pp. 2760–2765, 1992. (Cited in page 17).
- [73] G. Daalderop, P. Kelly, and F. Den Broeder, “Prediction and confirmation of perpendicular magnetic anisotropy in Co/Ni multilayers,” *Phys. Rev. Lett.*, vol. 68, no. 5, p. 682, 1992. (Cited in page 17).
- [74] S.-C. Shin, G. Srinivas, Y.-S. Kim, and M.-G. Kim, “Observation of perpendicular magnetic anisotropy in Ni/Pt multilayers at room temperature,” *Appl. Phys. Lett.*, vol. 73, no. 3, pp. 393–395, 1998. (Cited in page 17).
- [75] H. Yang, M. Chshiev, B. Dieny, J. Lee, A. Manchon, and K. Shin, “First-principles investigation of the very large perpendicular magnetic anisotropy at Fe|MgO and Co|MgO interfaces,” *Phys. Rev. B*, vol. 84, no. 5, p. 054401, 2011. (Cited in page 17).

- [76] F. Richomme, J. Teillet, A. Fnidiki, P. Auric, and P. Houdy, “Experimental study of the structural and magnetic properties of Fe/Tb multilayers,” *Phys. Rev. B*, vol. 54, no. 1, p. 416, 1996. (Cited in page 17).
- [77] S. Honda, M. Nawate, and I. Sakamoto, “Magnetic structure and perpendicular magnetic anisotropy of rare-earth (Nd, Pr, Gd)/Fe multilayers,” *J. Appl. Phys.*, vol. 79, no. 1, pp. 365–372, 1996. (Cited in page 17).
- [78] N. Heiman, A. Onton, D. Kyser, K. Lee, and C. Guarnieri, “Uniaxial anisotropy in rare earth (Gd, Ho, Tb)-transition metal (Fe, Co) amorphous films,” in *AIP Conference Proceedings*, vol. 24, no. 1. AIP, 1975, pp. 573–574. (Cited in page 17).
- [79] P. Hansen, C. Clausen, G. Much, M. Rosenkranz, and K. Witter, “Magnetic and magneto-optical properties of rare-earth transition-metal alloys containing Gd, Tb, Fe, Co,” *J. Appl. Phys.*, vol. 66, no. 2, pp. 756–767, 1989. (Cited in page 17).
- [80] P. Hansen, S. Klahn, C. Clausen, G. Much, and K. Witter, “Magnetic and magneto-optical properties of rare-earth transition-metal alloys containing Dy, Ho, Fe, Co,” *J. Appl. Phys.*, vol. 69, no. 5, pp. 3194–3207, 1991. (Cited in page 17).
- [81] K. Chen, D. Lott, F. Radu, F. Choueikani, E. Otero, and P. Ohresser, “Temperature-dependent magnetic properties of ferrimagnetic DyCo<sub>3</sub> alloy films,” *Phys. Rev. B*, vol. 91, no. 2, p. 024409, 2015. (Cited in page 17).
- [82] R. Cid, J. Alameda, S. Valvidares, J. Cezar, P. Bencok, N. Brookes, and J. Díaz, “Perpendicular magnetic anisotropy in amorphous Nd<sub>x</sub>Co<sub>1-x</sub> thin films studied by x-ray magnetic circular dichroism,” *Phys. Rev. B*, vol. 95, no. 22, p. 224402, 2017. (Cited in page 17).
- [83] B. N. Engel, C. D. England, R. A. Van Leeuwen, M. H. Wiedmann, and C. M. Falco, “Interface magnetic anisotropy in epitaxial superlattices,” *Phys. Rev. Lett.*, vol. 67, no. 14, p. 1910, 1991. (Cited in page 18).
- [84] P. C. Prabhajan D. Kulkarni, Somnath Bhattacharyya, “Perpendicular Magnetic Anisotropy in Magnetic Thin Films,” in *Advances in Magnetic Materials: Processing, properties, and performance*, S. Zhang and D. Zhao, Eds. Routledge Handbooks Online, 2017, ch. 9, pp. 582–626. (Cited in page 18).

- [85] X.-X. Li, J. Bao, L.-Y. Lu, X.-G. Xu, and Y. Jiang, "Oscillatory antiferromagnetic interlayer coupling in Co/Pt multilayer with perpendicular anisotropy," *Solid State Commun.*, vol. 148, no. 5, pp. 209–212, 2008. (Cited in page 19).
- [86] J. Moritz, F. Garcia, J. Toussaint, B. Dieny, and J. Nozieres, "Orange peel coupling in multilayers with perpendicular magnetic anisotropy: Application to (Co/Pt)-based exchange-biased spin-valves," *EPL*, vol. 65, no. 1, p. 123, 2004. (Cited in pages 19, 20).
- [87] M. D. Stiles, "Interlayer exchange coupling," *J. Magn. Magn. Mater.*, vol. 200, no. 1-3, pp. 322–337, 1999. (Cited in page 19).
- [88] J. Knepper and F. Yang, "Oscillatory interlayer coupling in Co/ Pt multilayers with perpendicular anisotropy," *Phys. Rev. B*, vol. 71, no. 22, p. 224403, 2005. (Cited in page 20).
- [89] C. Kooy, "Experimental and theoretical study of the domain configuration in thin layers of BaFe<sub>12</sub>O<sub>19</sub>," *Philips Res. Repts*, vol. 15, no. 7, 1960. (Cited in pages 21, 55).
- [90] M. Mansuripur, *The physical principles of magneto-optical recording*. Cambridge University Press, 1995. (Cited in pages 21, 36, 54, 107).
- [91] M. E. McHenry and D. E. Laughlin, "Magnetic properties of metals and alloys," in *Physical Metallurgy*, D. E. Laughlin and K. Hono, Eds. Elsevier, 2014, ch. 19, pp. 1881–2008. (Cited in page 22).
- [92] A. Hubert and R. Schäfer, *Magnetic Domains: The analysis of magnetic microstructure*. Springer, 1998. (Cited in pages 23, 85).
- [93] E. Della Torre, *Magnetic Hysteresis*. Wiley, 2000. (Cited in page 23).
- [94] W. Zeper, H. Van Kesteren, B. Jacobs, J. Spruit, and P. Carcia, "Hysteresis, microstructure, and magneto-optical recording in Co/Pt and Co/Pd multilayers," *J. Appl. Phys.*, vol. 70, no. 4, pp. 2264–2271, 1991. (Cited in pages 23, 84).
- [95] T. Suzuki, H. Notarys, D. Dobbertin, C.-J. Lin, D. Weller, D. Miller, and G. Gorman, "Coercivity mechanism and microstructure of (Co/Pt) multilayers," *IEEE Trans. Magn.*, vol. 28, no. 5, pp. 2754–2759, 1992. (Cited in pages 23, 70).
- [96] J. Ferré, "Dynamics of magnetization reversal: from continuous to patterned ferromagnetic films," in *Spin Dynamics in Confined Magnetic Structures I*, B. Hille-

- brands and K. Ounadjela, Eds. Springer, 2002, ch. 5, pp. 127–165. (Cited in page 24).
- [97] J. X. Shen, R. D. Kirby, K. Wierman, Z. S. Shan, D. J. Sellmyer, and T. Suzuki, “Magnetization reversal and defects in Co/Pt multilayers,” *J. Appl. Phys.*, vol. 73, no. 10, pp. 6418–6420, 1993. (Cited in page 24).
- [98] M. Farle, “Ferromagnetic resonance of ultrathin metallic layers,” *Rep. Prog. Phys.*, vol. 61, no. 7, p. 755, 1998. (Cited in page 24).
- [99] J. Katine, F. Albert, R. Buhrman, E. Myers, and D. Ralph, “Current-driven magnetization reversal and spin-wave excitations in Co/Cu/Co pillars,” *Phys. Rev. Lett.*, vol. 84, no. 14, p. 3149, 2000. (Cited in page 25).
- [100] S. Mangin, D. Ravelosona, J. Katine, M. Carey, B. Terris, and E. E. Fullerton, “Current-induced magnetization reversal in nanopyllars with perpendicular anisotropy,” *Nat. Mater.*, vol. 5, no. 3, p. 210, 2006. (Cited in page 25).
- [101] M. Weisheit, S. Fähler, A. Marty, Y. Souche, C. Poinsignon, and D. Givord, “Electric field-induced modification of magnetism in thin-film ferromagnets,” *Science*, vol. 315, no. 5810, pp. 349–351, 2007. (Cited in page 25).
- [102] C. Back, R. Allenspach, W. Weber, S. Parkin, D. Weller, E. L. Garwin, and H. Siegmann, “Minimum field strength in precessional magnetization reversal,” *Science*, vol. 285, no. 5429, pp. 864–867, 1999. (Cited in page 25).
- [103] T. Gerrits, H. Van Den Berg, J. Hohlfeld, L. Bär, and T. Rasing, “Ultrafast precessional magnetization reversal by picosecond magnetic field pulse shaping,” *Nature*, vol. 418, no. 6897, p. 509, 2002. (Cited in page 25).
- [104] I. Tudosa, C. Stamm, A. Kashuba, F. King, H. Siegmann, J. Stöhr, G. Ju, B. Lu, and D. Weller, “The ultimate speed of magnetic switching in granular recording media,” *Nature*, vol. 428, no. 6985, p. 831, 2004. (Cited in page 25).
- [105] A. G. Gurevich and G. A. Melkov, *Magnetization oscillations and waves*. CRC press, 1996. (Cited in page 25).
- [106] J. C. Slonczewski, “Current-driven excitation of magnetic multilayers,” *J. Magn. Magn. Mater.*, vol. 159, no. 1-2, pp. L1–L7, 1996. (Cited in page 25).
- [107] M. Faraday, “On the magnetization of light and the illumination of magnetic lines of force,” *Philos. Trans. Royal Soc.*, vol. 136, pp. 1–20, 1846. (Cited in page 26).

- [108] T. Cornelissen, R. Córdoba, and B. Koopmans, “Microscopic model for all optical switching in ferromagnets,” *Appl. Phys. Lett.*, vol. 108, no. 14, p. 142405, 2016. (Cited in pages 27, 32, 49, 52).
- [109] M. A. Kozhaev, A. I. Chernov, D. A. Sylgacheva, A. N. Shaposhnikov, A. R. Prokopov, V. N. Berzhansky, A. K. Zvezdin, and V. I. Belotelov, “Giant peak of the Inverse Faraday effect in the band gap of magnetophotonic microcavity,” *Sci. Rep.*, vol. 8, no. 1, pp. 1–7, 2018. (Cited in page 27).
- [110] J. Kerr, “On rotation of the plane of polarization by reflection from the pole of a magnet,” *Philos. Mag.*, vol. 3, no. 19, pp. 321–343, 1877. (Cited in page 27).
- [111] P. Zeeman, “On the Influence of Magnetism on the Nature of the Light Emitted by a Substance,” *Astrophys. J.*, vol. 5, p. 332, 1897. (Cited in page 27).
- [112] W. Voigt, “Doppelbrechung von im magnetfelde befindlichem natriumdampf in der richtung normal zu den kraftlinien,” *Nachrichten von der Gesellschaft der Wissenschaften zu Göttingen, Mathematisch-Physikalische Klasse*, vol. 1898, pp. 355–359, 1898. (Cited in page 27).
- [113] A. Cotton and H. Mouton, “Sur les propriétés magnétooptiques des colloïdes et des liqueurs hétérogenes,” *Ann. Chim. Phys.*, vol. 11, pp. 145–203, 1907. (Cited in page 27).
- [114] P. Oppeneer, “Magneto-optical Kerr spectra,” in *Handbook of Magnetic Materials*, K. H. J. Buschow, Ed. Elsevier, 2001, vol. 13, ch. 3, pp. 229–422. (Cited in pages 27, 31).
- [115] A. Yaresko, A. Perlov, V. Antonov, and B. Harmon, “Band-structure theory of dichroism,” in *Magnetism: A Synchrotron Radiation Approach*, F. S. J.-P. K. E. Beaurepaire, H. Bulou, Ed. Springer, 2006, ch. 6, pp. 121–141. (Cited in pages 28, 33).
- [116] C.-Y. You and S.-C. Shin, “Generalized analytic formulae for magneto-optical Kerr effects,” *J. Appl. Phys.*, vol. 84, no. 1, pp. 541–546, 1998. (Cited in page 30).
- [117] J. Zak, E. Moog, C. Liu, and S. Bader, “Universal approach to magneto-optics,” *J. Magn. Magn. Mater.*, vol. 89, no. 1-2, pp. 107–123, 1990. (Cited in page 30).



- [118] K. Shinagawa, “Faraday and Kerr effects in ferromagnets,” in *Magneto-optics*, S. Sugano and N. Kojima, Eds. Springer, 2000, ch. 5, pp. 137–177. (Cited in pages 30, 31).
- [119] T. Yokoyama, T. Nakagawa, and Y. Takagi, “Magnetic circular dichroism for surface and thin film magnetism: Measurement techniques and surface chemical applications,” *Int. Rev. Phys. Chem.*, vol. 27, no. 3, pp. 449–505, 2008. (Cited in page 30).
- [120] W. Kuch, R. Schäfer, P. Fischer, and F. U. Hillebrecht, *Magnetic microscopy of layered structures*. Springer, 2016. (Cited in pages 31, 32, 62, 82, 85).
- [121] N. A. Spaldin, *Magnetic Materials: Fundamentals and applications*. Cambridge University Press, 2010. (Cited in page 31).
- [122] J. Hamrle, “Magneto-optical determination of the in-depth magnetization profile in magnetic multilayers,” Ph.D. dissertation, Université Paris, Sud-Paris XI, 2003. (Cited in page 32).
- [123] L. P. Pitaevskii, “Electric forces in a transparent dispersive medium,” *Sov. Phys. JETP*, vol. 12, no. 5, pp. 1008–1013, 1961. (Cited in page 31).
- [124] R. Hertel, “Theory of the inverse Faraday effect in metals,” *J. Magn. Magn. Mater.*, vol. 303, no. 1, pp. L1–L4, 2006. (Cited in pages 31, 32).
- [125] M. Weiss, R. Follath, K. Sawhney, F. Senf, J. Bahrtdt, W. Frentrup, A. Gaupp, S. Sasaki, M. Scheer, H.-C. Mertins *et al.*, “The elliptically polarized undulator beamlines at BESSY II,” *Nucl. Instrum. Methods Phys. Res. A*, vol. 467, pp. 449–452, 2001. (Cited in page 33).
- [126] O. Kfir, P. Grychtol, E. Turgut, R. Knut, D. Zusin, D. Popmintchev, T. Popmintchev, H. Nembach, J. M. Shaw, A. Fleischer *et al.*, “Generation of bright phase-matched circularly-polarized extreme ultraviolet high harmonics,” *Nat. Photonics*, vol. 9, no. 2, p. 99, 2015. (Cited in page 33).
- [127] S.-g. Gang, R. Adam, M. Plötzing, M. von Witzleben, C. Weier, U. Parlak, D. E. Bürgler, C. M. Schneider, J. Rusz, P. Maldonado *et al.*, “Element-selective investigation of femtosecond spin dynamics in NiPd magnetic alloys using extreme ultraviolet radiation,” *Phys. Rev. B*, vol. 97, no. 6, p. 064412, 2018. (Cited in page 33).

- [128] S. Pizzini, J. Vogel, M. Bonfim, and A. Fontaine, “Time-resolved x-ray magnetic circular dichroism—A selective probe of magnetization dynamics on nanosecond timescales,” in *Spin Dynamics in Confined Magnetic Structures II*, B. Hillebrands and K. Ounadjela, Eds. Springer, 2003, ch. 5, pp. 157–187. (Cited in page 33).
- [129] J. Stöhr, “X-ray magnetic circular dichroism spectroscopy of transition metal thin films,” *J. Electron Spectros. Relat. Phenomena*, vol. 75, pp. 253–272, 1995. (Cited in page 34).
- [130] A. Scholl, L. Baumgarten, R. Jacquemin, and W. Eberhardt, “Ultrafast spin dynamics of ferromagnetic thin films observed by fs spin-resolved two-photon photoemission,” *Phys. Rev. Lett.*, vol. 79, no. 25, p. 5146, 1997. (Cited in page 36).
- [131] C. Stamm, T. Kachel, N. Pontius, R. Mitzner, T. Quast, K. Holldack, S. Khan, C. Lupulescu, E. Aziz, M. Wietstruk *et al.*, “Femtosecond modification of electron localization and transfer of angular momentum in nickel,” *Nat. Mater.*, vol. 6, no. 10, p. 740, 2007. (Cited in page 36).
- [132] B. Koopmans, M. Van Kampen, J. Kohlhepp, and W. De Jonge, “Ultrafast magneto-optics in nickel: magnetism or optics?” *Phys. Rev. Lett.*, vol. 85, no. 4, p. 844, 2000. (Cited in page 36).
- [133] A. Kirilyuk, A. V. Kimel, and T. Rasing, “Ultrafast optical manipulation of magnetic order,” *Rev. Mod. Phys.*, vol. 82, no. 3, p. 2731, 2010. (Cited in pages 38, 48, 52).
- [134] M. Giovannella, “Time resolved magneto-optical measurements of ultrafast demagnetization dynamics,” Ph.D. dissertation, Università degli Studi di Pisa, Pisa, 2013. (Cited in page 38).
- [135] B. Koopmans, “Time-resolved Kerr-effect and spin dynamics in itinerant ferromagnets,” in *Handbook of Magnetism and Advanced Magnetic Materials*, H. Kronmüller and S. Parkin, Eds. Wiley Online Library, 2007. (Cited in page 38).
- [136] F. Dalla Longa, “Laser-induced magnetization dynamics: an ultrafast journey among spins and light pulses,” Ph.D. dissertation, Eindhoven University of Technology, Eindhoven, 2008. (Cited in page 38).

- [137] L. Guidoni, E. Beaurepaire, and J.-Y. Bigot, “Magneto-optics in the ultrafast regime: Thermalization of spin populations in ferromagnetic films,” *Phys. Rev. Lett.*, vol. 89, no. 1, p. 017401, 2002. (Cited in page 39).
- [138] G. Zhang and W. Hübner, “Laser-induced ultrafast demagnetization in ferromagnetic metals,” *Phys. Rev. Lett.*, vol. 85, no. 14, p. 3025, 2000. (Cited in pages 39, 41).
- [139] M. Si and G. Zhang, “Resolving photon-shortage mystery in femtosecond magnetism,” *J. Phys. Condens. Matter*, vol. 22, no. 7, p. 076005, 2010. (Cited in page 39).
- [140] H.-S. Rhie, H. Dürr, and W. Eberhardt, “Femtosecond electron and spin dynamics in Ni/W(110) films,” *Phys. Rev. Lett.*, vol. 90, no. 24, p. 247201, 2003. (Cited in page 39).
- [141] M. Krauß, T. Roth, S. Alebrand, D. Steil, M. Cinchetti, M. Aeschlimann, and H. C. Schneider, “Ultrafast demagnetization of ferromagnetic transition metals: The role of the Coulomb interaction,” *Phys. Rev. B*, vol. 80, no. 18, p. 180407, 2009. (Cited in page 39).
- [142] B. Koopmans, J. Ruigrok, F. Dalla Longa, and W. De Jonge, “Unifying ultrafast magnetization dynamics,” *Phys. Rev. Lett.*, vol. 95, no. 26, p. 267207, 2005. (Cited in page 39).
- [143] B. Koopmans, G. Malinowski, F. Dalla Longa, D. Steiauf, M. Fähnle, T. Roth, M. Cinchetti, and M. Aeschlimann, “Explaining the paradoxical diversity of ultrafast laser-induced demagnetization,” *Nat. Mater.*, vol. 9, no. 3, p. 259, 2010. (Cited in page 40).
- [144] M. G. Münzenberg, “Magnetization dynamics: Ferromagnets stirred up,” *Nat. Mater.*, vol. 9, no. 3, p. 184, 2010. (Cited in page 40).
- [145] M. Battiato, K. Carva, and P. M. Oppeneer, “Superdiffusive spin transport as a mechanism of ultrafast demagnetization,” *Phys. Rev. Lett.*, vol. 105, no. 2, p. 027203, 2010. (Cited in page 40).
- [146] M. Battiato, K. Carva, and P. Oppeneer, “Theory of laser-induced ultrafast superdiffusive spin transport in layered heterostructures,” *Phys. Rev. B*, vol. 86, no. 2, p. 024404, 2012. (Cited in page 40).

- [147] V. Zhukov, E. Chulkov, and P. Echenique, “Lifetimes and inelastic mean free path of low-energy excited electrons in Fe, Ni, Pt, and Au: Ab initio GW+ T calculations,” *Phys. Rev. B*, vol. 73, no. 12, p. 125105, 2006. (Cited in page 40).
- [148] R. Gómez-Abal and W. Hübner, “Simple model for laser-induced electron dynamics,” *Phys. Rev. B*, vol. 65, no. 19, p. 195114, 2002. (Cited in page 41).
- [149] A. Kimel, A. Kirilyuk, P. Usachev, R. Pisarev, A. Balbashov, and T. Rasing, “Ultrafast non-thermal control of magnetization by instantaneous photomagnetic pulses,” *Nature*, vol. 435, no. 7042, pp. 655–657, 2005. (Cited in pages 41, 42, 49).
- [150] T. Ostler, J. Barker, R. Evans, R. Chantrell, U. Atxitia, O. Chubykalo-Fesenko, S. El Moussaoui, L. Le Guyader, E. Mengotti, L. Heyderman *et al.*, “Ultrafast heating as a sufficient stimulus for magnetization reversal in a ferrimagnet,” *Nature Commun.*, vol. 3, p. 666, 2012. (Cited in pages 44, 48).
- [151] I. Radu, K. Vahaplar, C. Stamm, T. Kachel, N. Pontius, H. Dürr, T. Ostler, J. Barker, R. Evans, R. Chantrell *et al.*, “Transient ferromagnetic-like state mediating ultrafast reversal of antiferromagnetically coupled spins,” *Nature*, vol. 472, no. 7342, p. 205, 2011. (Cited in pages 45, 48).
- [152] S. Alebrand, M. Gottwald, M. Hehn, D. Steil, M. Cinchetti, D. Lacour, E. E. Fullerton, M. Aeschlimann, and S. Mangin, “Light-induced magnetization reversal of high-anisotropy TbCo alloy films,” *Appl. Phys. Lett.*, vol. 101, no. 16, p. 162408, 2012. (Cited in page 45).
- [153] S. Mangin, M. Gottwald, C. Lambert, D. Steil, V. Uhlř, L. Pang, M. Hehn, S. Alebrand, M. Cinchetti, G. Malinowski *et al.*, “Engineered materials for all-optical helicity-dependent magnetic switching,” *Nat. Mater.*, vol. 13, no. 3, p. 286, 2014. (Cited in pages 45, 46).
- [154] S. Alebrand, U. Bierbrauer, M. Hehn, M. Gottwald, O. Schmitt, D. Steil, E. E. Fullerton, S. Mangin, M. Cinchetti, and M. Aeschlimann, “Subpicosecond magnetization dynamics in TbCo alloys,” *Phys. Rev. B*, vol. 89, no. 14, p. 144404, 2014. (Cited in page 45).
- [155] A. Hassdenteufel, J. Schmidt, C. Schubert, B. Hebler, M. Helm, M. Albrecht, and R. Bratschitsch, “Low-remanence criterion for helicity-dependent all-optical magnetic switching in ferrimagnets,” *Phys. Rev. B*, vol. 91, no. 10, p. 104431, 2015. (Cited in page 46).

- [156] M. S. El Hadri, M. Hehn, P. Pirro, C.-H. Lambert, G. Malinowski, E. E. Fullerton, and S. Mangin, “Domain size criterion for the observation of all-optical helicity-dependent switching in magnetic thin films,” *Phys. Rev. B*, vol. 94, no. 6, p. 064419, 2016. (Cited in page 47).
- [157] R. John, M. Berritta, D. Hinzke, C. Müller, T. Santos, H. Ulrichs, P. Nieves, J. Walowski, R. Mondal, O. Chubykalo-Fesenko *et al.*, “Magnetisation switching of FePt nanoparticle recording medium by femtosecond laser pulses,” *Sci. Rep.*, vol. 7, no. 1, p. 4114, 2017. (Cited in page 47).
- [158] Y. Takahashi, R. Medapalli, S. Kasai, J. Wang, K. Ishioka, S. Wee, O. Hellwig, K. Hono, and E. Fullerton, “Accumulative magnetic switching of ultrahigh-density recording media by circularly polarized light,” *Phys. Rev. Appl.*, vol. 6, no. 5, p. 054004, 2016. (Cited in page 47).
- [159] J. Gorchon, Y. Yang, and J. Bokor, “Model for multishot all-thermal all-optical switching in ferromagnets,” *Phys. Rev. B*, vol. 94, no. 2, p. 020409, 2016. (Cited in pages 47, 49, 50, 51, 52).
- [160] M. S. El Hadri, P. Pirro, C.-H. Lambert, S. Petit-Watlot, Y. Quessab, M. Hehn, F. Moutaigne, G. Malinowski, and S. Mangin, “Two types of all-optical magnetization switching mechanisms using femtosecond laser pulses,” *Phys. Rev. B*, vol. 94, no. 6, p. 064412, 2016. (Cited in pages 47, 52, 91).
- [161] Y. Quessab, R. Medapalli, M. El Hadri, M. Hehn, G. Malinowski, E. Fullerton, and S. Mangin, “Helicity-dependent all-optical domain wall motion in ferromagnetic thin films,” *Phys. Rev. B*, vol. 97, no. 5, p. 054419, 2018. (Cited in pages 47, 107).
- [162] J. Gorchon, C.-H. Lambert, Y. Yang, A. Pattabi, R. B. Wilson, S. Salahuddin, and J. Bokor, “Single shot ultrafast all optical magnetization switching of ferromagnetic Co/Pt multilayers,” *Appl. Phys. Lett.*, vol. 111, no. 4, p. 042401, 2017. (Cited in page 47).
- [163] M. Laliou, M. Peeters, S. Haenen, R. Lavrijsen, and B. Koopmans, “Deterministic all-optical switching of synthetic ferrimagnets using single femtosecond laser pulses,” *Phys. Rev. B*, vol. 96, no. 22, p. 220411, 2017. (Cited in pages 47, 126).
- [164] M. Vomir, M. Albrecht, and J.-Y. Bigot, “Single shot all optical switching of intrinsic micron size magnetic domains of a Pt/Co/Pt ferromagnetic stack,” *Appl. Phys. Lett.*, vol. 111, no. 24, p. 242404, 2017. (Cited in pages 47, 48).

- [165] K. Vahaplar, A. Kalashnikova, A. Kimel, D. Hinzke, U. Nowak, R. Chantrell, A. Tsukamoto, A. Itoh, A. Kirilyuk, and T. Rasing, “Ultrafast path for optical magnetization reversal via a strongly nonequilibrium state,” *Phys. Rev. Lett.*, vol. 103, no. 11, p. 117201, 2009. (Cited in pages 48, 52).
- [166] S. Alebrand, A. Hassdenteufel, D. Steil, M. Cinchetti, and M. Aeschlimann, “Interplay of heating and helicity in all-optical magnetization switching,” *Phys. Rev. B*, vol. 85, no. 9, p. 092401, 2012. (Cited in pages 48, 92).
- [167] K. Vahaplar, A. Kalashnikova, A. Kimel, S. Gerlach, D. Hinzke, U. Nowak, R. Chantrell, A. Tsukamoto, A. Itoh, A. Kirilyuk *et al.*, “All-optical magnetization reversal by circularly polarized laser pulses: Experiment and multiscale modeling,” *Phys. Rev. B*, vol. 85, no. 10, p. 104402, 2012. (Cited in page 49).
- [168] M. Berritta, R. Mondal, K. Carva, and P. M. Oppeneer, “Ab initio theory of coherent laser-induced magnetization in metals,” *Phys. Rev. Lett.*, vol. 117, no. 13, p. 137203, 2016. (Cited in page 49).
- [169] A. Khorsand, M. Savoini, A. Kirilyuk, A. Kimel, A. Tsukamoto, A. Itoh, and T. Rasing, “Role of magnetic circular dichroism in all-optical magnetic recording,” *Phys. Rev. Lett.*, vol. 108, no. 12, p. 127205, 2012. (Cited in pages 49, 50, 52, 91).
- [170] R. Medapalli, D. Afanasiev, D. Kim, Y. Quessab, S. Manna, S. Montoya, A. Kirilyuk, T. Rasing, A. Kimel, and E. Fullerton, “Multiscale dynamics of helicity-dependent all-optical magnetization reversal in ferromagnetic Co/Pt multilayers,” *Phys. Rev. B*, vol. 96, no. 22, p. 224421, 2017. (Cited in page 52).
- [171] M. O. Ellis, E. E. Fullerton, and R. W. Chantrell, “All-optical switching in granular ferromagnets caused by magnetic circular dichroism,” *Sci. Rep.*, vol. 6, p. 30522, 2016. (Cited in page 52).
- [172] G. Zhang, T. Latta, Z. Babyak, Y. Bai, and T. F. George, “All-optical spin switching: A new frontier in femtomagnetism—A short review and a simple theory,” *Mod. Phys. Lett. B*, vol. 30, no. 21, p. 16300052, 2016. (Cited in page 52).
- [173] S. Maat, K. Takano, S. Parkin, and E. E. Fullerton, “Perpendicular exchange bias of Co/Pt multilayers,” *Phys. Rev. Lett.*, vol. 87, no. 8, p. 087202, 2001. (Cited in page 53).

- [174] T. Kirk, O. Hellwig, and E. E. Fullerton, “Coercivity mechanisms in positive exchange-biased Co films and Co/Pt multilayers,” *Phys. Rev. B*, vol. 65, no. 22, p. 224426, 2002. (Cited in page 53).
- [175] W. Zeper, F. Greidanus, P. Carcia, and C. Fincher, “Perpendicular magnetic anisotropy and magneto-optical Kerr effect of vapor-deposited Co/Pt-layered structures,” *J. Appl. Phys.*, vol. 65, no. 12, pp. 4971–4975, 1989. (Cited in pages 53, 54).
- [176] S. Hashimoto, Y. Ochiai, and K. Aso, “Film thickness dependence of magneto-optical and magnetic properties in Co/Pt and Co/Pd multilayers,” *J. Appl. Phys.*, vol. 67, no. 9, pp. 4429–4431, 1990. (Cited in page 53).
- [177] F. Garcia, F. Fettar, S. Auffret, B. Rodmacq, and B. Dieny, “Exchange-biased spin valves with perpendicular magnetic anisotropy based on (Co/Pt) multilayers,” *J. Appl. Phys.*, vol. 93, no. 10, pp. 8397–8399, 2003. (Cited in page 53).
- [178] P. Matthes, S. S. P. K. Arekapudi, F. Timmermann, and M. Albrecht, “Magneto-transport properties of perpendicular [Pt/Co]/Cu/[Co/Pt] pseudo-spin-valves,” *IEEE Trans. Magn.*, vol. 51, no. 1, pp. 1–4, 2015. (Cited in page 53).
- [179] J.-H. Park, C. Park, T. Jeong, M. T. Moneck, N. T. Nufer, and J.-G. Zhu, “Co/Pt multilayer based magnetic tunnel junctions using perpendicular magnetic anisotropy,” *J. Appl. Phys.*, vol. 103, no. 7, p. 07A917, 2008. (Cited in page 53).
- [180] Z. Kugler, J.-P. Grote, V. Drewello, O. Schebaum, G. Reiss, and A. Thomas, “Co/Pt multilayer-based magnetic tunnel junctions with perpendicular magnetic anisotropy,” *J. Appl. Phys.*, vol. 111, no. 7, p. 07C703, 2012. (Cited in page 53).
- [181] R. Sbiaa, H. Meng, and S. Piramanayagam, “Materials with perpendicular magnetic anisotropy for magnetic random access memory,” *Phys. Status Solidi RRL*, vol. 5, no. 12, pp. 413–419, 2011. (Cited in page 53).
- [182] S. Woo, K. Litzius, B. Krüger, M.-Y. Im, L. Caretta, K. Richter, M. Mann, A. Krone, R. M. Reeve, M. Weigand *et al.*, “Observation of room-temperature magnetic skyrmions and their current-driven dynamics in ultrathin metallic ferromagnets,” *Nat. Mater.*, vol. 15, no. 5, p. 501, 2016. (Cited in page 53).

- [183] G. Li, R. Medapalli, R. Mikhaylovskiy, F. Spada, T. Rasing, E. Fullerton, and A. Kimel, “THz emission from Co/Pt bilayers with varied roughness, crystal structure, and interface intermixing,” *arXiv preprint arXiv:1903.04423*, 2019. (Cited in page 53).
- [184] N. Berggaard, M. Hehn, S. Mangin, G. Lengaigne, F. Montaigne, M. Lalieu, B. Koopmans, and G. Malinowski, “Hot-electron-induced ultrafast demagnetization in Co/Pt multilayers,” *Phys. Rev. Lett.*, vol. 117, no. 14, p. 147203, 2016. (Cited in page 53).
- [185] C. Brucker, “Magneto-Optical Thin Film Recording Materials in Practice,” in *Handbook of Magneto-Optical Data Recording*, W. McDaniel and R. H. Victora, Eds. Elsevier, 1995, ch. 5, pp. 279–361. (Cited in page 53).
- [186] K. J. Buschow, *Concise encyclopedia of magnetic and superconducting materials*. Elsevier, 2005. (Cited in page 54).
- [187] W. Zeper, F. J. Greidanus, H. Van Kesteren, B. A. Jacobs, J. Spruit, and P. F. Carcia, “Co/Pt and Co/Pd multilayers as a new class of magneto-optical recording materials,” in *Electro-Optic and Magneto-Optic Materials II*, vol. 1274. International Society for Optics and Photonics, 1990, pp. 282–293. (Cited in page 54).
- [188] D. Weller, H. Brändle, and C. Chappert, “Relationship between Kerr effect and perpendicular magnetic anisotropy in  $\text{Co}_{1-x}\text{Pt}_x$  and  $\text{Co}_{1-x}\text{Pd}_x$  alloys,” *J. Magn. Magn. Mater.*, vol. 121, no. 1-3, pp. 461–470, 1993. (Cited in page 54).
- [189] D. Weller, Y. Wu, J. Stöhr, M. Samant, B. Hermsmeier, and C. Chappert, “Orbital magnetic moments of Co in multilayers with perpendicular magnetic anisotropy,” *Phys. Rev. B*, vol. 49, no. 18, p. 12888, 1994. (Cited in page 54).
- [190] N. Nakajima, T. Koide, T. Shidara, H. Miyauchi, H. Fukutani, A. Fujimori, K. Iio, T. Katayama, M. Nývlt, and Y. Suzuki, “Perpendicular magnetic anisotropy caused by interfacial hybridization via enhanced orbital moment in Co/Pt multilayers: Magnetic circular x-ray dichroism study,” *Phys. Rev. Lett.*, vol. 81, no. 23, p. 5229, 1998. (Cited in pages 54, 55).
- [191] I. Chung, Y. Koo, and J. Lee, “Interface structure and magnetic anisotropy of a Co/Pt multilayer,” *J. Appl. Phys.*, vol. 87, no. 9, pp. 4205–4209, 2000. (Cited in page 54).



- [192] G. Bertero, R. Sinclair, C.-H. Park, and Z. Shen, “Interface structure and perpendicular magnetic anisotropy in Pt/Co multilayers,” *J. Appl. Phys.*, vol. 77, no. 8, pp. 3953–3959, 1995. (Cited in page 54).
- [193] P. Chowdhury, P. Kulkarni, M. Krishnan, H. C. Barshilia, A. Sagdeo, S. Rai, G. Lodha, and D. Sridhara Rao, “Effect of coherent to incoherent structural transition on magnetic anisotropy in Co/Pt multilayers,” *J. Appl. Phys.*, vol. 112, no. 2, p. 023912, 2012. (Cited in page 55).
- [194] J. Kanak, M. Czapkiewicz, T. Stobiecki, M. Kachel, I. Sveklo, A. Maziewski, and S. van Dijken, “Influence of buffer layers on the texture and magnetic properties of Co/Pt multilayers with perpendicular anisotropy,” *Phys. Status Solidi A*, vol. 204, no. 12, pp. 3950–3953, 2007. (Cited in page 55).
- [195] C.-J. Lin, G. Gorman, C. Lee, R. Farrow, E. Marinero, H. Do, H. Notarys, and C. Chien, “Magnetic and structural properties of Co/Pt multilayers,” *J. Magn. Magn. Mater.*, vol. 93, pp. 194–206, 1991. (Cited in pages 55, 56).
- [196] M. Labrune and L. Belliard, “Stripe domains in multilayers: Micromagnetic simulations,” *Phys. Status Solidi A*, vol. 174, no. 2, pp. 483–497, 1999. (Cited in page 55).
- [197] C. Kittel, “Theory of the structure of ferromagnetic domains in films and small particles,” *Phys. Rev.*, vol. 70, no. 11-12, p. 965, 1946. (Cited in page 55).
- [198] V. Baltz, A. Marty, B. Rodmacq, and B. Dieny, “Magnetic domain replication in interacting bilayers with out-of-plane anisotropy: application to Co/ Pt multilayers,” *Phys. Rev. B*, vol. 75, no. 1, p. 014406, 2007. (Cited in page 55).
- [199] B. Kaplan and G. Gehring, “The domain structure in ultrathin magnetic films,” *J. Magn. Magn. Mater.*, vol. 128, no. 1-2, pp. 111–116, 1993. (Cited in page 55).
- [200] O. Hellwig, A. Berger, J. B. Kortright, and E. E. Fullerton, “Domain structure and magnetization reversal of antiferromagnetically coupled perpendicular anisotropy films,” *J. Magn. Magn. Mater.*, vol. 319, no. 1, pp. 13–55, 2007. (Cited in page 56).
- [201] C. Tatnall, D. Joyce, P. Grundy, J.-P. Schille, and G. Van der Laan, “Anisotropy, orbital moments and microstructure in Co/Pt multilayer films,” *J. Magn. Magn. Mater.*, vol. 177, pp. 1181–1182, 1998. (Cited in page 56).

- [202] P. Bruno, "Dipolar magnetic surface anisotropy in ferromagnetic thin films with interfacial roughness," *J. Appl. Phys.*, vol. 64, no. 6, pp. 3153–3156, 1988. (Cited in page 56).
- [203] D. Weller, H. Notarys, T. Suzuki, G. Gorman, T. Logan, I. McFadyen, and C. Chien, "Thickness dependent coercivity in sputtered Co/Pt multilayers," *IEEE Trans. Magn.*, vol. 28, no. 5, pp. 2500–2502, 1992. (Cited in pages 56, 57).
- [204] P. Pitcher, J. Miller, D. Pearson, and P. Gurney, "Stacked Pt/Co multilayers with independent control of coercivity and Curie temperature," *J. Magn. Soc. Jpn.*, vol. 17, no. S1\_MORIS\_92, pp. S1.95–98, 1993. (Cited in pages 56, 57, 133).
- [205] G. Harp and S. Parkin, "Epitaxial growth of metals by sputter deposition," *Thin Solid Films*, vol. 288, no. 1-2, pp. 315–324, 1996. (Cited in page 57).
- [206] Nanosensors, "Point Probe Plus Magnetic Force Microscopy - Low Momentum - Reflex Coating," 2018, [Online; accessed 11-July-2019]. [Online]. Available: <https://www.nanosensors.com/Point-Probe-Plus-Magnetic-Force-Microscopy-Low-Momentum-Reflex-Coating-afm-tip-PPP-LM-MFMR> (Cited in page 60).
- [207] A. R. Calaforra, "Thin Magnetic Layer Elements for Applications in Spintronics," Ph.D. dissertation, Technische Universität Kaiserslautern, Kaiserslautern, 2015. (Cited in page 63).
- [208] A. Hasçalık and U. Çaydaş, "Optimization of turning parameters for surface roughness and tool life based on the Taguchi method," *Int. J. Adv. Manuf. Technol.*, vol. 38, no. 9-10, pp. 896–903, 2008. (Cited in page 63).
- [209] W. Yang, C. Hsu, Y. Liu, R. Hsu, T. Lu, and C. Hu, "The structure and photocatalytic activity of TiO<sub>2</sub> thin films deposited by DC magnetron sputtering," *Superlattices Microstruct.*, vol. 52, no. 6, pp. 1131–1142, 2012. (Cited in page 63).
- [210] D. Mishra, N. Bejoy, and M. Sharon, "Application of Taguchi Methodology for Optimization of Parameters of CVD Influencing Formation of a Desired Optical Band Gap of Carbon Film," *Carbon Lett.*, vol. 6, no. 2, pp. 96–100, 2005. (Cited in page 63).

- [211] M. S. Phadke, *Quality Engineering Using Robust Design*. Prentice Hall PTR, 1995. (Cited in page 64).
- [212] J. H. Thomas III, “Effect of pressure on DC planar magnetron sputtering of platinum,” *J. Vac. Sci. Technol. A*, vol. 21, no. 3, pp. 572–576, 2003. (Cited in page 66).
- [213] W. Antel Jr, M. Schwickert, T. Lin, W. O’Brien, and G. Harp, “Induced ferromagnetism and anisotropy of Pt layers in Fe/Pt (001) multilayers,” *Phys. Rev. B*, vol. 60, no. 18, p. 12933, 1999. (Cited in page 72).
- [214] F. Willems, C. von Korff Schmising, D. Weder, C. M. Günther, M. Schneider, B. Pfau, S. Meise, E. Guehrs, J. Geilhufe, A. E. D. Merhe *et al.*, “Multi-color imaging of magnetic Co/Pt heterostructures,” *Struct. Dyn.*, vol. 4, no. 1, p. 014301, 2017. (Cited in page 73).
- [215] F. Willems, C. Smeenk, N. Zhavoronkov, O. Kornilov, I. Radu, M. Schmidbauer, M. Hanke, C. von Korff Schmising, M. Vrakking, and S. Eisebitt, “Probing ultrafast spin dynamics with high-harmonic magnetic circular dichroism spectroscopy,” *Phys. Rev. B*, vol. 92, no. 22, p. 220405, 2015. (Cited in page 73).
- [216] O. Svelto and D. C. Hanna, *Principles of Lasers*. Springer, 1998. (Cited in page 76).
- [217] K. F. Walll and A. Sanchez, “Titanium sapphire lasers,” *The Lincoln Laboratory Journal*, vol. 3, no. 3, pp. 447–462, 1990. (Cited in pages 76, 77).
- [218] W. Koechner, *Solid-state Laser Engineering*. Springer, 2013. (Cited in page 76).
- [219] K. F. Renk, *Basics of Laser Physics*. Springer, 2012. (Cited in page 77).
- [220] D. Strickland and G. Mourou, “Compression of amplified chirped optical pulses,” *Opt. Commun.*, vol. 55, no. 6, pp. 447–449, 1985. (Cited in page 77).
- [221] I. Jovanovic, “Chirped-Pulse Amplification: Ultrahigh peak power production from compact short-pulse laser systems,” *Opt. Photon.*, vol. 5, no. 4, pp. 30–33, 2010. (Cited in page 78).
- [222] R. Trebino, *Frequency-resolved optical gating: the measurement of ultrashort laser pulses*. Springer, 2012. (Cited in pages 79, 80).

- [223] W. Schade, D. L. Osborn, J. Preusser, and S. R. Leone, “Two-color cross-correlation of fs-laser pulses by two-photon induced photoconductivity for near and far field optical measurements,” *Opt. Commun.*, vol. 150, no. 1-6, pp. 27–32, 1998. (Cited in pages 81, 82).
- [224] Wikipedia, “Prism compressor,” 2019, [Online; accessed 11-July-2019]. [Online]. Available: [https://en.wikipedia.org/wiki/Prism\\_compressor](https://en.wikipedia.org/wiki/Prism_compressor) (Cited in page 82).
- [225] J. McCord, “Progress in magnetic domain observation by advanced magneto-optical microscopy,” *J. Phys. D*, vol. 48, no. 33, p. 333001, 2015. (Cited in page 82).
- [226] T. S. Tkaczyk, *Field guide to microscopy*. Spie Bellingham, 2010. (Cited in pages 83, 84).
- [227] G. R. Fowles, *Introduction to Modern Optics*. Courier Corporation, 1989. (Cited in pages 83, 86).
- [228] C.-S. Liu, Y.-C. Chang, K.-W. Lin, and P.-H. Lin, “Speckle reduction in laser imaging applications using rotating magneto-optical disk,” *J. Opt. Soc. Am. A*, vol. 31, no. 1, pp. 16–20, 2014. (Cited in page 84).
- [229] C. A. Schneider, W. S. Rasband, and K. W. Eliceiri, “NIH Image to ImageJ: 25 years of image analysis,” *Nat. Methods*, vol. 9, no. 7, p. 671, 2012. (Cited in pages 85, 90).
- [230] S. Smith, *The scientist and engineer’s guide to digital signal processing*, 1997. (Cited in page 86).
- [231] J. Feng and A. Scholl, “Photoemission electron microscopy (PEEM),” in *Science of Microscopy*, P. W. Hawkes and J. C. H. Spence, Eds. Springer, 2007, ch. 9, pp. 657–695. (Cited in pages 87, 88).
- [232] F. Nickel, D. Gottlob, I. Krug, H. Doganay, S. Cramm, A. Kaiser, G. Lin, D. Makarov, O. Schmidt, and C. Schneider, “Time-resolved magnetic imaging in an aberration-corrected, energy-filtered photoemission electron microscope,” *Ultramicroscopy*, vol. 130, pp. 54–62, 2013. (Cited in page 87).
- [233] D. Attwood and A. Sakdinawat, *X-rays and Extreme Ultraviolet Radiation: Principles and Applications*. Cambridge University Press, 2017. (Cited in pages 87, 88).

- [234] U. Parlak, R. Adam, D. E. Bürgler, S. Gang, and C. Schneider, “Optically induced magnetization reversal in  $[\text{Co}/\text{Pt}]_N$  multilayers: Role of domain wall dynamics,” *Phys. Rev. B*, vol. 98, no. 21, p. 214443, 2018. (Cited in page 89).
- [235] D. L. Windt, “IMD—Software for modeling the optical properties of multilayer films,” *Comput. Phys.*, vol. 12, no. 4, pp. 360–370, 1998. (Cited in page 105).
- [236] F. Schlickeiser, U. Ritzmann, D. Hinzke, and U. Nowak, “Role of entropy in domain wall motion in thermal gradients,” *Phys. Rev. Lett.*, vol. 113, no. 9, p. 097201, 2014. (Cited in pages 107, 113, 117).
- [237] S. Moretti, V. Raposo, E. Martinez, and L. Lopez-Diaz, “Domain wall motion by localized temperature gradients,” *Phys. Rev. B*, vol. 95, no. 6, p. 064419, 2017. (Cited in pages 107, 113).
- [238] D. Hinzke and U. Nowak, “Domain wall motion by the magnonic spin Seebeck effect,” *Phys. Rev. Lett.*, vol. 107, no. 2, p. 027205, 2011. (Cited in pages 107, 117).
- [239] Y. A. Shokr, O. Sandig, M. Erkovan, B. Zhang, M. Bernien, A. A. Ünal, F. Kronast, U. Parlak, J. Vogel, and W. Kuch, “Steering of magnetic domain walls by single ultrashort laser pulses,” *Phys. Rev. B*, vol. 99, no. 21, p. 214404, 2019. (Cited in pages 107, 113).
- [240] K.-W. Moon, J.-C. Lee, S.-G. Je, K.-S. Lee, K.-H. Shin, and S.-B. Choe, “Long-range domain wall tension in Pt/Co/Pt films with perpendicular magnetic anisotropy,” *Applied Phys. Express*, vol. 4, no. 4, p. 043004, 2011. (Cited in page 107).
- [241] O. Sandig, Y. Shokr, J. Vogel, S. Valencia, F. Kronast, and W. Kuch, “Movement of magnetic domain walls induced by single femtosecond laser pulses,” *Phys. Rev. B*, vol. 94, no. 5, p. 054414, 2016. (Cited in page 113).
- [242] J. Sampaio, J. Grollier, and P. J. Metaxas, “Domain wall motion in nanostructures,” in *Handbook of Surface Science*, R. E. Camley, Z. Celinski, and R. L. Stamps, Eds. Elsevier, 2015, vol. 5, ch. 8, pp. 335–370. (Cited in page 113).
- [243] A. Chakravarty, J. Mentink, C. Davies, K. Yamada, A. Kimel, and T. Rasing, “Supervised learning of an opto-magnetic neural network with ultrashort laser pulses,” *Appl. Phys. Lett.*, vol. 114, no. 19, p. 192407, 2019. (Cited in page 113).

- [244] W. Jiang, P. Upadhyaya, Y. Fan, J. Zhao, M. Wang, L.-T. Chang, M. Lang, K. L. Wong, M. Lewis, Y.-T. Lin, J. Tang, S. Cherepov, X. Zhou, T. Yaroslav, R. N. Schwartz, and K. L. Wang, “Direct imaging of thermally driven domain wall motion in magnetic insulators,” *Phys. Rev. Lett.*, vol. 110, no. 17, p. 177202, 2013. (Cited in page 113).
- [245] Y. Mimura, N. Imamura, and T. Kobayashi, “Thermomagnetic writing on Gd–Fe and Gd–Fe–Y amorphous films,” *Jpn. J. Appl. Phys.*, vol. 17, no. 8, p. 1365, 1978. (Cited in page 113).
- [246] A. Hassdenteufel, B. Hebler, C. Schubert, A. Liebig, M. Teich, M. Helm, M. Aeschlimann, M. Albrecht, and R. Bratschitsch, “Thermally Assisted All-Optical Helicity Dependent Magnetic Switching in Amorphous Fe<sub>100-x</sub>Tb<sub>x</sub> Alloy Films,” *Adv. Mater.*, vol. 25, no. 22, pp. 3122–3128, 2013. (Cited in pages 113, 114).
- [247] A. Donges, N. Grimm, F. Jakobs, S. Selzer, U. Ritzmann, U. Atxitia, and U. Nowak, “Unveiling domain wall dynamics of ferrimagnets in thermal magnon currents: competition of angular momentum transfer and entropic torque,” *arXiv preprint arXiv:1911.05393*, 2019. (Cited in page 117).
- [248] P. Yan, X. Wang, and X. Wang, “All-magnonic spin-transfer torque and domain wall propagation,” *Phys. Rev. Lett.*, vol. 107, no. 17, p. 177207, 2011. (Cited in page 117).
- [249] A. Barman, S. Wang, O. Hellwig, A. Berger, E. E. Fullerton, and H. Schmidt, “Ultrafast magnetization dynamics in high perpendicular anisotropy [Co/Pt]<sub>n</sub> multilayers,” *J. Appl. Phys.*, vol. 101, no. 9, p. 09D102, 2007. (Cited in page 119).
- [250] G. Malinowski, F. Dalla Longa, J. Rietjens, P. Paluskar, R. Huijink, H. Swagten, and B. Koopmans, “Control of speed and efficiency of ultrafast demagnetization by direct transfer of spin angular momentum,” *Nat. Phys.*, vol. 4, no. 11, p. 855, 2008. (Cited in page 119).
- [251] C. von Korff Schmising, M. Giovannella, D. Weder, S. Schaffert, J. Webb, and S. Eisebitt, “Nonlocal ultrafast demagnetization dynamics of Co/Pt multilayers by optical field enhancement,” *New J. Phys.*, vol. 17, no. 3, p. 033047, 2015. (Cited in page 119).

- 
- [252] W. A. Challener and A. V. Itagi, “Near-field optics for heat-assisted magnetic recording (experiment, theory, and modeling),” in *Modern Aspects of Electrochemistry*, M. Schlesinger, Ed. Springer, 2009, pp. 53–111. (Cited in page 127).
- [253] E. Ögüt, G. Kızıldaş, and K. Şendur, “Circularly polarized localized near-field radiation at the nanoscale,” *Appl. Phys. B*, vol. 99, no. 1-2, pp. 67–74, 2010. (Cited in page 127).

# Abbreviations

<b>AFM</b>	Antiferromagnetic	<b>MBE</b>	Molecular beam epitaxy
<b>AFM</b>	Atomic force microscopy	<b>MCD</b>	Magnetic circular dichroism
<b>AODF</b>	All-optical domain formation	<b>MFM</b>	Magnetic force microscopy
<b>AO-HDS</b>	All-optical helicity-dependent switching	<b>MFP</b>	Mean free path
<b>AO-HIS</b>	All-optical helicity-independent switching	<b>MOKE</b>	Magneto-optical Kerr effect
<b>AOS</b>	All-optical switching	<b>MRAM</b>	Magnetic random access memory
<b>APD</b>	Areal pulse density	<b>MTJ</b>	Magnetic tunnel junctions
<b>BBO</b>	$\beta$ -Barium borate	<b>M3TM</b>	Microscopic three temperature model
<b>BPMR</b>	Bit-patterned magnetic recording	<b>NA</b>	Numerical aperture
<b>CCD</b>	Charge coupled device	<b>NFT</b>	Near field transducer
<b>CPA</b>	Chirped pulse amplification	<b>NM</b>	Non-magnetic
<b>CW</b>	Continuous wave	<b>PBS</b>	Polarizing beam splitter
<b>DCM</b>	Dichroic mirror	<b>PD</b>	Photodiode
<b>DMI</b>	Dzyaloshinskii-Moriya interaction	<b>PEEM</b>	Photoemission electron microscopy
<b>DOE</b>	Design of experiment	<b>PM</b>	Paramagnetic
<b>DOS</b>	Density of states	<b>PMA</b>	Perpendicular magnetic anisotropy
<b>DW</b>	Domain wall	<b>PMR</b>	Perpendicular magnetic recording
<b>EY</b>	Elliot-Yafet	<b>PTD</b>	Pure thermal demagnetization
<b>FM</b>	Ferromagnetic	<b>PVD</b>	Physical vapor deposition
<b>FOV</b>	Field of view	<b>QCM</b>	Quartz crystal microbalance
<b>FWHM</b>	Full width at half maximum	<b>RCP</b>	Right circular polarization
<b>GMR</b>	Giant magnetoresistance	<b>RE</b>	Rare-earth
<b>GT</b>	Glan-Thompson	<b>RKKY</b>	Ruderman-Kittel-Kasuya-Yosida
<b>GVD</b>	Group velocity dispersion	<b>RPM</b>	Rounds per minute
<b>HAMR</b>	Heat-assisted magnetic recording	<b>SMR</b>	Shingled magnetic recording
<b>HDD</b>	Hard disk drive	<b>SNR</b>	Signal-to-noise ratio
<b>HNF</b>	Helmholtz Nanoelectronic Facility	<b>SOI</b>	Spin-orbit interaction
<b>HWP</b>	Half-wave plate	<b>SSD</b>	Solid-state drive
<b>IFE</b>	Inverse Faraday effect	<b>SSE</b>	Spin Seebeck effect
<b>LCP</b>	Left circular polarization	<b>TDMR</b>	Two-dimensional magnetic recording
<b>LLG</b>	Landau-Lifschitz-Gilbert	<b>TM</b>	Transition metal
<b>LMR</b>	Longitudinal magnetic recording	<b>UHV</b>	Ultra-high vacuum
<b>LP</b>	Linear polarization	<b>XMCD</b>	X-ray circular magnetic dichroism
<b>MAMR</b>	Microwave-assisted magnetic recording	<b>XRR</b>	X-ray reflectivity





# Symbols

$A$	Exchange stiffness parameter	$I$	Stoner parameter
$\mathbf{D}$	Displacement vector	$J$	Exchange integral
$D$	Thermal diffusivity	$\mathbf{J}$	Total angular momentum
$D_0$	Characteristic domain size	$K_{eff}$	Effective anisotropy constant
$\mathbf{E}$	Electric field vector	$K_{MCA}$	Magnetocrystalline anisotropy constant
$E_{ani}$	Magnetic anisotropy energy	$K_{Sh}$	Shape anisotropy constant
$E_B$	Electron binding energy	$K_u$	Magnetic anisotropy constant
$E_F$	Fermi energy level	$\mathbf{L}$	Orbital momentum
$G_{el,sl,es}$	Coupling constants between electron, lattice and spin reservoirs	$\mathbf{M}$	Magnetization
$g_e$	Electron g-factor	$\mathbf{m}_i$	Magnetic moment
$H$	Heisenberg Hamiltonian	$M_S$	Saturation magnetization
$H_C$	Coercive field	$M_R$	Remanence magnetization
$H_d$	Demagnetization field	$\mathbf{S}_i$	Spin operator
$H_{ext}$	External magnetic field	$\mathbf{S}$	Spin momentum
$H_N$	Nucleation field	$T$	Temperature
$H_P$	Pinning field	$T_{e,s,l}$	Electron, spin and lattice temperatures
$H_{SO}$	Spin-orbit Hamiltonian	$T_C$	Curie temperature
$H(t)$	Heaviside step function	$V$	Volume
		$Z$	Nuclear charge
$\alpha$	Gilbert damping parameter	$\pi$	Linear polarization
$\gamma$	Domain wall energy	$\sigma_w$	Domain wall energy density
$\epsilon_0$	Dielectric permittivity constant	$\sigma^{+,-}$	Right and left circular polarization
$\epsilon(\omega)$	Dielectric permittivity tensor	$\tau_E$	Relaxation time
$\eta_K$	Kerr ellipticity	$\tau_M$	Demagnetization time
$\theta_K$	Kerr rotation	$\Phi_K$	Complex Kerr rotation
$\mu$	Optical absorption coefficient	$\omega_L$	Larmor frequency
$\mathcal{N}$	Demagnetizing tensor		
$eV$	Electronvolt		$1.602 \times 10^{-19} \text{ J}$
$k_B$	Boltzmann constant		$1.380 \times 10^{-23} \text{ J} \cdot \text{K}^{-1}$
$\mu_B$	Bohr magneton		$9.274 \times 10^{-24} \text{ J} \cdot \text{T}^{-1}$



# Publications and conference contributions

## Articles

- A1** “Selective area growth and stencil lithography for in situ fabricated quantum devices”  
P. Schüffegen, D. Rosenbach, C. Li, T. Schmitt, M. Schleenvoigt, A. R. Jalil, S. Schmitt, J. Kölzer, M. Wang, B. Benjemann, **U. Parlak**, L. Kibkalo, S. Trelenkamp, T. Grap, D. Meertens, M. Luysberg, G. Mussler, E. Berenschot, N. Tas, A. A. Golubov, A. Brinkman, T. Schäpers, D. Grützmacher  
*Nat. Nanotechnol.*, **14**, 825-831 (2019)
- A2** “Steering of magnetic domain walls by single ultrashort laser pulses”  
Y. S. Shokr, O. Sandig, M. Erkovan, B. Zhang, M. Bernien, A. A. Ünal, F. Kronast, **U. Parlak**, J. Vogel, W. Kuch  
*Phys. Rev. B*, **99**, 214404 (2019)
- A3** “Current-induced domain wall oscillations in a nanowire imaged by time-resolved photoemission electron microscopy”  
M. I. Khan, S. Cramm, D. E. Bürgler, **U. Parlak**, S. Nemsák, D. M. Gottlob, J. Hackl, H. Doğanay, C. M. Schneider  
*J. Magn. Magn. Mater.*, **476**, 538-545 (2019)
- A4** “Optically induced magnetization reversal in  $[\text{Co/Pt}]_N$  multilayers: Role of domain wall dynamics”  
**U. Parlak**, R. Adam, D. E. Bürgler, S. Gang, C. M. Schneider  
*Phys. Rev. B*, **98**, 214443 (2018)
- A5** “Element-selective investigation of femtosecond spin dynamics in NiPd magnetic alloys using extreme ultraviolet radiation”  
S. Gang, R. Adam, M. Plötzing, M. von Witzleben, C. Weier, **U. Parlak**, D. E. Bürgler, C. M. Schneider, J. Ruzs, P. Maldonado, P. M. Oppeneer  
*Phys. Rev. B*, **97**, 064412 (2018)

- 
- A6** “The study of exchange bias effect in  $\text{Pt}_x\text{Co}_{1-x}/\text{CoO}$  bilayers”  
M. Erkovan, M. E. Aköz, **U. Parlak**, O. Öztürk  
*J. Supercond. Nov. Magn.*, **30**, 2909-2913 (2017)
- A7** “Coexistence of perpendicular and parallel exchange bias effects on Ni/CoO bilayer”  
**U. Parlak**, M. E. Aköz, M. Erkovan  
*J. Supercond. Nov. Magn.*, **29**, 1851-1854 (2016)
- A8** “Probing exchange bias properties of  $\text{Pt}_x\text{Co}_{1-x}/\text{Pt}/\text{CoO}$  films”  
M. Erkovan, M. E. Aköz, M. Öztürk, E. Demirci, **U. Parlak**, N. Akdogan, O. Öztürk  
*J. Supercond. Nov. Magn.*, **29**, 163-168 (2016)

**Conference contributions (related to this work)**

- Talk** Optically induced magnetization reversal in  $[\text{Co}/\text{Pt}]_N$  multilayers: Role of domain wall dynamics, **U. Parlak**, R. Adam\*, D. E. Bürgler, S. Gang, C. M. Schneider, The 10th International Symposium on Metallic Multilayers, 18 Jun 2019, Madrid, ES
- Talk** Magnetization reversal and demagnetization dynamics of Co/Pt multilayers with circularly polarized laser pulses, **U. Parlak\***, R. Adam, S. Gang, M. Plötzing, D. E. Bürgler, C. M. Schneider, DPG Spring Meeting, 12 Mar 2018, Berlin, DE
- Invited talk** Optically induced magnetization reversal dynamics in  $(\text{Pt}/\text{Co})_N$  multilayers, R. Adam\*, **U. Parlak**, M. Plötzing, D. E. Bürgler, C. M. Schneider, SPIE Nanoscience and Nanoengineering, 10 Aug 2017, San Diego, US
- Talk** All-optical switching and ultrafast magnetization dynamics in Pt/Co multilayers, **U. Parlak\***, M. Plötzing, D. E. Bürgler, C. M. Schneider, DPG Spring Meeting, 20 Mar 2017, Dresden, DE
- Talk** Effect of material properties and laser beam characteristics on all-optical switching of ferromagnetic  $(\text{Co}/\text{Pt})_N$  multilayers, **U. Parlak\***, D. E. Bürgler, R. Adam, G. Shayeganrad, S. Khan, C. M. Schneider, The 9th International Symposium on Metallic Multilayers, 20 Jun 2016, Uppsala, SE
- Talk** Towards optically controlled magnetization reversal in ferromagnetic  $(\text{Co}/\text{Pt})_N$  and  $(\text{Co}/\text{Pd})_N$  multilayers, **U. Parlak\***, D. E. Bürgler, R. Adam, G. Shayeganrad, S. Khan, C. M. Schneider, DPG Spring Meeting, 7 Mar 2016, Regensburg, DE
- Poster** Optically induced magnetization reversal in  $[\text{Co}/\text{Pt}]_N$  multilayers, **U. Parlak**, R. Adam\*, D. E. Bürgler, S. Nemsak, S. Gang, Claus M. Schneider, ICMFS-2018, July 2018, Santa Cruz, US
- Poster** All-optical magnetization reversal in ferromagnetic Co/Pt multilayers, **U. Parlak\***, R. Adam, S. Gang, M. Plötzing, S. Nemsak, D. E. Bürgler, Claus M. Schneider, PoF Scientific Exchange Meeting, Oct 2017, Jülich, DE
- Poster** All-optical switching in Co/Pt multilayers: The effect of beam parameters, **U. Parlak\***, R. Adam, S. Gang, M. Plötzing, S. Nemsak, D. E. Bürgler, Claus M. Schneider, UMC 2017, Oct 2017, Kaiserslautern, DE



# Curriculum vitae

## Personal data

Date of birth	18th October 1987
Place of birth	İstanbul
Nationality	Turkish

## Experience

09/2014-04/2018	PhD Student at PGI-6, Research Centre Jülich
03/2013-07/2014	Research Assistant at Metallurgical and Materials Engineering Dept., Marmara University
06/2011-02/2013	Master's Student at Nanotechnology Research Centre, Gebze Technical University

## Education

PhD in Physics 2015-2021	Duisburg-Essen University (DE)
MSc in Physics 2011-2014	Gebze Technical University (TR)
BSc in Materials Sci. and Engineering 2009-2012	Gebze Technical University (TR)
BSc in Physics 2007-2011	Gebze Technical University (TR)

## Research overview

Magnetic thin film fabrication and characterization, magneto-optics, ultrafast magnetism, surface science

## Publication list (online)

[ResearchGate](#), [Google Scholar](#)

**Umut Parlak**





# Acknowledgments

I express my gratitude to all the people, who supported me to accomplish this work. Hereby, I would like to acknowledge:

My supervisor, **Prof. Dr. Claus M. Schneider**, for giving me the chance to be a member of PGI-6. It has been a great privilege to do my research under his supervision.

**Dr. Roman Adam**, for his extreme support in every step of my experimental work. Without his experience, encouragement and grateful suggestions this work would not be completed.

**PD Dr. Daniel E. Bürgler**, who has inspired me with all his ability of asking striking questions. He also helped a lot for my research at very critical points.

**Prof. Dr. Wolfgang Kuch**, for accepting to be the second referee for the disputation.

**Dr. Stefan Cramm, Dr. Slavomír Nemšák, Dr. Tomáš Duchoň, Dr. M. Imtiaz Khan and Dr. Johanna Hackl**, for their help in XMCD-PEEM microscopy studies at Bessy II in Berlin.

**Thomas Jansen, Benjamin Bennemann and Kristoph Krause**, for their technical support at Nanocluster in HNF.

**Jürgen Lauer, Heinz Pfeiffer, Norbert Schnitzler, Arnd Bremen and Bernd Küpper**, who are the secret heroes behind all experimental achievements. Thank you for the technical support from the first day to the end of my PhD in FZ Jülich.

**René Borowski**, for instructions of clean room technologies.

**Dr. Paul Meuffels**, for his support for the x-ray diffractometer.

**Christian Riedel and Dr. Attila Kákay**, from HZDR Dresden, for their kind help with the Kerr microscopy.

And the last but not the least, all the present and former members of magnetization dynamics group; **Dr. Christian Weier, Dr. Moritz Plötzing, Dr. Seung-gi Gang**,

**Moritz von Witzleben, Sarah Heidtfeld, Christian Greb and Fangzhou Wang.**

I will forever be thankful to **Prof. Dr. H. Bülent Üner**, who inspired me to become a physicist.

Finally, I would like to thank to my family, and my beloved wife **Zümray**.

**Umut Parlak**

Aachen, 2021

Band / Volume 220

**Inspection Games over Time: Fundamental Models and Approaches**

R. Avenhaus und T. Krieger (2020), VIII, 455 pp

ISBN: 978-3-95806-475-1

Band / Volume 221

**High spatial resolution and three-dimensional measurement of charge density and electric field in nanoscale materials using off-axis electron holography**

F. Zheng (2020), xix, 182 pp

ISBN: 978-3-95806-476-8

Band / Volume 222

**Tools and Workflows for Data & Metadata Management of Complex Experiments**

Building a Foundation for Reproducible & Collaborative Analysis in the Neurosciences

J. Sprenger (2020), X, 168 pp

ISBN: 978-3-95806-478-2

Band / Volume 223

**Engineering of *Corynebacterium glutamicum* towards increased malonyl-CoA availability for polyketide synthesis**

L. Milke (2020), IX, 117 pp

ISBN: 978-3-95806-480-5

Band / Volume 224

**Morphology and electronic structure of graphene supported by metallic thin films**

M. Jugovac (2020), xi, 151 pp

ISBN: 978-3-95806-498-0

Band / Volume 225

**Single-Molecule Characterization of FRET-based Biosensors and Development of Two-Color Coincidence Detection**

H. Höfig (2020), XVIII, 160 pp

ISBN: 978-3-95806-502-4

Band / Volume 226

**Development of a transcriptional biosensor and reengineering of its ligand specificity using fluorescence-activated cell sorting**

L. K. Flachbart (2020), VIII, 102 pp

ISBN: 978-3-95806-515-4

Band / Volume 227

**Strain and Tool Development for the Production of Industrially Relevant Compounds with *Corynebacterium glutamicum***

M. Kortmann (2021), II, 138 pp

ISBN: 978-3-95806-522-2

Band / Volume 228

**Complex magnetism of nanostructures on surfaces:  
from orbital magnetism to spin excitations**

S. Brinker (2021), III, 208 pp

ISBN: 978-3-95806-525-3

Band / Volume 229

**High-throughput All-Electron Density Functional Theory Simulations  
for a Data-driven Chemical Interpretation of X-ray Photoelectron Spectra**

J. Bröder (2021), viii, 169, XL pp

ISBN: 978-3-95806-526-0

Band / Volume 230

**Molecular tools for genome engineering of *Corynebacterium glutamicum***

C. K. Sonntag (2021), VIII, 111 pp

ISBN: 978-3-95806-532-1

Band / Volume 231

**Interface Functionalization of Magnetic Oxide Fe<sub>3</sub>O<sub>4</sub>/SrTiO<sub>3</sub>  
Heterostructures**

M. H. A. Hamed (2021), xvii, 151 pp

ISBN: 978-3-95806-535-2

Band / Volume 232

**Optically induced magnetization reversal in Co/Pt multilayers:**

Role of domain wall dynamics

U. Parlak (2021), ix, 162, XII pp

ISBN: 978-3-95806-536-9

Weitere **Schriften des Verlags im Forschungszentrum Jülich** unter  
<http://www.zb1.fz-juelich.de/verlagextern1/index.asp>



Schlüsseltechnologien / Key Technologies

Band / Volume 232

ISBN 978-3-95806-536-9